A dissertation for doctoral degree

MODELING OF WATER-AIR-SOIL THREE-PHASE MATERIAL AND ITS APPLICATION TO GEOTECHNICAL DISASTER INCLUDING LIQUEFATION

水・空気・土粒子三相系の力学特性のモデル化と液状化を含めた地盤災害への適用

Supervised by
Professor **Feng Zhang**

Xiaohua Bao
Department of Scientific and Engineering Simulation
Nagoya Institute of Technology, Japan

May 2012

Abstract

Geotechnical disasters have always threatened human being not only because the disasters may lead to tremendous loss of life and properties, but also it may take a long time to recover or even unrecoverable. Various factors of the geotechnical disasters are existed, among which, heavy rain and earthquake are the two main factors that are difficult to predict. Slope failures caused by heavy rain and liquefaction caused by earthquake are tremendous disasters to human being and civil facilities. These two phenomenons have been investigated by engineers for a long time. The mechanisms of slope failure due to rainfall and liquefaction due to earthquake have been investigated thoroughly as the development of soil mechanics. In a word, in many cases we have to deal with these geotechnical problems depending on saturated soil mechanics or unsaturated soil mechanics.

As is known that saturated soil mechanics has been widely developed for a long time, but for unsaturated soil mechanics, many challenges still lie ahead to geotechnical engineers, especially its engineering practice to solve boundary value problems. The main purpose of this dissertation is to use the existing theories on both saturated and unsaturated soil mechanics to solve various boundary value problems.

For the unsaturated soil problems, first, a new constitutive model based on the experiment study is proposed by Zhang (2011). The constitutive model for unsaturated soil using the skeleton stress and degree of saturation as independent state variables is therefore possible to be able to describe not only the behaviors of unsaturated soil but also saturated soil because the skeleton stress can smoothly shift to effective stress if saturation changes from unsaturated condition to saturated condition.

Next, 2D FEM approaches that consider the interaction between soil skeleton, pore water and pore air in one-dimensional infiltration problem is conducted. In this three-phase field theory, the displacement of solid u and the pore water pressure p^w are taken as the basic variables in the governing equations. The finite element is used to discretize the field equations in space, and finite difference method is used for the discretization of the continuity equation for the pore fluid. Newmark-β method is employed to descretize the field equation in time.

Last, combining the proposed new constitutive model and soil-water-air three-phase mixture theory, 2D unsaturated-saturated numerical analysis is performed using a FEM program SOFT to simulate the process of infiltration in the unsaturated Shirasu slope. The numerical simulation aims to reproduce the three cases of soil tank model tests of

unsaturated Shirasu slope, in which water injection is conducted from the bottom and back of the slope respectively. Simulation results are compared with test results to verify the proposed constitutive model and numerical method.

For the saturated soil problems, numerical simulation on different kinds of ground is carried out using cyclic mobility model proposed by Zhang (2007). The calculation includes three types of ground:

1) Dry sand ground. Numerical tests on seismic enhancement effect of existing group-pile foundation with ground improvement are first conducted to find out the optimum pattern of ground improvement around existing pile foundation. In the numerical tests, three influential factors are considered, that is, the depth, the thickness (or height) and the width (or length) of the ground-improvement zone around the pile group. The numerical tests are conducted in static push-over condition. Firstly, find out an optimum pattern for the partial-ground improvement around an existing pile foundation, and secondary, confirm the efficiency of seismic enhancement by the partial-ground improvement method both by shaking table tests and numerical analyses. As a consequence, the applicability of the DBLEAVES for evaluating the seismic behavior of pile foundation is verified again. In the numerical analyses, nonlinear behaviors of ground and pile are described by cyclic mobility model (Zhang et al, 2007) and axial force dependent model (AFD model) proposed by Zhang and Kimura (2002), respectively.
2) Saturated soft rock ground. Simulation is performed on the undersea soft rock under high confining stress state subjecting to dynamic loading to clarify the mechanism process of the formation from proto-decollement to decollement, which is one step to the clarification of the earthquake mechanism. In the calculation, parameters of the soft rock are determined based on laboratory tests and element simulation. The mechanical behaviors of the soft rock subjecting to huge dynamic loadings such as earthquake motions are well examined. The study object is selected at a depth of 1650m under seabed, where has a confining stress of 9.75MPa. Through the results including acceleration, effective stress and excess pore water pressure, it is understood that decollement zone with a high confining stress may consolidate and become dense when subjected to huge shear stress caused by earthquake.
3) Saturated sand-silt mixed ground. To evaluate the anti-seismic performance of Kanie Parking Lot foundation based on liquefaction analysis, numerical simulation was carried out by 2D soil-water coupled finite element method in two cases, which are the long-pile type foundation and short-pile type foundation. In the numerical calculation, the process during earthquake was simulated by a dynamic soil-water

coupled analysis, while the process of dissipation of excess pore water pressure was simulated by a static consolidation analysis. The mechanical behavior of the ground during liquefaction and the settlement in post-liquefaction is well examined. Through the results, it is clear that although the ground in both two cases liquefied, the structure with the long-pile type foundation has less uneven settlement than the short-pile type foundation after earthquake. The seismic stability of the structure foundation was well evaluated by this numerical analysis.

Acknowledgements

This research could not be finished without the collaboration and support of a number of individuals. I would like to express my gratitude to them here.

First and foremost, I would like to express my heartiest gratitude to my supervisor Professor Feng Zhang at Nagoya Institute of Technology, for his guidance, inspiration, understanding, patience, and most importantly, for his father-like care during my graduate study. As to my research work, he was so strict and criticized me so much for my mistakes that whenever I saw his car parked in front of the laboratory building in the morning I was afraid and felt nervous. On the other hand, he always had patient and taught me like a primary school teacher. He also encouraged me to be an excellent geotechnical engineer, a specialist in numerical simulation and an independent thinker. His clear concept and extensive knowledge in the research will encourage me in the future study. Mòreover, I am very gratitude for his compatibility on my willfulness. Here, I would also like to thank his wife, Mrs. Ying Mao. I really appreciate her for the delicious foods and life guidance. She provided us a warm and nice time every New Year's Eve. I will always remember the good time together with Professor Feng Zhang and his wife – Mrs. Yin Mao for their kindness and care.

I wish to express my special respect and gratitude to Professor Teruo Nakai, who is like a boss in the laboratory and always treats the students kindly. In addition, I am very grateful to Professor Maeda Kenichi, who is always ready to help me especially late at night when I have to stay up late, his passion on the research and leadership in the neighbor laboratory impressed me. I would also give thanks to Associate Professor Md. Shahin Hossain for his assistance and guidance in knowledge of numerical simulation, and Assistant Professor Mamoru Kikumoto, who helped me a lot during the study before doctor course.

I am very grateful to Electronic Officer Tomonori Sato. His support made the numerical

works of my dissertation possible. I would also like to thank Ms. Furukawa who is the secretary of the laboratory and always talk to me like an elder sister.

I would like to give thanks to Professor M. Obata and Professor Hehua Zhu for serving on my dissertation committee and for many helpful comments and suggestions.

I wish to give gratitude to all the students in the laboratory. I had a great five-year time with many wonderful memories under the help of all the students in the laboratory. The copartner Yukihiro Morikawa, who is a kind senior, always discussed with me about research. Moreover, he also helped me a lot when I was in trouble or in low spirits. I would like to thank Mr. Sheng Zhang, Mr. Yuanfeng Bao, Mr. Yonglin Xiong, Mr. Imase, Mr. Kondo, Mr. Nagano, Mr. Okuda, Mr. Nishimura, Mr. Tsukamoto et al. for their friendship and encouragement. I also wish to give gratitude to friends with who I had a good happy time in past five years.

Special thanks should also be given to Associate Professor Guanlin Ye, Department of Civil Engineering, Shanghai Jiao Tong University, Shanghai, China and Teacher Bin Ye, Department of Geotechnical Engineering, Tongji University, Shanghai, China. In this research, many theories and calculations are referenced to the works by Associate Professor Guanlin Ye and Teacher Bin Ye.

I am also very grateful to the Ministry of Education and Culture of Japan (MONBUSHO) for the financial support throughout my five years` study.

Finally, and most importantly, I would like to thank my family, especially to my parents and husband, for their unconditional love, support and encouragement.

Xiaohua Bao
Nagoya Institute of Technology
May 2012

MODELING OF WATER-AIR-SOIL THREE-PHASE MATERIAL AND ITS APPLICATION TO GEOTECHNICAL DISASTER INCLUDING LIQUEFATION

水・空気・土粒子三相系の力学特性のモデル化と液状化を含めた地盤災害への適用

Contents

CHAPTER 1 Introduction

1.1 Problem and objectives

Geotechnical disasters always draw much attention of geotechnical engineers not only because geotechnical disasters may case tremendous lose of life and properties , but also it may take a long time to recover or unrecoverable. Various factors of the geotechnical disasters are existed, among which, heavy rain and earthquake are the two main factors that can be avoided and even difficult to predict. Slope failures caused by heavy rain and liquefaction caused by earthquake are tremendous disasters to human being and civil facilities. These two phenomenons have been investigated by engineers for a long time. Figure 1 shows the natural disaster of slope failure and liquefaction. To avoid or reduce the damages caused by slope failure and liquefaction, mechanism of slope failure and liquefaction has to be made clear. Figure 2 shows the mechanism of slope failure due to rainfall. Figure 3 shows the mechanism of liquefaction due to earthquake clearly.

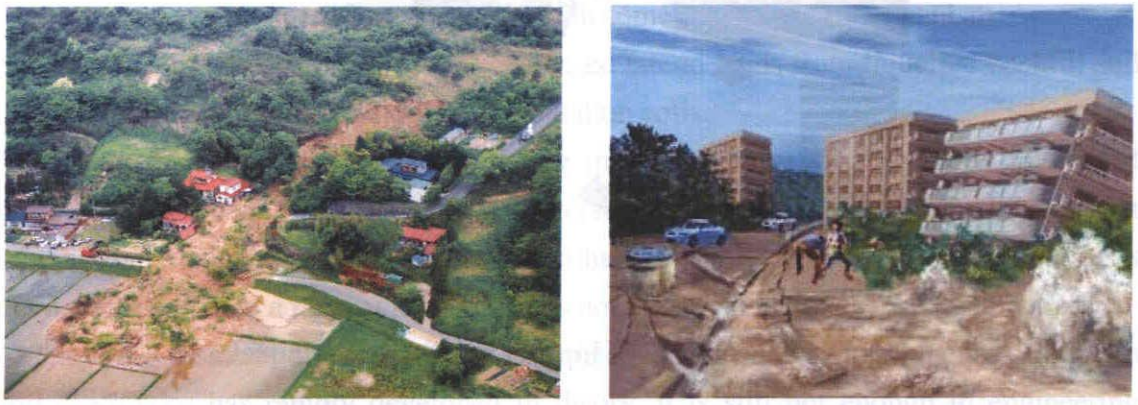

a) Slope failure b) Liquefaction

Figure 1 Natural disaster of slope failure and liquefaction

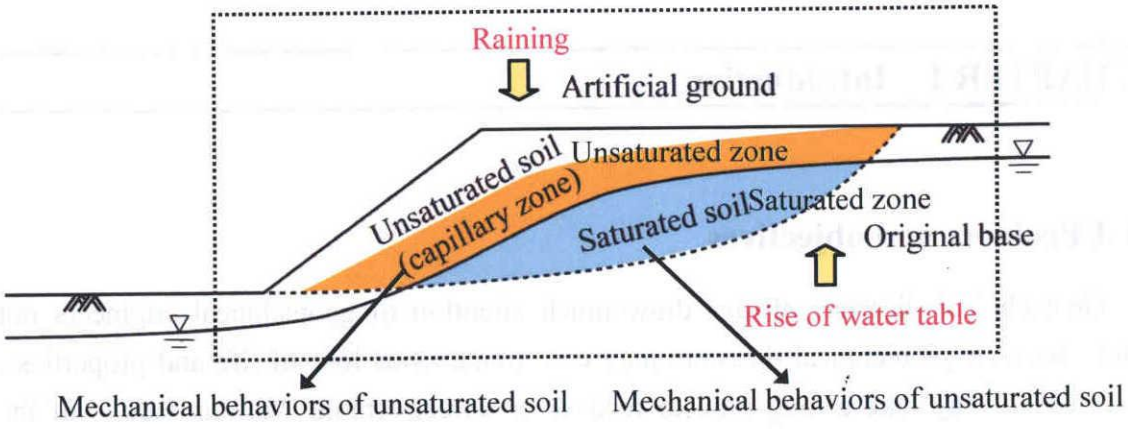

Figure 2 Mechanism of slope failure due to rainfall

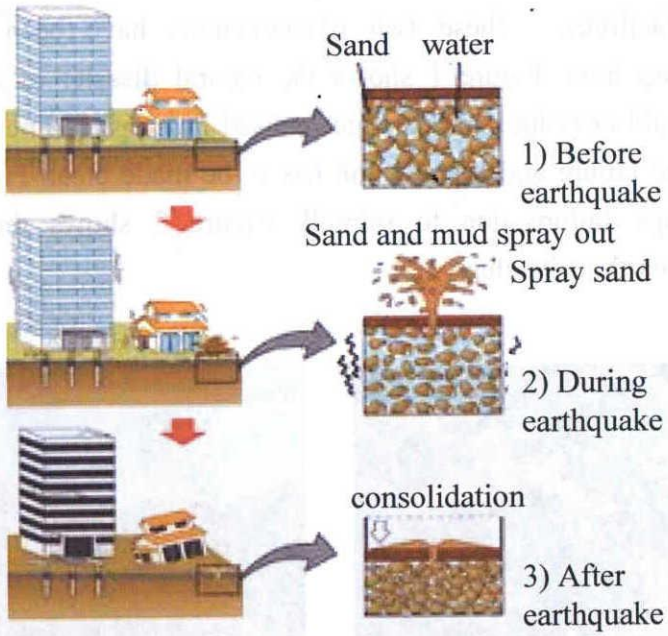

Figure 3 Mechanism of liquefaction due to earthquake

First, for the slope failure in unsaturated conditions, it is closely related to heavy rainfall and infiltration. As shown in Figure 2, the mechanism leading to the slope failure is that the matric suction (negative pore water pressure) decreases when water infiltrates the unsaturated zone in raining seasons. The loss of matric suction makes the shear strength of the soil decrease below the mobilized shear strength along the potential slip surface (Hsin-Fu Yeh, et al, 2006). Usually unsaturated residual soils experience high matric suction in dry period, which contributes to the shear strength of the soil. But in the longtime wet period, there is sufficient infiltration into the slope, and

the matric suction of the soil decreases, in turn results in an increase in the degree of saturation. At this time, the additional shear strength provided by the matric suction may be reduced enough to trigger a shallow landslide (Fredlund and Rahardjo, 1993).

Secondly for the liquefaction, it has been clear that a transfer of intergranular stress from grains to pore water is the main mechanism. As shown in figure 3, when saturated sand is subjected to vibration, excess pore water pressure will build up, which reduce the effective confining stress. If the effective stress reduces to zero, soil will loose all of its strength and stiffness to support structures. The soil of this state will behave like a viscous fluid. After vibration stops, the soil will reconsolidated because of the dissipation of excess pore water pressure. At this time, usually a large contractive volume change occurs. The National Research Council (1985) lists eight types of failure commonly associated with soil liquefaction earthquakes:

- Sand boils, which usually result in subsidence and relatively minor damage.
- Flow failures of slopes involving very large down-slope movements of a soil mass.
- Lateral spreads resulting from the lateral displacements of gently sloping ground.
- Ground oscillation where liquefaction of a soil deposit beneath a level site leads to back and forth movements of intact blocks of surface soil.
- Loss of bearing capacity causing foundation failures.
- Buoyant rise of buried structure suck as tanks.
- Ground settlement, often associated with some other failure mechanism.
- Failure of retaining walls due to increased lateral loads from liquefied backfill soil or loss of support from liquefied foundation soils.

Moreover, in a huge earthquake including multiple earthquake vibrations in a short period of time (main shock + several big aftershocks within one year or so), liquefaction may not only happen in main shock but also happen in aftershock whose acceleration is very small, which in a normal knowledge, is not strong enough to cause liquefaction.

These big disasters are concerned to saturated-unsaturated soil mechanics. Although soil mechanics has rapidly developed in theory, it is still not enough in engineering practice. Especially unsaturated soil mechanics, many challenges still lie ahead before engineers clearly understand how best to apply unsaturated soil mechanics in engineering practice (Fredlund, D. G. 2006). In situ test is the best way to study the engineering problem, but it is not practical because of high cost and long time. So laboratory model tests are widely conducted by researchers. The biggest problem in model tests is that the model scale can not represent the real scale fully. As the development of computer technology, numerical simulation using FEM or FDM has gradually played an important role in achieving practical geotechnical solutions. In this

case, the constitutive model for soil is the key factor in numerical simulation.

To well examine and correctly predict the ground behavior in these geotechnical disasters, on the one hand a suitable constitutive model for soil should be proposed to ensure that the ground soil can be described exactly in element condition; on the other hand, a FE-FD analysis program has to be selected to make sure that the numerical simulation is reasonable. At last, model tests should be conducted with a comparison between simulation and tests results to confirm the accuracy of numerical analysis.

The main object of this dissertation contains two parts:

(1) Modeling of water-air-soil three-phase material and its application to unsaturated slope failure. First, a new constitutive model for unsaturated soil is introduced. The model is achieved by assuming that normally consolidated line in unsaturated state (*N.C.L.S.*) is parallel to the normally consolidated line in saturated state (*N.C.L.*) but in a higher position than *N.C.L.* in the void ratio-logarithmic mean skeleton stress (e-lnp) relation. In the model, which can describe the mechanical behaviors of both unsaturated and saturated soils, the skeleton stress tensor and the degree of saturation are selected to be independent state variables. Secondly, a water- air-soil three-phase model is proposed to solve unsaturated boundary value problem. The assumption that the air in the soil is always connected to atmosphere and its pressure is given as 0 is used. Third, combining the new constitutive model and proposed three-phase theory in the program named as SOFT, a simulation of one element is carried out with two different loading conditions to verify the availability of the program in simulation unsaturated problems. Finally, 2D finite element analysis was carried out to simulate the model test of unsaturated Shirasu slope failure. By comparing the calculated results to test results, the constitutive model and three-phase theory are verified.

(2) Numerical analysis in solving geotechnical problems including liquefaction. In this part, numerical simulation on three kinds of ground was carried out based on Cyclic Mobility Model (Zhang, 2007) using the program DBLEAVES (Ye, 2011). The first one is numerical test on seismic enhancement effect of improved dry sand ground pile foundation with a comparison between the simulated results and shaking table tests results; The second one is dynamic analysis of undersea soft rock to clarify the mechanism of the formation process from the proto-decollement to the decollement; The third one is liquefaction analysis of sand-silt mixed ground foundation of Knie Parking lot to evaluate the stabilities of different kinds of foundation in earthquake.

1.2 Outline of the dissertation

The composition of the dissertation is listed as follows:

Chapter 2 Constitutive model for unsaturated soil: Reviews on the development of constitutive model for unsaturated soil are presented firstly. Then a new constitutive model using skeleton stress and degree of saturation is described in detail.

Chapter 3 Using Soil-water-air three-phase mixture theory in FEM: 2D FEM approaches that consider the interaction between soil skeleton, pore water and air in one-dimensional infiltration problem is described in detail.

Chapter 4 Numerical simulation of unsaturated Shirasu slope failure and comparison with soil tank test results: 2D unsaturated-saturated soil-water-air three-phase coupled finite element analysis is conducted on model Shirasu slope. Simulation results are compared with soil tank test results to verify the proposed constitutive model and FEM method.

Chapter 5 Numerical simulation of ground improvement for group-pile foundation and comparison with shaking table test results: Numerical tests on seismic enhancement effect of existing group-pile foundation with ground improvement are first conducted to find out the optimum pattern of ground improvement around existing pile foundation. Then the efficiency of seismic enhancement by partial-ground improvement method is confirmed by shaking table tests and numerical analysis.

Chapter 6 Dynamic analyses of undersea soft rock: Simulate the undersea soft rock under high confining stress state subjecting to dynamic loading to clarify the mechanism process of the formation from proto-decollement to decollement, which is one step to the clarification of the earthquake mechanism.

Chapter 7 Evaluation of anti-seismic performance of Kanie Parking Lot based on liquefaction analysis: Analysis was carried out by 2D soil-water coupled finite element method in two cases, which are the long-pile type foundation and short-pile type foundation changed to evaluate the seismic stability of the structure and foundation.

Chapter 8 Conclusions and Remarks: The important results obtained from this research are summarized including the significant findings and the direction of future study.

References

Fredlund, D.G. and Rahardjo, H. (1993): Soil mechanics for unsaturated soils, JohnWiley, New York.

Fredlund, D.G. (2006): Unsaturated soil mechanics in engineering practice, Journal of Geotechnical and Geoenvironmental Engineering, Vol.132, No.3, 286-321.

Yeh, H.F., Chang, P.H., Chen, J.F. and Lee, C.H. (2006): Instability of unsaturated soil slopes due to infiltration.

Ye, G. L. (2011): DBLEAVES: User's manual, Version 1.6, Shanghai Jaotong University, China (In Japanese and Chinese).

Zhang, F., Ye, B., Noda, T., Nakano, M. and Nakai, K. (2007): Explanation of Cyclic Mobility of Soils: Approach by Stress-Induced Anisotropy, Soils and Foundations, Vol.47, No.4, 635-648.

PART I:

MODELING OF WATER-AIR-SOIL THREE-PHASE MATERIAL AND ITS APPLICATION TO UNSATURATED SLOPE FAILURE

CHAPTER 2 Constitutive model for unsaturated soil

2.1 Introduction

Much research has been done on the mechanical behaviors of unsaturated soils experimentally, empirically, and theoretically. Some constitutive models for unsaturated soils have been developed since the work by Alonso et al. (1990), in which Barcelona Basic Model (BBM) was proposed using LC conception and normally regarded as one of the basic model for unsaturated soils. The constitutive models based on the framework of BBM, can be found in the works such as Kohgo et al. (1993a and 1993b), Cui and Delage (1996) and Sun et al. (2000), etc. In these models, stress-suction-strain relations of unsaturated soil were considered explicitly while the degree of saturation was not considered directly. On the other hand, constitutive models considering the influence of the degree of saturation were also proposed in the same period, which can be found in the literatures such as Kato et al. (1996), Karube et al. (1997), Gallipoli et al. (2003), Sheng et al. (2004), Muraleetharan and Liu (2005), Sun et al. (2007a) and Sheng et al. (2008).

Most of the models in literatures usually use stress and suction as independent state variables. In the work by Ohno et al. (2007), however, a very interesting assumption based on various experimental results was proposed that void ratio-logarithmic effective stress relation e-ln$p$ is dependent on the degree of saturation and the dependency is modeled with a simple relation. In the model proposed by Ohno et al. (2007), therefore, only the effective stress that was defined by a combination of net stress, suction and 'effective degree of saturation', was used as state variable, based on which a Cam-clay type model for unsaturated soil was proposed. The advantage of using effective stress or skeleton stress instead of using net stress and suction as independent state variable in modeling unsaturated soils is that it is much easier and smoother to describe the behaviors of soil from unsaturated state to saturated state and vice verse if the moisture characteristics of the soil is properly described and incorporated into the constitutive model. Based on this type of model, it is possible to conduct a numerical analysis related to boundary value problems of saturated and unsaturated grounds in a unique way.

In this chapter, based on the experimental results, a constitutive model using the skeleton stress and degree of saturation as independent state variables is proposed by

Zhang (2011) for unsaturated soil, in which the influence of the degree of saturation can be properly described. Meanwhile, other mechanical features such as over-consolidation, soil structure formed in sedimentary process of the soil, and stress-induced anisotropy that are often discussed for saturated soil and can be suitably described with unique framework (Zhang et al., 2007), can also be easily considered in the same way for saturated and unsaturated states. In the proposed model, a very simple moisture characteristics curve considering moisture hysteresis of unsaturated soil is also proposed from the hint of the work by Muraleetharan and Liu (2005). The moisture characteristics curve can not only be applied to secondary drying process but also primary drying process originated from slurry soil.

2.2 Definition of effective stress

First, effective stress is defined by the concept of skeleton stress as shown in following relation,

$$\sigma_{ij}^{''} = \sigma_{ij}^{t} - U\delta_{ij} \tag{1}$$

$$U = S_r u_w + (1 - S_r) u_a \tag{2}$$

where $U$is mean pore pressure, $\sigma_{ij}^{''}$ is skeleton stress tensor, S_r is degree of saturation, σ_{ij}^{t} is total stress tensor and u_a is air pressure. Equation (1) means that the skeleton stress tensor is the difference of total stress tensor with mean pore pressure. Equation (1) can also be rewritten as

$$\sigma_{ij}^{''} = \sigma_{ij}^{t} - u_a\delta_{ij} + S_r(u_a - u_w)\delta_{ij} = \sigma_{ij}^{n} + S_r s\delta_{ij} \tag{3}$$

where $\sigma_{ij}^{n} = \sigma_{ij}^{t} - u_a\delta_{ij}$, $s = u_a - u_w$ (4)

σ_{ij}^{n} is net stress tensor and s is suction. Equation (4) is just the definition of the effective stress defined by Bishop if taking the value χ in Bishop's definition as S_r. The physical explanation for Equations (1) and (4), however, is different. For simplicity, throughout the context, the skeleton stress tensor $\sigma_{ij}^{''}$ will be abbreviated as σ_{ij} without specification in the following context.

2.3 Derivation of constitutive model

A quantitative relation for void ratio-logarithmic mean skeleton stress e-ln$p$ relation is established using the degree of saturation as a state variable. Here, it is assumed that normally consolidated line in unsaturated state (*N.C.L.S.*) is parallel to the normally consolidated line in saturated state (*N.C.L.*) but in a higher position than *N.C.L.*, as shown in Figure 1, which means that under the same mean skeleton stress, unsaturated soil can keep higher void ratio than those of saturated soil.

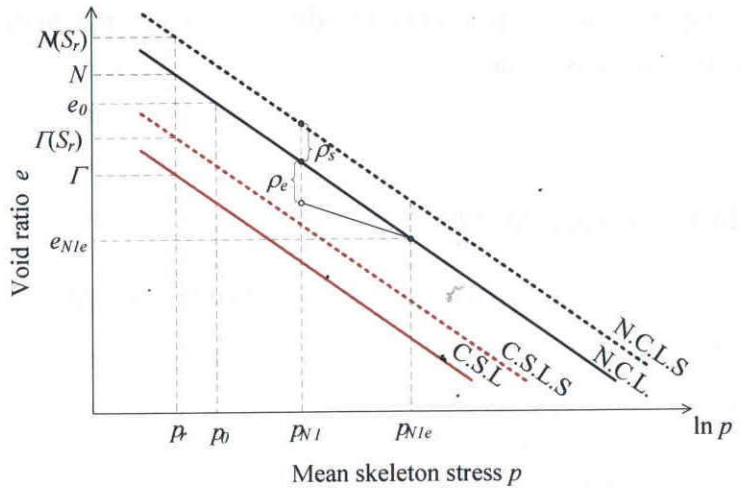

Figure 1 Illustration of e-ln$p$ relation considering moving up of *N.C.L.* and *C.S.L.* due to instauration

The *N.C.L.S.* and *C.S.L.S.* are given in the following relations as,

$$N.C.L.S.:\ e = N(S_r) - \lambda \ln \frac{p}{p_r} \quad (\eta = \frac{q}{p} = 0) \tag{5}$$

$$C.S.L.S.:\ e = \Gamma(S_r) - \lambda \ln \frac{p}{p_r} \quad (\eta = \frac{q}{p} = M) \tag{6}$$

Where, $N(S_r)$ and $\Gamma(S_r)$ are the void ratios at *N.C.L.S.* and *C.S.L.S.* under a reference mean skeleton stress p_r (Usually p_r =98kPa) and certain degree of saturation. $p = \sigma_{ii}/3$ and $q = \sqrt{3(\sigma_{ij} - p\delta_{ij})(\sigma_{ij} - p\delta_{ij})/2}$ are the mean skeleton stress and the second invariant of deviatory skeleton stress tensor. M is the stress ratio at critical state and has the same value for saturated and unsaturated states. Therefore, similar to the derivation of Cam-clay model for saturated soils, the void ratio e subjected to shearing is assumed to be,

$$e = \chi(\eta, S_r) - \lambda \ln \frac{p}{p_r} \tag{7}$$

where $\chi(\eta, S_r)$ is a function of shear stress ratio η and the degree of saturation S_r and can be expressed with simple functions as,

(i) For Cam-clay type (Roscoe et al., 1963):

$$e = N(S_r) - \frac{N(S_r) - \Gamma(S_r)}{M}\eta - \lambda \ln \frac{p}{p_r} \tag{8}$$

(ii) For Modified Cam-clay type (Schofield and Wroth, 1968):

$$e = N(S_r) - \frac{N(S_r) - \Gamma(S_r)}{\ln 2} \ln \frac{M^2 + \eta^2}{M^2} - \lambda \ln \frac{p}{p_r} \tag{9}$$

Under an saturated isotropic normally consolidated state, that is, s=0, p= p_0, η=0, S_r =1, $N = N(S_r = 1)$, e takes a value of e_0 and can be expressed as,

$$e_0 = N - \lambda \ln \frac{p_0}{p_r} \tag{10}$$

From Equations (9) and (10)

$$-\Delta e = e_0 - e = N - N(S_r) + \frac{N(S_r) - \Gamma(S_r)}{\ln 2} \ln \frac{M^2 + \eta^2}{M^2} + \lambda \ln \frac{p}{p_0} \tag{11}$$

where λ is compression index. Similar to the original Cam-Clay model, elastic change of void ratio of unsaturated soil can be calculated with swelling index κ as

$$-\Delta e^e = \kappa \ln \frac{p}{p_0} \tag{12}$$

From equations (11) and (12), it is clear that unlike most constitutive models for unsaturated soils, both the compression index and swelling index are independet from suction or degree of saturation. Elastic volumetric strain can then be calculated as,

$$\varepsilon^e_v = \frac{-\Delta e^e}{1 + e_0} = \frac{\kappa}{1 + e_0} \ln \frac{p}{p_0} \tag{13}$$

By differentiating Equation (13), the following relation can be derived,

$$d\varepsilon^e_v = \frac{\kappa}{1 + e_0} \frac{dp}{p} \tag{14}$$

Plastic part of the change of void ratio can be given as

$$-\Delta e^p = N - N(S_r) + \frac{N(S_r) - \Gamma(S_r)}{\ln 2} \ln \frac{M^2 + \eta^2}{M^2} + (\lambda - \kappa) \ln \frac{p}{p_0} \tag{15}$$

Therefore volumetric strain can also be divided into elastic and plastic parts and the plastic part can be expressed as,

$$\varepsilon_v^p = \frac{-\Delta e^p}{1+e_0} = \frac{N - N(S_r)}{1+e_0} + \frac{N(S_r) - \Gamma(S_r)}{(1+e_0)\ln 2} \ln \frac{M^2 + \eta^2}{M^2} + \frac{(\lambda - \kappa)}{1+e_0} \ln \frac{p}{p_0} \tag{16}$$

Equation (16) is only suitable for normally consolidated soil. For over consolidated soil, concept of sub loading surface proposed by Hashiguchi and Ueno (1977) can easily be applied to unsaturated soil as

$$\varepsilon_v^p = \frac{-\Delta e^p}{1+e_0} = \frac{N - N(S_r)}{1+e_0} + \frac{N(S_r) - \Gamma(S_r)}{(1+e_0)\ln 2} \ln \frac{M^2 + \eta^{*2}}{M^2} + \frac{(\lambda - \kappa)}{1+e_0} \ln \frac{p^*}{p_0} \tag{17}$$

where (p^*, q^*) represents a normally consolidated stress state through which a normal yielding surface passes, as shown in Figure 2.

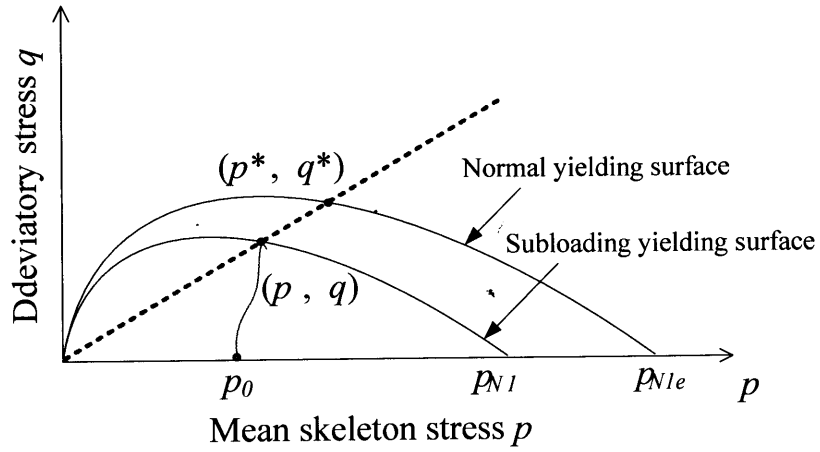

Figure 2 Extension of sub loading concept to unsaturated soil in skeleton stress space

According to the similarity between the normal yielding surface and sub-loading yielding surface, the following relations can easily be obtained.

$$\eta = \eta^* = \frac{q^*}{p^*} = \frac{q}{p}, \quad \frac{p^*}{p} = \frac{p_{N1e}}{p_{N1}} \tag{18}$$

$$\frac{p^*}{p_0} = \frac{p}{p_0}\frac{p^*}{p} = \frac{p}{p_0}\frac{p_{N1e}}{p_{N1}} \tag{19}$$

Substituting Equations (18) and (19) into Equation (17), following relation is obtained,

$$\begin{aligned} \varepsilon_v^p &= \frac{N - N(S_r)}{1+e_0} + \frac{N(S_r) - \Gamma(S_r)}{(1+e_0)\ln 2} \ln \frac{M^2 + \eta^2}{M^2} + \frac{(\lambda - \kappa)}{1+e_0} \ln \frac{p}{p_0}\frac{p_{N1e}}{p_{N1}} \\ &= \frac{N - N(S_r)}{1+e_0} + \frac{N(S_r) - \Gamma(S_r)}{(1+e_0)\ln 2} \ln \frac{M^2 + \eta^2}{M^2} + C_p \ln \frac{p}{p_0} + \frac{\rho_e}{1+e_0} \end{aligned} \tag{20}$$

where,

$$C_p = \frac{\lambda - \kappa}{1+e_0}, \quad \rho_e = (\lambda - \kappa) \ln \frac{p_{N1e}}{p_{N1}} \tag{21}$$

ρ_e represents a void ratio difference between normally consolidated state and over-consolidated state under the same mean skeleton stress. As shown in Figure 6, it is known that *N.C.L.S.* moves upward in parallel from *N.C.L.* when the degree of saturation decreases. Therefore, a new state variable ρ_s which represents a void ratio difference between *N.C.L.* and *N.C.L.S.* under the same mean skeleton stress, is expressed as,

$$\rho_s = N(S_r) - N \tag{22}$$

Equation (20) then can be rewritten as,

$$\varepsilon_v^p = C_p \ln\frac{p}{p_0} + \frac{N(S_r) - \Gamma(S_r)}{(1+e_0)\ln 2}\ln\frac{M^2+\eta^2}{M^2} - \frac{\rho_s}{1+e_0} + \frac{\rho_e}{1+e_0} \tag{23}$$

Therefore, yielding function can be written as,

$$f = \ln\frac{p}{p_0} + \frac{N(S_r) - \Gamma(S_r)}{C_p(1+e_0)\ln 2}\ln\frac{M^2+\eta^2}{M^2} - \frac{\rho_s}{1+e_0}\frac{1}{C_p} + \frac{\rho_e}{1+e_0}\frac{1}{C_p} - \varepsilon_v^p\frac{1}{C_p} = 0 \tag{24}$$

By the definition of the critical state and some algebraic calculations, it is easy to obtain a useful relation as,

$$d\varepsilon_v^p = \Lambda\left.\frac{\partial f}{\partial p}\right|_{\eta=M} = 0 \quad \Rightarrow \quad N(S_r) - \Gamma(S_r) = (\lambda - \kappa)\ln 2 \tag{25}$$

Substituting Equations (21) and (25) into Equation (24), the following relation is obtained,

$$f = \ln\frac{p}{p_0} + \ln\frac{M^2+\eta^2}{M^2} - \frac{\rho_s}{1+e_0}\frac{1}{C_p} + \frac{\rho_e}{1+e_0}\frac{1}{C_p} - \varepsilon_v^p\frac{1}{C_p} = 0$$

$$= f_\sigma + \frac{\rho_e - \rho_s}{1+e_0}\frac{1}{C_p} - \varepsilon_v^p\frac{1}{C_p} = 0 \tag{26}$$

where

$$f_\sigma = \ln\frac{p}{p_0} + \ln\frac{M^2+\eta^2}{M^2} \tag{27}$$

From consistency equation df=0, it is known that

$$df = \frac{\partial f_\sigma}{\partial \sigma_{ij}}d\sigma_{ij} - d\left(\frac{\rho_s}{1+e_0}\right)\frac{1}{C_p} + d\left(\frac{\rho_e}{1+e_0}\right)\frac{1}{C_p} - d\varepsilon_v^p\frac{1}{C_p} = 0 \tag{28}$$

In Equation(28), it is necessary to give evolution equations for the development of the state variables ρ_e of overconsolidation and ρ_s of saturation, and the flow rule for plastic strain tensor in the following ways:

(i) Associate flow rule: $d\varepsilon_{ij}^{p} = \Lambda \frac{\partial f}{\partial \sigma_{ij}}$ (29)

(ii) $d(\frac{\rho_e}{1+e_0}) = -\Lambda \frac{\rho^{\beta}}{p}, \quad \rho = a\rho_e + b\rho_s$ (30)

(iii)
$$\left\{ \begin{array}{l} N(S_r) = N + \frac{N_r - N}{S_r^s - S_r^r}(S_r^s - S_r); \quad N_r = N(S_r^r) \\ \rho_s = N(S_r) - N = Q(S_r^s - S_r); \quad Q = \frac{N_r - N}{S_r^s - S_r^r} \\ d\rho_s = -QdS_r \end{array} \right\} \quad (31)$$

Where, S_r^r and S_r^s are the degrees of saturation under residual and saturated condition.

Equation(31) means $N(S_r)$ changes linearly with the degree of saturation. Parameters *a, b* and β control the development of the state variables ρ_e. N_r is the void ratios at *N.C.L.S.* under the reference mean skeleton stress p_r when the degrees of saturation is in residual state, that is, $N_r = N(S_r^r)$

Volumetric strain increment can be divided into elastic and plastic parts as,

$$d\varepsilon_{ij} = d\varepsilon_{ij}^{e} + d\varepsilon_{ij}^{p} \quad (32)$$

Using Hooke's theory with stiffness tensor E_{ijkl}, incremental stress tensor can be expressed as,

$$d\sigma_{ij} = E_{ijkl}(d\varepsilon_{kl} - d\varepsilon_{kl}^{p}) = E_{ijkl}d\varepsilon_{kl} - E_{ijkl}\Lambda \frac{\partial f}{\partial \sigma_{kl}} \quad (33)$$

Substituting this equation into Equation(28), the following relation can be obtained,

$$\frac{\partial f}{\partial \sigma_{ij}} E_{ijkl} d\varepsilon_{kl} - \frac{\partial f}{\partial \sigma_{ij}} E_{ijkl} \Lambda \frac{\partial f}{\partial \sigma_{kl}} - \Lambda \frac{\rho^{\beta}}{p} \frac{1}{C_p} + \frac{Q}{1+e0} dS_r \frac{1}{C_p} - \Lambda \frac{1}{C_p} \frac{\partial f}{\partial \sigma_{mm}} \quad (34)$$

which resulting in,

$$\Lambda = \frac{\frac{\partial f}{\partial \sigma_{ij}} E_{ijkl}\, d\varepsilon_{kl} + \frac{1}{C_p} \frac{Q}{1+e_0} dS_r}{\frac{h_p}{C_p} + \frac{\partial f}{\partial \sigma_{ij}} E_{ijkl} \frac{\partial f}{\partial \sigma_{kl}}} \quad (35)$$

where, $h_p = \frac{\partial f}{\partial \sigma_{mm}} + \frac{\rho^{\beta}}{p}$ (36)

Therefore it is easy to define the loading criteria as,

$$\begin{cases} \Lambda > 0 & loading \\ \Lambda = 0 & neutral \\ \Lambda < 0 & unloading \end{cases} \tag{37}$$

Substituting Equation(35) into Equation(29),

$$d\varepsilon_{ij}^{p} = \frac{\dfrac{\partial f}{\partial \sigma_{mn}} E_{mnkl}\, d\varepsilon_{kl} + \dfrac{1}{C_p}\dfrac{Q}{1+e_0} dS_r}{\dfrac{h_p}{C_p} + \dfrac{\partial f}{\partial \sigma_{mn}} E_{mnkl} \dfrac{\partial f}{\partial \sigma_{kl}}} \dfrac{\partial f}{\partial \sigma_{ij}} \tag{38}$$

Meanwhile,

$$\begin{aligned} d\sigma_{ij} &= E_{ijkl}(d\varepsilon_{kl} - d\varepsilon_{kl}^{p}) \\ &= E_{ijkl}\, d\varepsilon_{kl} - E_{ijqr} E_{mnkl} \frac{\partial f}{\partial \sigma_{mn}} \frac{\partial f}{\partial \sigma_{qr}} \frac{1}{D} d\varepsilon_{kl} - \frac{1}{C_p}\frac{Q}{1+e_0} dS_r \frac{1}{D} E_{ijqr} \frac{\partial f}{\partial \sigma_{qr}} \\ &= (E_{ijkl} - E_{ijkl}^{p}) d\varepsilon_{ij} - A E_{ijkl} \frac{\partial f}{\partial \sigma_{kl}} \end{aligned} \tag{39}$$

where,

$$A = \frac{1}{C_p}\frac{Q}{1+e_0} dS_r \frac{1}{D}, \qquad D = \frac{h_p}{C_p} + \frac{\partial f}{\partial \sigma_{mn}} E_{mnkl} \frac{\partial f}{\partial \sigma_{kl}} \tag{40}$$

$$E_{ijkl}^{p} = \frac{E_{ijqr} E_{mnkl} \dfrac{\partial f}{\partial \sigma_{mn}} \dfrac{\partial f}{\partial \sigma_{qr}}}{D} \tag{41}$$

2.4 Definition of the moisture characteristic curve

In order to properly consider the influence of the degree of saturation on stress-strain-dilatancy relationships of unsaturated soils, it is necessary to give a precise description of the moisture characteristics, taking into consideration the moisture hysteresis. Therefore, a suitable moisture characteristics curve for suction-saturation relation should include skeleton curves and scanning curves so that at any moisture state (S_r, s), it is possible to obtain an incremental relation between suction and the degree of saturation as,

$$dS_r = k_s^{-1} ds \tag{42}$$

where, k_s is the tangential stiffness of suction-saturation relation.

The skeleton curves for the moisture characteristics with tangential and arc-tangential functions are given in three different ways according to the state of the moisture as,

(i) Primary drying curve from slurry:

$$S_r = S_r^{s0} - \frac{2}{\pi}(S_r^{s0} - S_r^r)\tan^{-1}((e^{c_1 s} - 1)/e^{c_1 s_d}) \tag{43}$$

or $$s = \frac{1}{c_1}\ln\left[1 + e^{c_1 s_d}\tan(\frac{\pi}{2}\frac{S_r^{s0} - S_r}{S_r^{s0} - S_r^r})\right] \tag{44}$$

(ii) Secondary drying curve experienced drying-wetting process:

$$S_r = S_r^s - \frac{2}{\pi}(S_r^s - S_r^r)\tan^{-1}((e^{c_1 s} - 1)/e^{c_1 s_d}) \tag{45}$$

or $$s = \frac{1}{c_1}\ln\left[1 + e^{c_1 s_d}\tan(\frac{\pi}{2}\frac{S_r^s - S_r}{S_r^s - S_r^r})\right] \tag{46}$$

(iii) Wetting curve:

$$S_r = S_r^s - \frac{2}{\pi}(S_r^s - S_r^r)\tan^{-1}((e^{c_2 s} - 1)/e^{c_2 s_w}) \tag{47}$$

or $$s = \frac{1}{c_2}\ln\left[1 + e^{c_2 s_w}\tan(\frac{\pi}{2}\frac{S_r^s - S_r}{S_r^s - S_r^r})\right] \tag{48}$$

where, S_d is a parameter corresponding to drying AEV and S_w is a parameter corresponding to WEV, as shown in Figure 3. c_1 and c_2 are scaling factors that controlling the shape of the curves. S_r^{s0} is the degree of saturation of a slurry under fully saturated condition and is equal to 1.0.

As to the scanning curve in the process of drying-wetting process between the skeleton curves, the incremental relation between suction and saturation is expressed as,

$$k_s^{-1} = k_{s0}^{-1} + k_{s1}^{-1} \tag{49}$$

k_{s0} is the gradient of suction-saturation relation under the condition that inner variable r equals to 0. k_{s1} is expressed as:

$$k_{s1} = k_{s1}^s(1 + c_3\frac{1-r}{r}) \tag{50}$$

where, c_3 is a scaling factor which controlling the curvature of the scanning curve. k_{s1}^s

is the gradient of the corresponding skeleton curve on which the moisture state (S_r, s) is locating under the condition that r equals to 1, as shown in Figure 3. According the illustration in Figure 8, the inner variable r is defined as,

$$r = \begin{Bmatrix} \delta_2 / \delta & ds > 0 \\ \delta_1 / \delta & ds \le 0 \end{Bmatrix} \tag{51}$$

Equation (49) means that the stiffness of k_s consists of two parts, k_{s0} and k_{s1} in a way that its value looks like the value of a spring consisted from two series springs. It is easily understood from Equations (49) and (50) that if r=0, k_{s1} will be infinite and $k_s = k_{s0}$. While if r =1 and $k_{s0} = k_{s1}^s$, k_s will equal to k_{s1}^s, which coincides with the gradient of the skeleton curve. This explanation can also be easily understood by means of the illustration shown in Figure 3.

Eight parameters are involved in the proposed moisture characteristic curve, among which three parameters c_1, c_2 and c_3 are determined with curve fitting method while other five parameters, k_{s0}, S_r^s, S_r^r, S_d and S_w have definite physical meaning and can be determined by the test of moisture characteristics easily.

Figure 4 shows a theoretical prediction of moisture characteristics curve of a fictional unsaturated silt. It is very clear that all main features of the moisture characteristics can be properly described. The values of the parameters are listed in Table 1.

Table 1 Parameters of moisture characteristics curve of unsaturated fictional silt

Saturated degrees of saturation S_r^s	0.82
Residual degrees of saturation S_r^r	0.64
Parameter corresponding to drying AEV (kPa) S_d	550
Parameter corresponding to wetting WEV (kPa) S_w	320
Initial stiffness of scanning curve (kPa) k_{sp}^e	200000
Parameter of shape function c_1	0.0080
Parameter of shape function c_2	0.013
Parameter of shape function c_3	10.0

In the area between the primary drying curve and the secondary drying curve, the upper bound for the scanning curve is changed from the secondary drying curve to the primary drying curve; and the lower bound for the scanning curve is changed from the wetting curve to a combined curve made from the wetting curve in the region $S_r \le S_r^s$

and the line $s = 0$ in the region $S_r > S_r^s$. The scanning rule, however, is totally the same as those for the secondary drying-wetting process discussed in Equations 49-51. It should be emphasized that the moisture characteristic curve is possible to describe the hysteresis relation for both saturated and unsaturated states smoothly with relative small number of parameters.

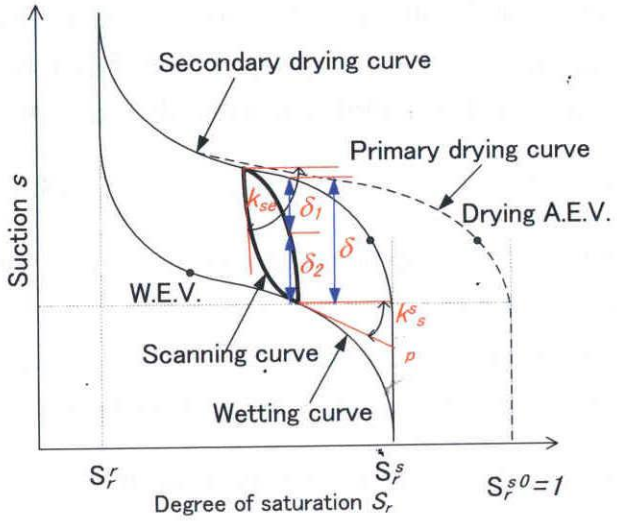

Figure 3 Image of moisture characteristic curve of unsaturated soil

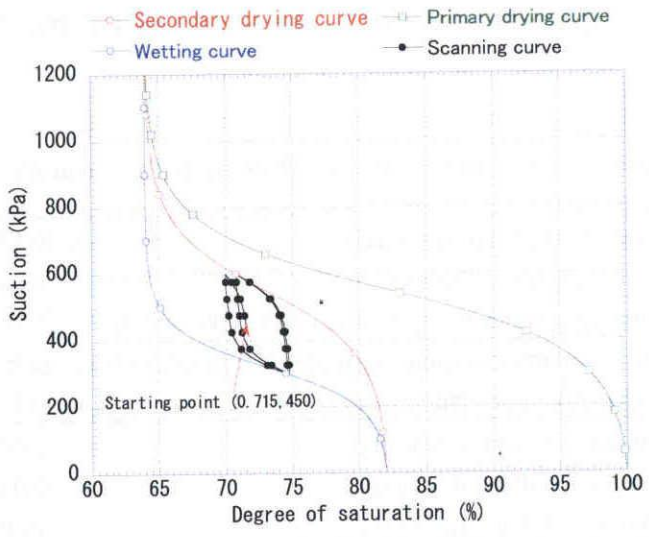

Figure 4 Simulated moisture characteristics curve of unsaturated fictional silt

2.5 Performance of the proposed model

Nine parameters are involved in the proposed model, among which five parameters, M, N, λ, κ, and ν are the same as the ones in Cam-clay model. The other three parameters a, b and β, the parameters that control the losing rate of over consolidation contributed both from the state parameters ρ_e and ρ_s when the soil subjected to shearing or compression, have clear physical meanings and can be easily determined based on conventional triaxial compression tests under drained and exhausted conditions. The ninth parameter, N_r, the void ratio at *N.C.L.S.* under $p=p_r$ and residual unsaturated state $N_r = N(S_r^r)$, is just a physical state like N.

In order to check the performance of the proposed model, fictional silt with a moisture characteristics curve shown in Figure 4, whose parameters are listed in Table 1, is simulated under different loading conditions in isotropic consolidation tests and triaxial compression tests.

2.5.1 Simulation of isotropic consolidation test

Figure 5 shows the simulated volumetric change of the normally consolidated silt subjected to different suctions in isotropic consolidation test. The loading path includes three steps as listed below:

Step I: Applying suction to the silt initially under saturated condition

Step II: Keeping the suction in a constant value and applying net mean stress from 0 to 10,000kPa

Step III: Reducing the suction to zero (submergence)

The material parameters used in the model are listed in Table 2. The correctness of the simulation is evident because so many test results have been reported in the literature. The volumetric contraction due to submergence in the Step III, however, is not completely equal to the difference between $\varepsilon_v - \ln p_{net}$ curves with suction and without suction. In the figure, mean net stress is expressed as $p_{net} = \sigma_{ii}^n / 3$.

Figure 6 shows more detailed performance of volumetric contraction due to submergence at different values of net stress in the isotropic consolidation test with a constant suction of 1500 kPa. It can be seen that a residual difference between $\varepsilon_v - \ln p_{net}$ curves with suction and without suction after the suction is completed released, is negligible at relative low net stress but will increase to some extent. The reason why this phenomenon occurs is that the development of state values ρ_e of over consolidation and ρ_s of saturation are independent. Therefore, ρ_s will be zero at the end of submergence (s=0) but ρ_e is not necessary to be zero. After the submergence completed (s=0), if a loading such as shearing continues, then according to the

definition of ρ_e, the soil will reach *C.S.L.*, where ρ_e will definitely become zero. The correctness of this independence is still need to be verified by test results. At present stage, it just predicts the possibility of the existence of the residual difference.

Table 2 Material parameters of fictional silt in odometer tests

Compression index λ	0.050
Swelling index κ	0.010
Critical state parameter **M**	1.0
Void ratio N (p'=98 kPa on *N.C.L.*)	1.14
Poisson's ratio v	0.30
Parameter of overconsolidation a	5.00
Parameter of suction b	5.50
Parameter of overconsolidation β	1.0
Void ratio N_r (p'=98 kPa on *N.C.L.S.*)	1.28

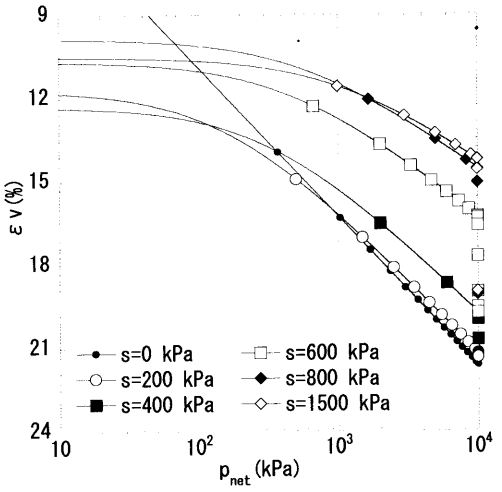

Figure 5 Simulated relations between void ratio and net stress in isotropic compression under different constant suctions.

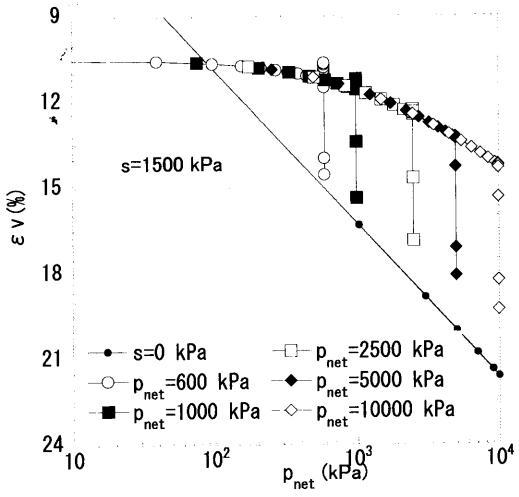

Figure 6 Simulated processes of volumetric contraction due to submergence of unsaturated soil

2.5.2 Simulation of triaxial compression tests under different suction and confining stress

Figure 7 shows the skeleton stress, strain and dilatancy relations of triaxial compression test on unsaturated silt under drained and exhausted condition under different confining stresses and suctions (Cui and Delage, 1996). Because the silt samples were statically compacted under certain vertical stress, it would be in slightly over-consolidated state if the confining stress is relatively low, e.g., σ_3=50 kPa. The results are simulated with the proposed model. Because there is no detailed data related

to moisture characteristics curve, the moisture characteristics curve of the fictional unsaturated silt shown in Figure 4 is assumed for the silt. Therefore, the following predictions by the model do not aim to describe precisely the test results but an overall behavior of the unsaturated silt qualitatively.

The material parameters of the fictional silt in triaxial tests are listed in Table 3. In simulating the triaxial compression tests, suction loading before shearing is calculated at first so that all the samples simulated are started from the same initial conditions except the state variable of overconsolidation which is dependent on veridical stress once applied in the static compaction of the samples. The initial values of state variables are listed in Table 4.

Table 3 Material parameters of fictional silt in triaxial tests

Compression index λ	0.050
Swelling index κ	0.010
Critical state parameter **M**	1.0
Void ratio N (p'=98 kPa on *N.C.L.*)	1.14
Poisson's ratio ν	0.30
Parameter of overconsolidation a	5.0
Parameter of suction b	0.50
Parameter of overconsolidation β	1.0
Void ratio N_r (p'=98 kPa on *N.C.L.S.*)	1.28

Table 4 Initial value of state variables in triaxial tests

State variable of saturation ρ_s			0.00
State variable of overconsolidation ρ_e		σ_3= 50 kPa	0.01
		σ_3=100 kPa	0.00
		σ_3=400 kPa	0.00

Figures 8～10 show the simulated skeleton stress, strain and dilatancy relations and skeleton stress paths in triaxial compression tests on unsaturated silts under drained and exhausted condition with different confining stresses. During shearing, the confining stress and the suction are kept constant. The volumetric strains shown in the figures are countered from the point on which the shearing is started.

In the case of σ_3=50 kPa, due to the slightly over consolidated condition, a typical strain hardening and strain softening accompanied by positive dilatancy can be seen in the simulated results, especially in the case of high suction. The simulated results agrees qualitatively well with the test results shown in Figure 7, though the fictional silt is not the same materials as the real silt.

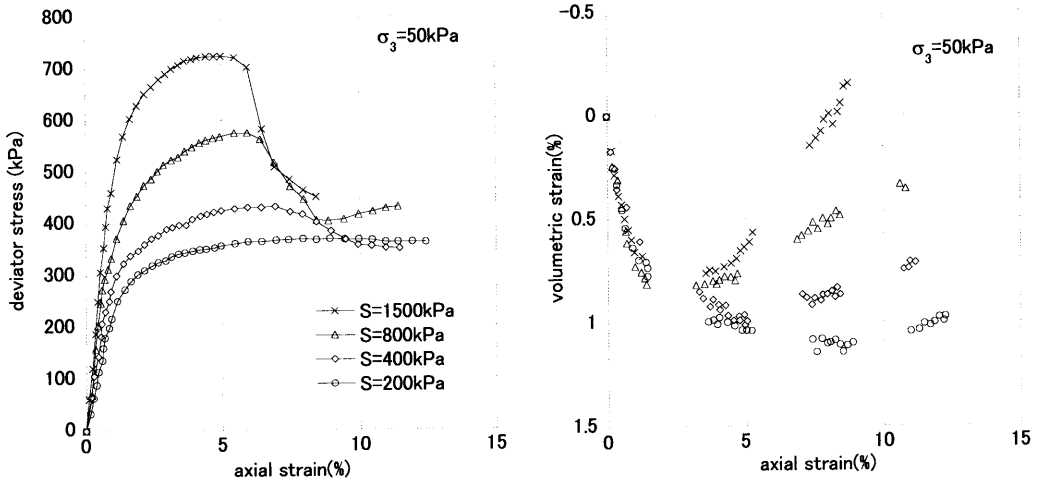

(a) σ_3=50 kPa

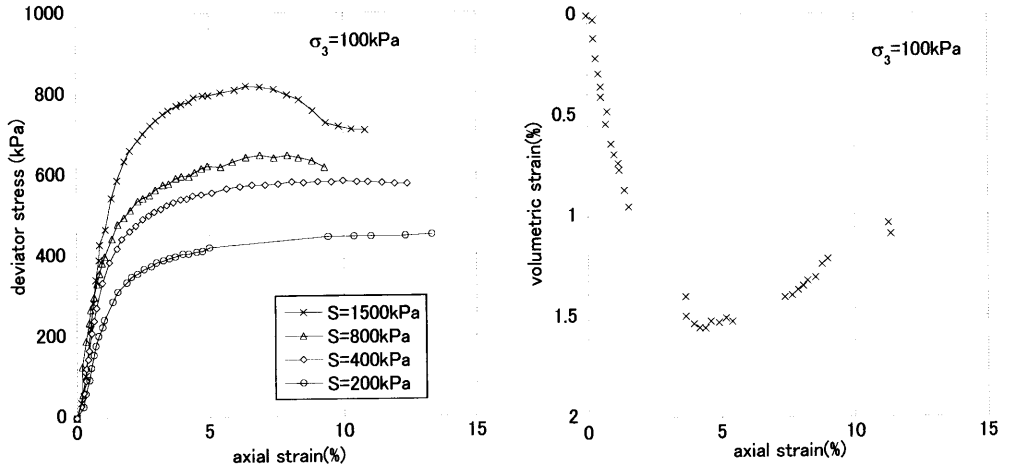

(b) σ_3=100 kPa

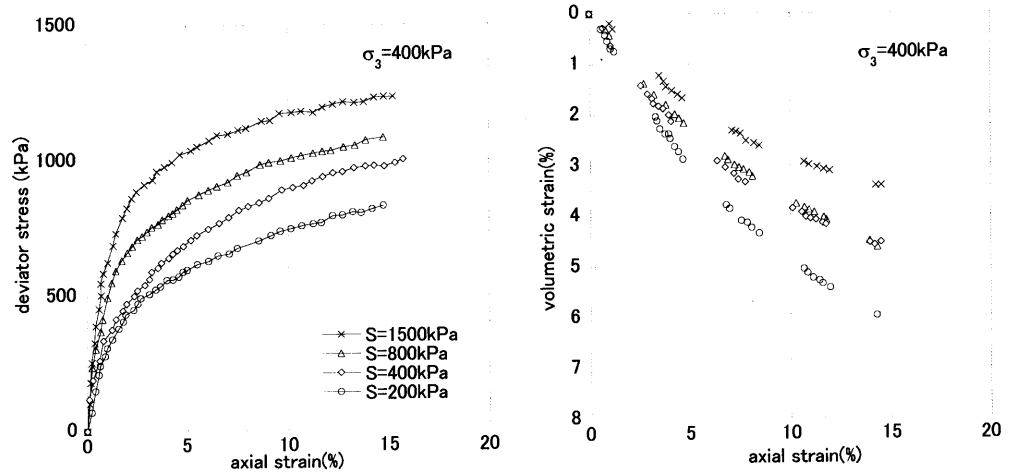

(c) σ_3=400 kPa

Figure 7 Skeleton stress, strain and dilatancy relations at different confining stresses and suctions (Cui and Delage, 1996)

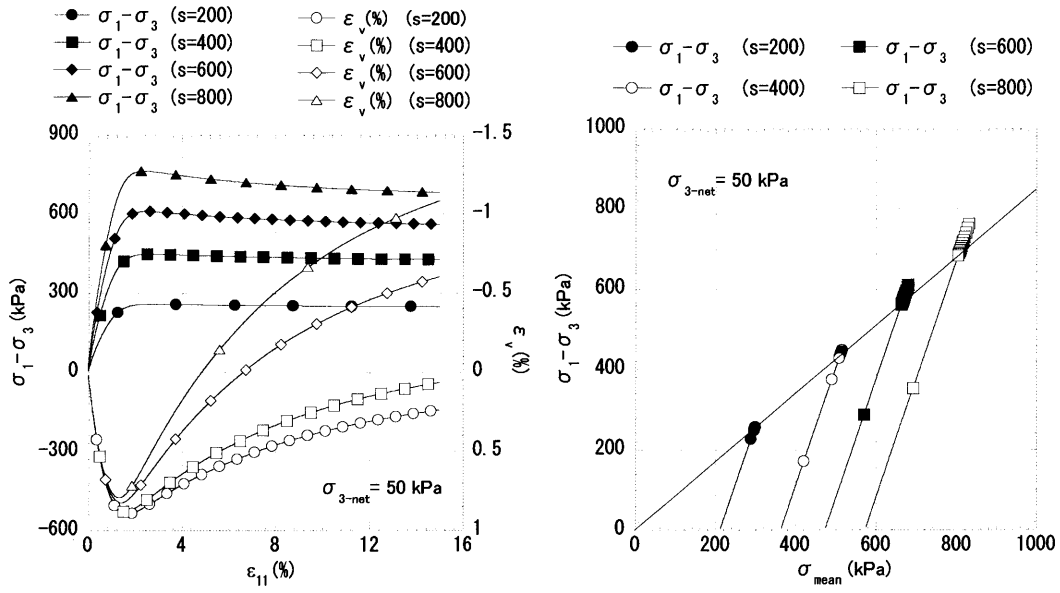

(a) Stress, strain and dilatancy relations (b) Skeleton stress Paths

Figure 8 Simulated stress, strain and dilatancy relations and skeleton stress paths (σ_3=50 kPa)

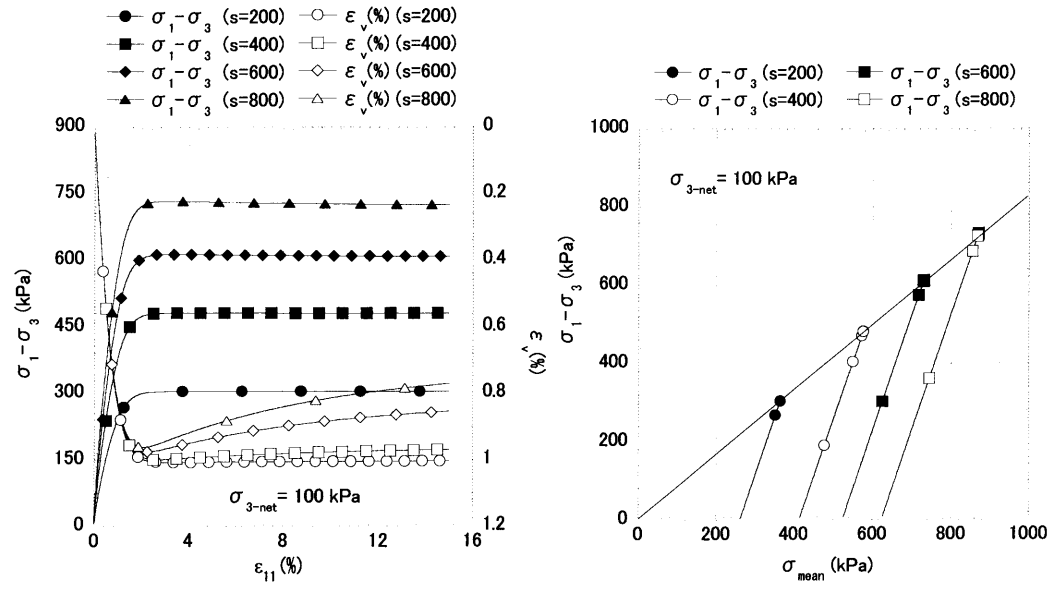

(a) Stress, strain and dilatancy relations (b) Skeleton stress Paths

Figure 9 Simulated stress, strain and dilatancy relations and skeleton stress paths (σ_3=100 kPa)

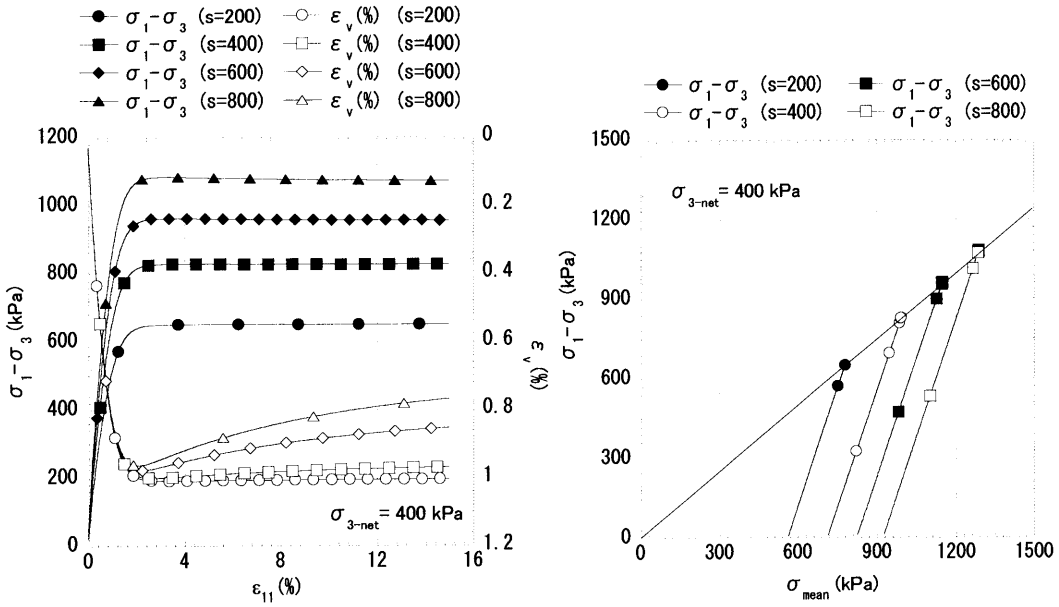

(a) Stress, strain and dilatancy relations (b) Skeleton stress Paths

Figure 10 Simulated stress, strain and dilatancy relations and skeleton stress paths (σ_3=400 kPa)

2.5.3 Simulation of collapse by submergence in triaxial compression tests

Another important phenomenon of unsaturated soil during shearing is so called collapse by submergence. In this section, collapse by submergence happened in three different shearing stages listed below is simulated:

(i) Submergence at post-peak shearing

(ii) Submergence on peak stage

(iii) Submergence at pre-peak shearing stage

Furthermore, in order to investigate the influence of submergence rate on the collapse behavior during shearing, two different submergence rates are considered in the simulation. One is gradual submergence, which is carried out with a gradual reduction of suction accompanied by simultaneous shearing till the end of the shearing test. This load process is called as loading path 1. Another is abrupt submergence, in which submergence is carried out instantly at first with a prescribed suction reduction under the condition that the vertical strain is kept constant and then the strain-controlled shearing continues under the condition that the reduced suction is kept constant. This loading process is called as loading path 2. Loading path 3 is just a normal triaxial compression test without submergence.

Figure 11 shows the simulated results of above loading paths in the case of σ_3=50

kPa, s=800 kPa. The extent of the suction reduction in above submergence processes is 50% of the original suction. It is known from the figure that no matter what kind of shearing stage at which submergence is carried out, collapse will definitely occur due to the loss of suction. Meanwhile, submergence always causes extra positive dilatancy no matter what kind of submergence it may be. Abrupt submergence always causes an immediate reduction of strength which is usually called as collapse and extra positive dilatancy. The submergence rate affects the stress-strain-dilatancy relation a lot but at the end of the shearing, they will merge to the same destination, the point at *C.S.L.S.* or *C.S.L.*, depending on the value of the suction.

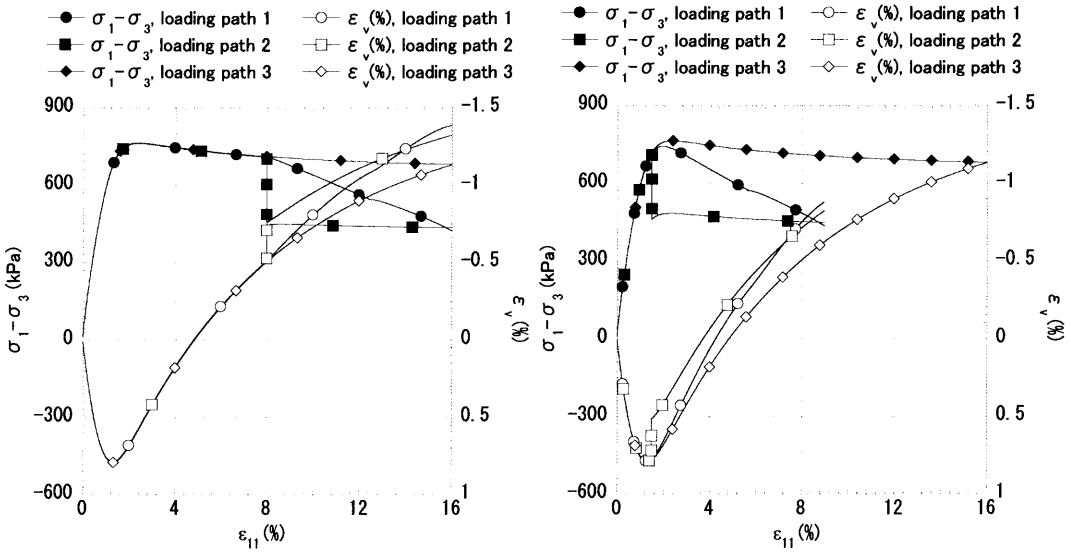

(a) Submergence at post-peak shearing stage (b) Submergence on peak stage

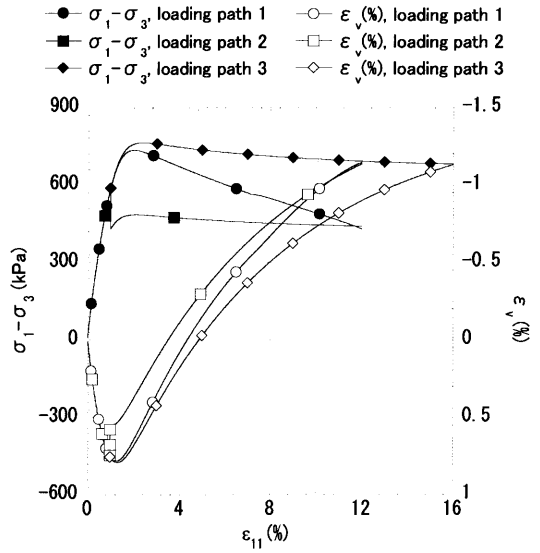

(c) Submergence at pre-peak shearing stage

Figure 11 Influence of submergence on stress, strain and dilatancy relation (σ_3=50 kPa, s=800 kPa)

Figure 12 shows the skeleton stress paths in the process of the collapse by submergence under different loading paths. In the submergence process at pre-peak shearing stage, if it is carried out abruptly, then stress path will approach the residual line in the region below the line. Otherwise, stress state will always overpass the line and finally reaches the critical state.

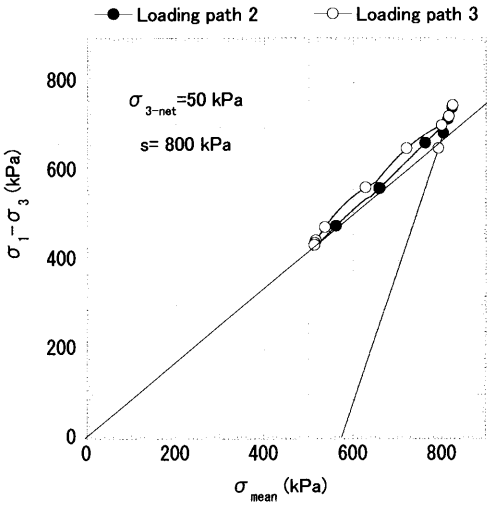

(a) Submergence at post-peak shearing stage

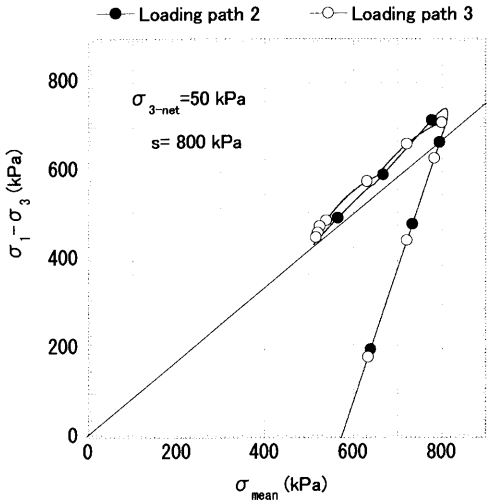

(b) Submergence on peak stage

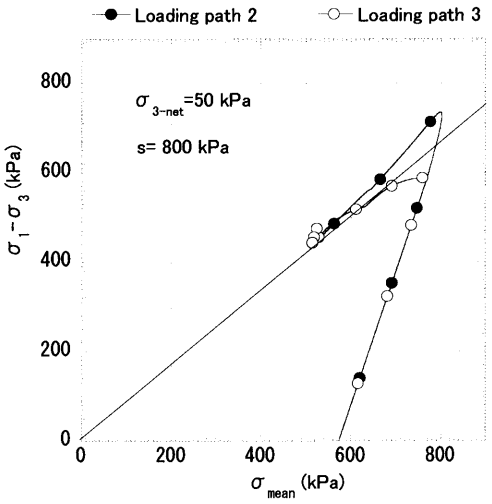

(c) Submergence at pre-peak shearing stage

Figure 12 Influence of submergence on skeleton stress path

2.5.4 Verification of the model by drained and exhausted triaxial compression tests for a rockfill with submergence process

Kohgo et al (2007b) conducted a systematic laboratory test on rock fill materials with drained and exhausted triaxial compression tests including submergence process to investigate the influence of the degree of saturation on mechanical behavior of the rock fill. Detailed description about the tests can be found in the reference. The size of the test specimen is 30 cm in diameter and 60 cm in height. Figure 13 shows the test and simulated moisture characteristics curve of the unsaturated rock fill. The parameters involved in the moisture characteristics curve are listed in Table 5.

In the drained and exhausted triaxial compression tests under constant confining pressure, three kinds of tests were conducted for the rock fill, that is, tests for saturated specimen, tests for unsaturated specimen with constant suction and tests for unsaturated specimen with submergence process. Table 5 listed the material parameters involved in the proposed model, among which, apart from the parameters a, b and β, other parameters are determined based on the laboratory tests. Figure 14 shows the comparison between the test and simulated results of the drained and exhausted triaxial compression tests for the rock fill. The accuracy of the model is quite good comparing with its parameters used.

Table 5 Parameters of moisture characteristic curve of unsaturated rock fill

Saturated degrees of saturation S_r^s	0.85
Residual degrees of saturation S_r^r	0.20
Parameter corresponding to drying AEV (kPa) S_d	2.0
Parameter corresponding to wetting WEV (kPa) S_w	0.07
Initial stiffness of scanning curve (kPa) k_{sp}^e	700
Parameter of shape function c_1	0.05
Parameter of shape function c_2	0.05
Parameter of shape function c_3	10.0

Table 6 Material parameters of rock fill

Compression index λ	0.14
Swelling index κ	0.0010
Critical state parameter **M**	1.7
Void ratio N (p'=98 kPa on *N.C.L.*)	0.61
Poisson's ratio ν	0.30
Parameter of overconsolidation a	5.0
Parameter of suction b	0.50
Parameter of overconsolidation β	3.0
Void ratio N_r (p'=98 kPa on *N.C.L.S.*)	0.80

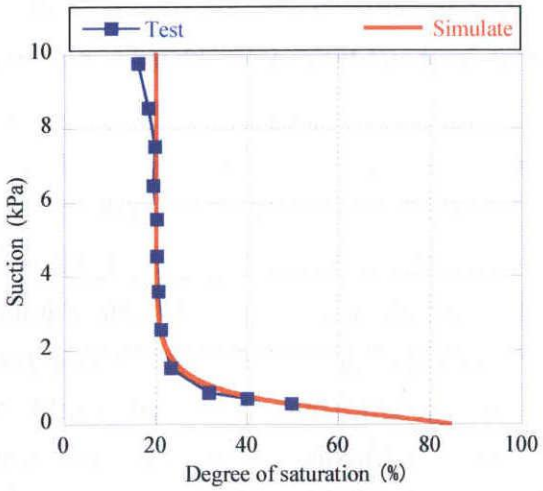

Figure 13 Test and simulated moisture characteristic curve of unsaturated rock fill (test data from the work by Kohgo et al, 2007b)

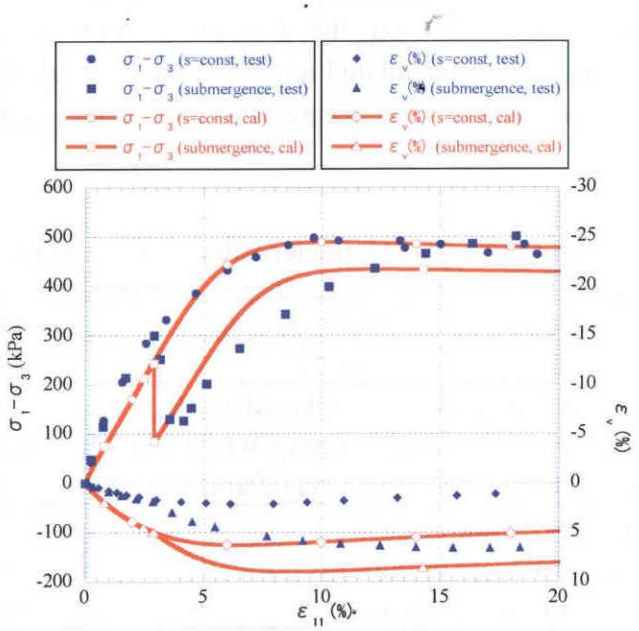

(a) Stress, strain and dilatancy relation (σ_3=100kPa)

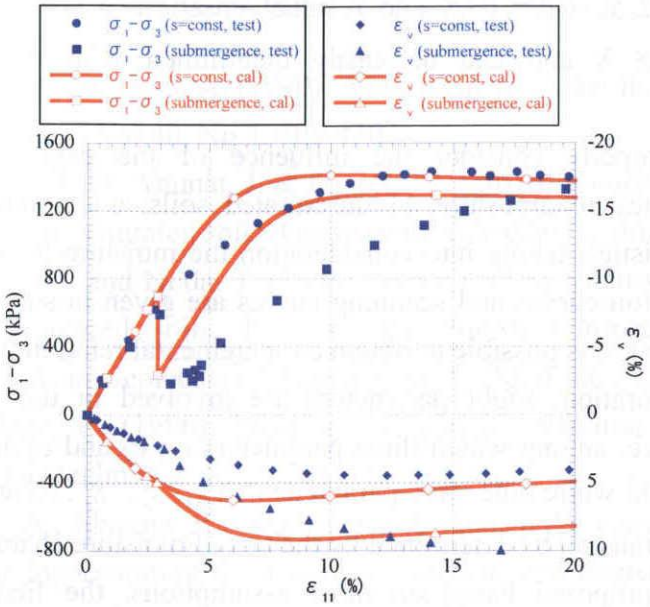

(b) Stress, strain and dilatancy relation (σ_3=300kPa)

Figure 14 Verification of the model by drained and exhausted triaxial compression tests for a rock fill with submergence process (test data from the work by Kohgo et al, 2007b)

From above discussion, it is concluded that collapse by submergence can be properly described by the proposed model.

2.6 Summary

In this chapter, a new constitutive model for unsaturated soil based on the framework of skeleton stress and degree of saturation proposed by Zhang (2011) is introduced in detail. The constitutive model is therefore possible to be able to describe not only the behaviors of unsaturated soil but also saturated soil because the skeleton stress can smoothly shift to effective stress if saturation changes from unsaturated condition to saturated condition. The main features of the proposed model can be given as below:

The proposed model is very simple and is derived from the base of modified Cam-clay model. It has nine parameters, among which five are the same as those in the Cam-clay model and are familiar to most geotechnical researchers. The other three parameters a, b and β, the parameters that control the losing rate of overconsolidation affected by the state parameter of overconsolidation ρ_e and saturation ρ_s, have clear physical meanings and can be easily determined based on conventional triaxial compression tests under drained and exhausted conditions. The ninth parameter, N_r, the

void ratio at *N.C.L.S.* under $p=p_r$ and residual unsaturated state $N_r = N(S_r^r)$, is just a physical state like N and can be easily determined with the test of moisture characteristics.

In order to properly consider the influence of the degree of saturation on stress-strain-dilatancy relationships of unsaturated soils, a theoretical description of moisture characteristics, taking into consideration the moisture hysteresis is proposed, in which the skeleton curves and scanning curves are given in such a way that at any moisture state (S_r, s), it is possible to obtain an incremental relation between suction and the degree of saturation. Eight parameters are involved in the proposed moisture characteristics curve, among which three parameters c_1, c_2 and c_3 are determined with curve fitting method while other five parameters, k_{s0}, S_r^s, S_r^r, S_d and S_w have definite physical meaning and can be determined by the test of moisture characteristics easily.

The model is proposed based on three assumptions, the first is that normally consolidated line in unsaturated state (*N.C.L.S.*) is parallel to the normally consolidated line in saturated state (*N.C.L.*) but in a higher position than *N.C.L.*, which means that under the same mean skeleton stress, unsaturated soil can keep higher void ratio than those of saturated soil. The second is that no matter what kind condition of saturation may be, compression index λ and swelling index κ in void ratio-skeleton stress relation are always kept constant which makes the model very simple and easily understood. The third is that the shear stress ratio η at critical state will be unique no matter what kind condition of saturation may be. All these assumption can be confirmed with the tests results available in literatures.

Skeleton stress, strain and dilatancy relations and skeleton stress paths in triaxial compression tests on unsaturated fictional silt under drained and exhausted condition with different confining stresses are also simulated. The overall behaviors of unsaturated soil under normally consolidated and over consolidated states can be described uniquely within the framework of skeleton stress and saturation. The collapse of unsaturated soil due to submergences at the stages of pre-peak, on-peak and post-peak of stress-strain relation is also simulated. It is known from the simulation that whenever submergence happens, collapse will always occur and causes extra positive dilatancy. Furthermore, abrupt submergence always causes an immediate collapse and extra positive dilatancy. The submergence rate affects the stress-strain-dilatancy relation a lot but at the end of the shearing, they will merge to the same destination, that is, the same point at critical state line.

References

Alonso, E. E., Gens, A. and Josa, A. (1990): A constitutive model for partially saturated soils, Geotechnique, Vol.40, No.3, 405-430.

Alonso, E. E., Pereira, M. J., Vaunat, J. & Plivella, S. (2010). A microstructurally-based effective stress for unsaturated soils, Geotechnique, Vol.60 (in printing).

Asaoka, A., Nakano, M. and Noda. T. (1998): Super loading yield surface concept for the saturated structured soils, Proc. of the Fourth European Conference on Numerical Methods in Geotechnical Engineering-NUMGE98, 232-242.

Cui, Y. J. and Delage, P., (1996): Yielding and plastic behaviour of an unsaturated compacted silt, Geotechnique, 46(2), 291-311

Gallipoli. D., Gens, A., Sharma, R., and Vaunat, J. (2003): An elastoplastic model for unsaturated soil incorporating the effects of suction and degree of saturation on mechanical behaviour. Geotechnique, 53(1): 123-135.

Gallipoli, D., Gens A., Chen, D. J. and D'Onza, F. (2008) Modelling unsaturated soil behaviour during normal consolidation and at critical state, Computers and Geotechnics, Vol.35, 825–834.

Hashiguchi, K. and Ueno, M. (1977): Elastoplastic constitutive laws of granular material, Constitutive Equations of Soils, Pro. 9th Int. Conf. Soil Mech. Found. Engrg., Spec. Ses. 9, Murayama, S. and Schofield, A. N. (eds.), Tokyo, JSSMFE, 73-82.

Hashiguchi, K., Chen, Z. P. (1998): Elastoplastic constitutive equations of soils with the subloading surface and the rotational hardening. Int. J. Numer. Anal. Meth. Geomech. 22, 197–227.

Honda, M. (2000): Research on the prediction methods for the mechanical behaviors of unsaturated soils, Doctoral Dissertation, Kobe University.

Ikariya, T. (2009): Research on mechanical behavior of unsaturated soil, Master Thesis, Nagoya Institutive of Technology (in Japanese)

Kanazawa, S., Tachibana, S., Kawai,K., Ohno, S. and Iizuka, A. (2008): Study of spatial discretization scheme in unsaturated soil/water coupled analysis, Applied Mechanics, JSCE, Vol.11, 331-338 (in Japanese).

Karube, D., Honda, M., Kato, S. and Tsurugasaki, K. (1997): The relationship between shearing characteristics and the composition of pore-water in unsaturated soil, JSCE, No.575/III-40, 49-58 (in Japanese).

Kato, S., Karube, D., Honda, M. and Fujiwara, T. (1996): Influence of water distribution on the compression behavior of unsaturated soil, JSCE, No.554/III-37, 57-69 (in Japanese).

Khalili1, N., Geiser, F. and Blight, G. E. (2004) Effective Stress in Unsaturated Soils: Review with New Evidence, Int. J. Geomechanics, ASCE, Vol.4, No.2,115-126.

Khalili, N. and Zargarbashi, S. (2010): Influence of hydraulic hysteresis on effective stress in unsaturated soils, Geotechnique, Vol.60 (in printing)

Kodaka, T., Suzuki, H. and Oka, F., (2006): Conventional triaxial compression tests for unsaturated silt under drained and exhausted condition, Proc. 18th Conf. of Geotechnical Engineering in Chubu Branch of JGS, 53-58 (in Japanese).

Kohgo, Y., Nakano, M. and Miyazaki, T. (1993a): Theoretical Aspects of constitutive model for unsaturated soils, Soils and Foundations, Vol.33, No.4, 49-63.

Kohgo, Y., Nakano, M. and Miyazaki, T. (1993b): Verification of the generalized elastoplastic model for unsaturated soils, Soils and Foundations, Vol.33, No.4, 64-73.

Kohgo, Y., Asano, I. and Hayashida, Y. (2007a). An elastoplastic model for unsaturated rockfills and its simulations of laboratory tests, Soils and Foundations, Vol.47 No.5, 919-929.

Kohgo, Y., Asano, I. and Hayashida, Y. (2007b). Mechanical properties of unsaturated low quality rockfills, Soils and Foundations, Vol.47 No.5, 947-959.

Lu, N., Godt, J. W. & Wu, D. T. (2010). A closed form equation for effective stress in unsaturated soils, Water Resources Res., Vol.46 (in printing).

Muraleetharan, K. K. and C. Liu (2005): A comprehensive approach to modeling the behavior of unsaturated soil using an elastoplastic framework, Geomechanics II, Testing, Modeling and Simulation, Geotechnical Special Publication No.156, ASCE, 515-527.

Ohno, S., Kawai, K. and Tachibana, S. (2007): Elasto-plastic constitutive model for unsaturated soil applied effective degree of saturation as parameter expressing stiffness, JSCE, Vol.63, No.4, 1132-1141 (in Japanese).

Russell, A. R. and Khalili, N. (2006): A unified bounding surface plasticity model for unsaturated soils, Int. J. Numer. Anal. Meth. Geomech., Vol.30, 181–212.

Roscoe, K. H., Schofield, A. N. and Thurairajah, A. (1963): Yielding of clays in states wetter than critical, Geotechnique, Vol.13, No.3, 250-255.

Schofield, A.N. and Wroth, C. P. (1968): Critical State Soil Mechanics, McGraw-Hill.

Sekiguchi, H. (1977): Rheological characteristics of clays, Proc. 9th Int. Conf. Soil Mech., Found. Eng., Tokyo, Vol.1, 289-292.

Sheng, D., Fredlund, D. G. and Gens. A. (2008): A new modelling approach for unsaturated soils using independent stress variables, Canadian Geotechnique, No.45, 511-534.

Sun, D. A., Matsuoka, H., Yao, Y. P. and Ichihara, W. (2000): An elasto-plastic model for unsaturated soil in three-dimensional stresses, Soils and Foundations, Vol.40, No.3, 17-28.

Sun, D.A., Matsuoka, H., and Xu, Y. F. (2004): Collapse behavior of compacted clays in suction-controlled triaxial tests, Geotechnical Testing Journal, 27(4): 362-370.

Sun, D. A., Sheng, D., and Sloan, S. W. (2007a): Elastoplastic modelling of hydraulic and stress-strain behaviour of unsaturated soil. Mechanics of Materials, 39(3): 212-221.

Sun, D. A., Sheng, D., and Xu, Y. F. (2007b): Collapse behaviour of unsaturated compacted soil with different initial densities. Canadian Geotechnical Journal, 44(6): 673-686.

Zhang, F., YE, B., Noda, T., Nakano, M., and Nakai, K. (2007): Explanation of Cyclic mobility of soils: approach by stress-induced anisotropy, Soils and Foundations, Vol.47, No.4, 635-648.

Zhang, F. and Ikariya T. (2011): A new model for unsaturated soil using skeleton stress and degree of saturation as state variables, Soils and Foundations, Vol.51, No.1, 67-81.

CHAPTER 3 Finite element method for coupled of soil · water · air three-phase mixture

3.1 Introduction

The accurate prediction of propagation of the surface infiltration in an unsaturated soil is practically important to many geotechnical and geoenvironmental problems. In unsaturated boundary value problems, it is of great significance to provide a water-air-soil three phase field theory. Oka et al. (1994) proposed a soil-water coupling two-phase field theory with u-p formulation, in which the displacement of the solid u and the pore water pressure p are used as unknown variables. Moreover, in the discretization of the governing equations in space, both FEM (Finite Element Method) and FDM (Finite Difference Method) are used. FEM is used for the discretization of the equation of motion for the mixture, and FDM is used for the discretization of the continuity equation for the pore fluid (Ye, 2007). Uzuoka et al (2007, 2008 and 2010) has proposed soil-water-air three-phase field theory, which works effectively for slope stability problems in unsaturated soils. Such type of soil-water-air three-phase field theory can also be seen in the work by Li, et al (2004) and Borja R. (2005).

In another hand, many finite element programs are available for analyses of unsaturated boundary value problems. For example, the software program SEEP/W is a popular program for such seepage analyses among geotechnical engineers (Fredlund and Rahardjo, 1993). In this chapter, the soil-water-air coupled three-phase mixture theory based on the work by Uzuoka et al (2007, 2008 and 2010) is incorporated in the program named as SOFT. As to the continuity equation, a backward finite difference scheme (Akai and Tamura, 1978) is adopted for water-air flow. Four-node quadrilateral element is used in the 2D calculation, and one pore water-pore air pressure is defined at the center of each element.

3.2 Soil-water-air three –phase field theory and FE-FD algorithm of field equations

Before the derivation of the three-phase field theory, the following assumptions should be list out:

(1) Soil grains and water are incompressible.

(2) The distribution of porosity in space and time is very small comparing to other variables.

(3) The three-phase field theory is proposed to solve static problem and the accelerations of the three phases are supposed to be 0.

3.2.1 Basic equation of mixture

The detailed derivation of soil-water two-phase equations can be referred to the work by Oka et al. (1994). While the soil-water-air three-phase equations can be referred to the work by Uzuoka et al (2007 and 2008), Uzuoka (2010), Li et al (2004) and Borja R. (2005). Here these equations are directly written in the following:

Equilibrium equation

$$\frac{\partial \sigma_{ij}}{\partial x_j} + \rho b_i = 0 \tag{52}$$

Continuity equation of water

$$S_r \dot{\varepsilon}_{ii}^s - \frac{k^w}{\gamma^w}\frac{\partial^2 p^w}{\partial x_i \partial x_i} - \frac{nS_r}{K^w}\dot{p}^w + n\dot{S}_r = 0 \tag{53}$$

Continuity equation of air

$$(1-S_r)\dot{\varepsilon}_{ii}^s - \frac{k^a}{\gamma^a}\frac{\partial^2 p^a}{\partial x_i \partial x_i} + n(1-S_r)\frac{1}{K^a}\dot{p}^a - n\dot{S}_r = 0 \tag{54}$$

Where b_i is body force, S_r is degree of saturation, K is the volumetric elastic coefficient, k is permeability, p is fluid pressure, n is porosity, and the superscript of s, w and a in the above equation denotes the solid, water and air phase respectively.

For simplicity, it is assumed that the air in the soil is always connecting to atmosphere and its value is given as 0 in this paper, therefore the continuity equation of air can be satisfied automatically in general.

3.2.2 Discretization of equilibrium equation

By using virtual work theorem, the weak form of the equilibrium equation in an arbitrary region v can be expressed as following

$$\int_V \left(\frac{\partial \sigma_{ij}}{\partial x_j} + \rho b_i \right) \delta u_i^s dV = 0 \tag{55}$$

Here, δu_i^s is the arbitrary virtual displacement.

Based on Gaussian's theory and boundary condition, Equation(55) can be changed as

$$\int_V \sigma_{ij}\delta\varepsilon_{ij}^s dV = \int_V \rho b_i \delta u_i^s dV + \int_S T_i \delta u_i^s dS \tag{56}$$

Where, T_i is surface force, $\delta\varepsilon_{ij}^s$ is the arbitrary virtual strain.

The effective stress for unsaturated soil is expressed as,

$$\sigma_{ij} = \sigma_{ij}^{'} + S_r p^w + (1-S_r)p^a = \sigma_{ij}^{'} + S_r p^w \tag{57}$$

Substituting Equation(57) into Equation(56), the following equation can be obtained

$$\int_V (\sigma_{ij}^{'} + S_r p^w)\delta\varepsilon_{ij}^s dV = \int_V \rho b_i \delta u_i^s dV + \int_S T_i \delta u_i^s dS \tag{58}$$

The incremental form of the above equation in finite element scheme can be written as follow:

$$\begin{aligned}&\int_V \Delta\sigma_{ij}'\delta\varepsilon_{ij}^s dV + \int_V \Delta(S_r p^w)\delta\varepsilon_{ii}^s dV \\ &= \int_V \rho\Delta b_i \delta u_i^s dV + \int_S \Delta T_i \delta u_i^s dS\end{aligned} \tag{59}$$

In the proposed program, Different shape function for displacement and pore water pressure in FEM discretization is used. The variables of displacement are given at the nodes and the variables of pore water pressure are given at the gravitational center.

For one element, $\vec{u}_N$ is denoted as the displacement vector of all nodes, and p_{dE} is denoted as the excessive pore water pressure at gravitational center. The displacement vector of any arbitrary point within this element, u^s can be expressed by the displacement vector of nodes $\vec{u}_N$

$$u^s = [N]\vec{u}_N \tag{60}$$

$$\delta u^s = [N]\delta\vec{u}_N \tag{61}$$

Here, $[N]$ is shape function matrix. The strain vector of any arbitrary point within an element can be written as

$$\varepsilon^s = [L]u^s = [L][N]\{u_N\} = [B]\{u_N\} \tag{62}$$

$$\delta\varepsilon_{ii}^s = \delta\varepsilon_v^s = \vec{B}_v^T\{\delta u_N\} = \{\delta u_N\}\vec{B}_v \tag{63}$$

Where, $[B_i]=\begin{bmatrix} N_{i,x} & 0 \\ 0 & N_{i,y} \\ N_{i,y} & N_{i,x} \end{bmatrix}$, $[B]=[B_1 \cdots B_i \cdots B_n]$

On the one hand, the constitutive model used in the program with vector form can be written as

$$\Delta\sigma' = [D]^{ep}[B]\{u_N\} - E^{RFS}\Delta S_r \tag{64}$$

Where, $E^{RFS} = \frac{1}{C_p}\frac{Q}{1+e_0}\frac{1}{\tilde{D}}[D]^e\frac{\partial f}{\partial\sigma}$, $[D]^e$ and $[D]^{ep}$ are the elastic matrix stiffness and elasto-plastic matrix stiffness respectively (Zhang, 2011).

Because the virtual displacement is arbitrary, combining Equation(60),(61),(62),(63) and (64), Equation(59) with vector form can be expressed

$$\begin{aligned}&\int_V [B]^T [D]^{ep}[B]dV\cdot\Delta\vec{u}_N - \int_V [B]^T\cdot E^{RFS}dV\cdot\Delta S_r \\ &+\int_V \vec{B}_v\Delta(S_r p_{dE}^w)dV = \int_V \rho[N]^T\Delta\vec{b}dV + \int_S [N]^T\Delta\vec{T}dS\end{aligned} \tag{65}$$

By defining the following equations

$$\Delta\vec{F} = \int_V \rho[N]^T\Delta\vec{b}dV + \int_S [N]^T\Delta\vec{T}dS \tag{66}$$

$$[K] = \int_V [B]^T[D][B]dV \tag{67}$$

$$\vec{K}_{Sat} = \int_V [B]^T\vec{E}^{RFS}dV \tag{68}$$

$$\vec{K}_v = \int_V \vec{B}_v dV \tag{69}$$

Equation(65) can be rewritten as

$$[K]\Delta\vec{u}_N - \vec{K}_{Sat}\Delta S_r + \vec{K}_v\Delta(S_r p_{dE}^w) = \Delta\vec{F} \tag{70}$$

The incremental form of $\Delta(S_r p_{dE}^w)$ is approximated as

$$\begin{aligned}&\Delta(S_r p_{dE}^w) = \Delta S_r p_{dE}^w + S_r\Delta p_{dE}^w \\ &= \Delta S_{r|t+\Delta t} p_{dE|t}^w + S_{r|t}\Delta p_{dE|t+\Delta t}^w\end{aligned} \tag{71}$$

$$\Delta S_{r|t+\Delta t} = S_{r|t+\Delta t} - S_{r|t} \tag{72}$$

On the other hand, in the work by Zhang (2011), a new moisture characteristics curve

(MCC) is also proposed, where the relationship between the incremental suction and saturation is expressed as

$$\Delta S_r = k_s^{-1} \Delta s \tag{73}$$

Where, k_s^{-1} is the stiffness of saturation-suction relationship.

Substituting Equation(71) and (73) into Equation(70),

$$[K]\Delta\vec{u}_N + \vec{K}_v S_r \Delta p_{dE}^w + (\vec{K}_v p_{dE}^w - \vec{K}_{Sat}) \cdot k_s^{-1} \cdot \Delta s = \Delta\vec{F} \tag{74}$$

The discretization of Equation(74) in time can be written as

$$\begin{aligned} &[K]\Delta\vec{u}_{N|t+\Delta t} + \vec{K}_v S_{r|t} \Delta p_{dE|t+\Delta t}^w + \\ &(\vec{K}_v p_{dE|t}^w - \vec{K}_{Sat}) k_s^{-1} \cdot \Delta s_{|t+\Delta t} = \Delta\vec{F}_{|t+\Delta t} \end{aligned} \tag{75}$$

Because

$$\begin{aligned} \Delta s_{|t+\Delta t} &= s_{|t+\Delta t} - s_{|t} = (-p_{dE|t+\Delta t}^w) - (-p_{dE|t}^w) \\ &= p_{dE|t}^w - p_{dE|t+\Delta t}^w \end{aligned} \tag{76}$$

Finally substituting Equation(76) into Equation(75), the discretization of equilibrium equation in space and time can be obtained

$$[K]\Delta\vec{u}_{N|t+\Delta t} + \vec{F}_{Sat} p_{dE|t+\Delta t}^w = \Delta\vec{F}_{|t+\Delta t} + \vec{F}_{Sat} p_{dE|t}^w \tag{77}$$

Where, $\vec{F}_{Sat} = \vec{K}_v S_{r|t} - (\vec{K}_v p_{dE|t}^w - \vec{K}_{Sat}) \cdot k_s^{-1}$

3.2.3 Discretization of continuity equation

The discretization of continuity equation can be implemented by the same way and written as

$$\begin{aligned} &\int_V \frac{\gamma^w}{k^w} S_r \vec{B}_v^T \vec{u}_N dV - \int_V \cdot \frac{\partial^2 p_{dE}^w}{\partial x_i \partial x_i} dV \\ &- \int_V \frac{\gamma^w}{k^w} \frac{n S_r}{K^w} \dot{p}_{dE}^w dV + \int_V \frac{\gamma^w}{k^w} n \dot{S}_r dV = 0 \end{aligned} \tag{78}$$

As to continuity equation, a backward finite difference scheme (Akai and Tamura, 1978) is adopted for water flow. So the term of $\int_V \cdot \frac{\partial^2 p_{dE}^w}{\partial x_i \partial x_i} dV$ can be expressed as

$$\int_V \frac{\partial^2 p_{dE}^w}{\partial x_i \partial x_i} dV = \alpha p_{dE}^w - \sum_{i=1}^{6} \alpha_i p_{idE}^w \tag{79}$$

$\alpha = \sum_{i=1}^{4} \frac{S_i}{b_i}, \alpha_i = \frac{S_i}{b_i}$

Where, , S_i is center-to center distance of an arbitrary element to its i^{th} neighboring element, b_i is drainage area of an arbitrary element in edge i.

By defining the following equations

$$\int_V \frac{\gamma^w n S_r}{k^w \cdot K^w} dV \cdot \dot{p}^w_{dE} = \frac{\gamma^w n S_r}{k^w \cdot K^w} \cdot \bar{V} \cdot \dot{p}^w_{dE} = A \cdot \dot{p}^w_{dE} \tag{80}$$

$$\int_V \frac{\gamma^w n}{k^w} dV \cdot \dot{S}_r = \frac{\gamma^w n}{k^w} \cdot \bar{V} \cdot \dot{S}_r \tag{81}$$

Equation(78) can be rewritten as

$$\frac{\gamma^w}{k^w} S_r \vec{K}_v^T \ddot{\vec{u}}_N - \alpha p^w_{dE} + \sum_{i=1}^{6} \alpha_i p^w_{idE} - A\dot{p}^w + \frac{\gamma^w}{k^w} n\dot{S}_r \cdot \bar{V} = 0 \tag{82}$$

Because

$$\ddot{\vec{u}}_{N|t+\Delta t} = \frac{\Delta \vec{u}_{N|t+\Delta t}}{\Delta t}, \dot{p}^w_{dE|t+\Delta t} = \frac{p^w_{dE|t+\Delta t} - p^w_{dE|t}}{\Delta t}$$
$$\dot{S}_{r|t+\Delta t} = \frac{S_{r|t+\Delta t} - S_{r|t}}{\Delta t} = \frac{\Delta S_{r|t+\Delta t}}{\Delta t} \tag{83}$$

And substituting Equation(73),(76) and (83) into Equation(82), the continuity equation in time can be written as

$$S_{r|t} \vec{K}_v^T \cdot \Delta \vec{u}_{N|t+\Delta t} - \left[\frac{k^w \cdot \Delta t}{\gamma^w} \cdot \alpha + \frac{k^w}{\gamma^w} \cdot (A + \frac{\gamma^w}{k^w} n\bar{V} \cdot k_s^{-1}) \right]$$
$$\cdot p^w{}_{|t+\Delta t} - \sum_{i=1}^{6} \frac{k^w \Delta t}{\gamma^w} \alpha_i p_i^w{}_{|t+\Delta t} = -\frac{k^w}{\gamma^w} (A + \frac{\gamma^w}{k^w} n\bar{V} \cdot k_s^{-1}) \cdot p^w{}_{|t} \tag{84}$$

By defining the following equations

$$\bar{\alpha} = \frac{k^w \cdot \Delta t}{\gamma^w} \alpha \tag{85}$$

$$\bar{A} = \frac{k^w}{\gamma^w} \cdot A \tag{86}$$

$$F_{sr} = n\bar{V} k_s^{-1} \tag{87}$$

$$\bar{\alpha}_i = \frac{k^w \Delta t}{\gamma^w} \alpha_i \tag{88}$$

Finally, the continuity equation discretized in space and time can be obtained.

$$S_{r|t} \vec{K}_v^T \cdot \Delta \vec{u}_{N|t+\Delta t} - \left[\bar{\alpha} + \bar{A} + F_{sr} \right] \cdot p^w{}_{|t+\Delta t} - \sum_{i=1}^{6} \bar{\alpha}_i p_i^w{}_{|t+\Delta t}$$
$$= -(\bar{A} + F_{sr}) \cdot p^w{}_{|t} \tag{89}$$

Combining Equation(77) and Equation(89), the FEM-FDM equation used in the program for static analysis can be obtained

$$\begin{bmatrix} [K] & \vec{F}_{Sat} \\ S_{r|t}\vec{K}_v^T & -(\overline{\alpha}+\overline{A}+F_{sr}) \end{bmatrix} \begin{Bmatrix} \Delta\vec{u}_{N|t+\Delta t} \\ p^w_{dE|t+\Delta t} \end{Bmatrix} + \begin{Bmatrix} 0 \\ \sum_{i=1}^{m} \overline{\alpha}_i p^w_{idE|t+\Delta t} \end{Bmatrix}$$
$$= \begin{Bmatrix} \Delta\vec{F}_{|t+\Delta t} + \vec{F}_{Sat} \cdot p^w_{dE|t} \\ -(\overline{A}+F_{sr}) \cdot p^w_{dE|t} \end{Bmatrix} \quad (90)$$

3.3 Verification of the program by one element analysis

Before simulating the model test of unsaturated slope failure by the proposed program, a simulation of one element is firstly carried out with two different loading conditions to verify the availability of the proposed program. The boundary conditions and loading conditions are shown in Figure 1. In Case 1, the element was firstly loaded to 0.4MPa under constant suction (0.784MPa) and then water injection (suction force decreased from -0.784MPa to -0.392MPa) was carried out under the condition that the vertical total stress was kept constant (0.4MPa). In Case 2, a given displacement of 0.005m along vertical direction was firstly loaded under constant suction (0.784MPa) and then water injection (suction force decreased from 0.784MPa to 0.392MPa) was carried out under the condition that the displacement loading is continued up to 0.01m.

The moisture characteristics curve (MCC) is shown in Figure 2. Tables 1 and 2 show the parameters involved in the constitutive model and the corresponding MCC (Zhang, 2011). Figure 3 shows the mechanical behaviors of unsaturated soil under aforementioned two loading condition. From the results, it is known that the collapse behavior of unsaturated soil observed in the elementary test due to water injection (the decrease of suction) can be reproduced during the shear process, no matter what kind of loading condition it may be.

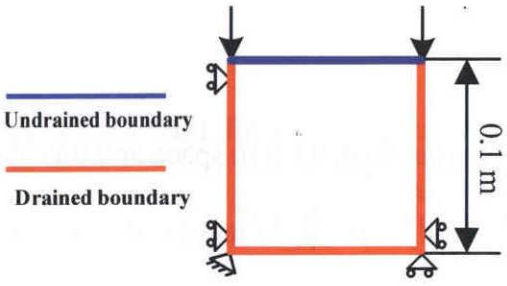

Figure 1 Boundary conditions of element simulation

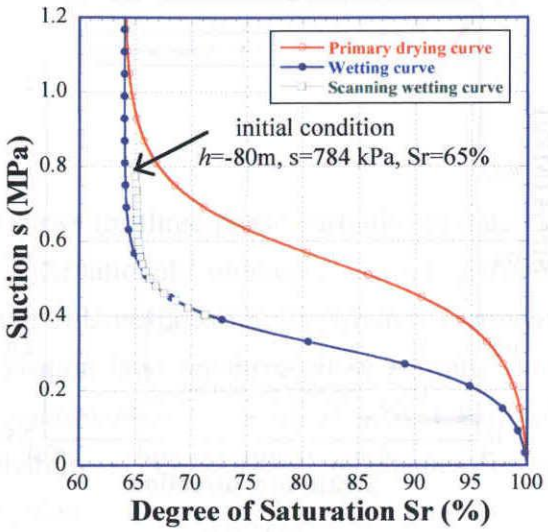

Figure 2 Simulated MCC for silt clay

Table 1 Material parameters of unsaturated silt clay

Compression index λ	0.050
Swelling index κ	0.010
Critical state parameter **M**	1.0
Void ratio N (p'=98 kPa on *N.C.L.*)	1.14
Poisson's ratio ν	0.30
Parameter of overconsolidation a	5.00
Parameter of suction b	5.50
Parameter of overconsolidation β	1.0
Void ratio N_r (p'=98 kPa on *N.C.L.S.*)	1.38

Table 2 Parameters involved in MCC

Saturated degrees of saturation S_r^s	1.00
Residual degrees of saturation S_r^r	0.65
Parameter corresponding to drying AEV (kPa) S_d	550
Parameter corresponding to wetting AEV (kPa) S_w	320
Initial stiffness of scanning curve (kPa) k_{sp}^e	200000
Parameter of shape function c_1	0.008
Parameter of shape function c_2	0.013
Parameter of shape function c_3	10.0

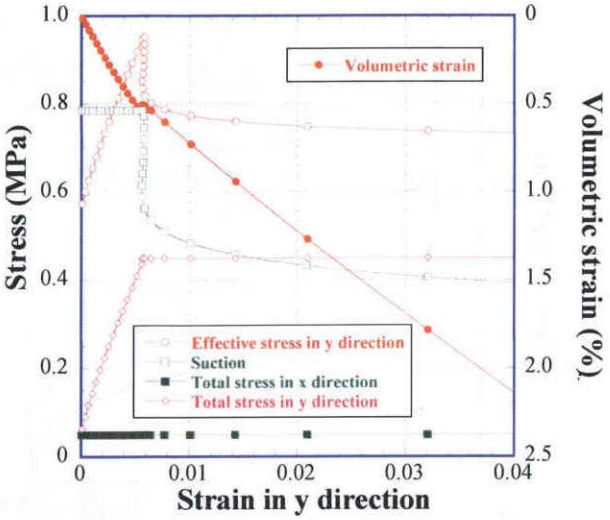

(a) Case 1

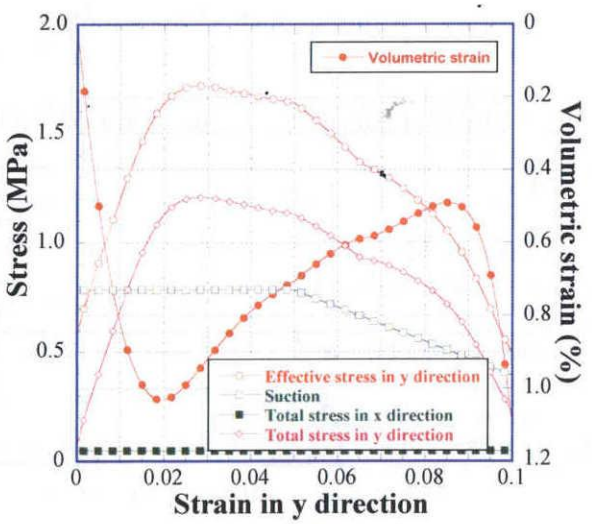

(b) Case 2

Figure 3 Mechanical behavior of unsaturated soil under two different loading conditions (σ_{30}=50kPa)

3.4 Summery

In this chapter, the governing equations of Uzuoka's three-phase field theory was re-derived. The displacement of solid u and pore water pressure p^w are taken as the basic variables in the governing equations, in which both FEM and FDM are used to discretize the equations in space. Moreover, Newmark-β method is employed to discretize the field equations in time. At last the proposed numerical method was verified by the simulation of an element subjected to different loading and water

infiltration.

References

Borja, R.I. Conservation laws for three-phase partially saturated granular media (2003), Proceedings of the International Conference, from Experimental Evidence towards Numerical Modelling of Unsaturated Soils, Weimar, Germany, 18–19 September.

Borja R. (2005): Conservation laws for three-phase partially saturated granular media, *Unsaturated soils: numerical and theoretical approaches*, Vol. 94, 3-14.

Fredlund, D.G. and Rahardjo, H. (1993): Soil mechanics for unsaturated soils, John Wilely & Sons Ltd., New York.

Fredlund, D.G. (2006): Unsaturated soil mechanics in engineer practice, ASCE, Journal of Geotechnical and Geoenvironmental Engineering, 286-321.

Kato, R., Oka, F., Kimato, S., Kodaka, T. and Sunami, S. (2009) : A method of seepage-deformation coupled analysis of unsaturated ground and its application to river embankment, J-STAGE C, Vol.65, No.1, 226-240.

Li, C., Borja, R.I. and Regueiro, R.A. (2004): Dynamics of porous media at finite strain, Computer Methods in Applied Mechanics and Engineering, 193, 3837-3870.

Oka F, Yashima A, Shimata T et al. (1994): FEM-FDM coupled liquefaction analysis of a porous soils using an elasto-plastic model, Applied Scientific Research, Vol. 52, 209-245.

Uzuoka et al. (2007): Finite element analysis for dynamic finite deformation in unsaturated soil, Proceedings of the conference on computational engineering and science,Vol.12, No.2, 523-526 (In Japanese)

Uzuoka et al. (2008): Finite element analysis of coupled of unsaturated soil and water using aerial elements, Proceedings of the conference on computational engineering and science, Vol.13, No.1, 219-222 (In Japanese)

Uzuoka et al. (2009): Soil-water-air coupled dynamic analysis of unsaturated fill, Proceedings of the conference on computational engineering and science, Vol.14, No.1, 461-464 (In Japanese)

Uzuoka, R. (2010: effective stress analysis (limited displacement analysis) seminar document (private material).

Tan, T.S., Phoon, K.K. and Chong, P.C. (2004): Numerical study of finite element method based solutions for propagation of wetting fronts in unsaturated soil, Journal of Geotechnical and Geoenvironmental Engineering, Vol.130, No.3, 254-263.

Zhang. F. and Ikariya. T. (2011): A new model for unsaturated soil using skeleton and degree of saturation as state variables, Soil and Foundations, Vol. 51, No. 1, 67-81.

Zienkiewicz, O.C., Chan, A.H.C., Pastor, M., Schre er, B.A. and Shiomi, T. (1999): Computational Geomechanics with Special Reference to Earthquake Engineering, John Wiley & Sons Ltd., New York.

CHAPTER 4 Numerical simulations of unsaturated Shirasu slope failure and comparison with soil tank model test results

4.1 Introduction

Shirasu is a kind of non-cemented pyroclastic flow deposits from active volcanoes in Kagoshima prefecture which located in the southern part of Kyushu Island, Japan. As the Shirasu particle is porous with a smaller density than common sandy soils, the slope failure easily occurs on Shirasu slopes under heavy rainfall. As it is known that the slope failure due to rainfall is mainly caused by the increase in weight of soil mass and the decrease in suction of unsaturated soil, field measurements, model tests and numerical simulations have been carried out by many researchers (Delage, 2002; Orense et al. 2004; Sako et al., 2006; Kitamura et al., 2007; Kohgo et al., 2011) to investigate the mechanism of the slope failure due to rainfall.

In the work by Kitamura et al. (2007), several patterns of the model tests were conducted on different conditions such as position of water injection, rain intensity, inclined degree of slope, etc. In this chapter, numerical simulations of the model slope failure using FE-FD program SOFT based on the proposed constitutive model in the chapter 2 and three-phase field theory in chapter 3 are carried out in the same conditions as the model test. By the comparison between the results of test and simulation, the availability of the proposed numerical method for Boundary Value Problem of unsaturated soil can be confirmed.

4.2 Model test condition and material parameters

4.2.1 Equipment and measuring devices

Shirasu soil is used as the material for the model slope in the test. Photo 1 shows the overall view of model test condition that is composed of the completed model slope and measuring devices. Figure 1 shows arrangement of pore water sensors at the bottom of the model slope to measure pore water pressure. Figure 2 shows arrangement of tensiometers in the model slope to measure negative pore water pressure (suction) and water injection position. The tensiometers with a diameter of 18mm were set at the depth of 10cm, 20cm, 30cm, 40cm and 50cm respectively in the slope and water can be

injected in to the slope from top, bottom and back side as shown in Figure 2.

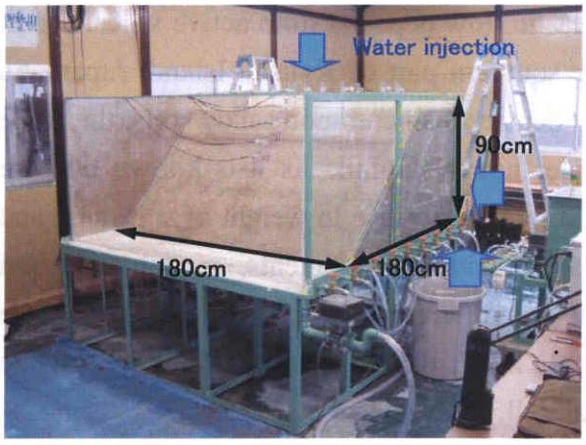

Photo 1 The whole view of test condition

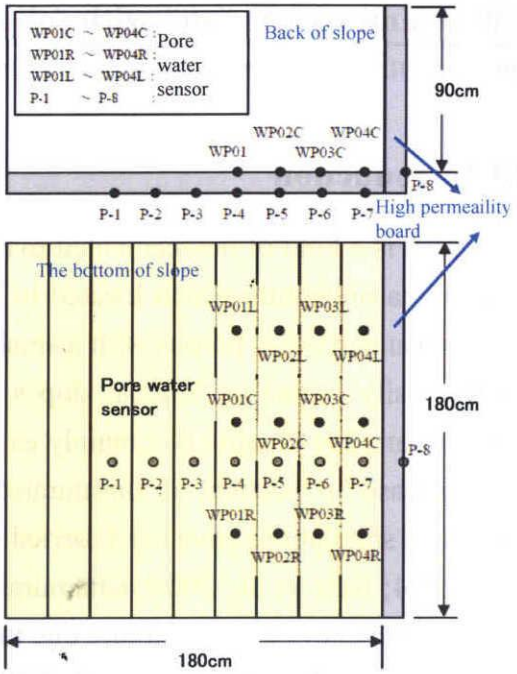

Figure 1 Arrangement of pore water sensor

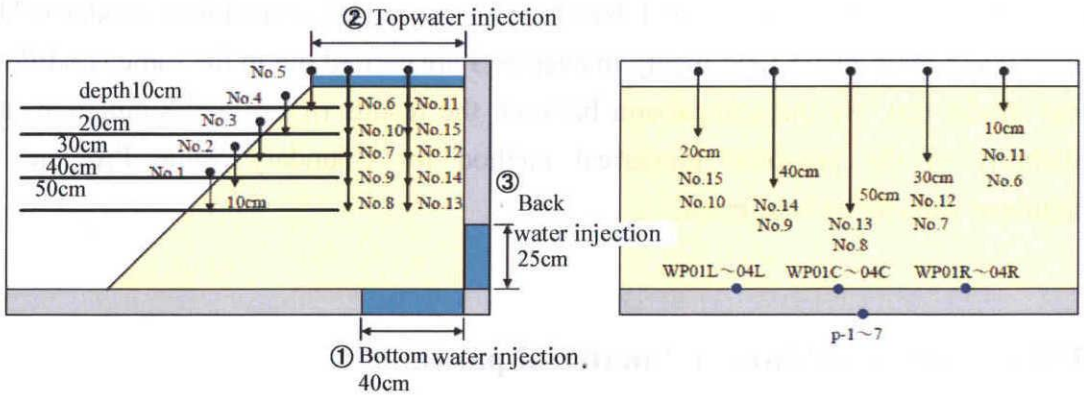

Figure 2 Arrangement of tensiometers and water injection position

4.2.2 Soil parameter and test conditions

The grain size distribution of Shirasu soil is shown in Figure 3. The soil particle density of Shirasu is 2.4g/cm^3, which is smaller than normal sandy soil. Figure 4 shows the relationship between unsaturated permeability coefficient and degree of saturation obtained from the standard constant head permeability test on Shirasu in the work by Sako et al. (2006). The physical properties of Shirasu are shown in Table 1. It is noted in

Table 1 that the degree of saturation of the specimens in the permeability test is less than 100% although the permeability coefficient obtained from the standard constant head permeability test is commonly called the saturated permeability coefficient. The moisture characteristics curve (MCC) obtained from the pressure plate method and calculation is shown in Figure 5. The simulated MCC calculated by the proposed MCC model, agrees well with the moisture characteristic observed in the tests. The parameters involved in the MCC model are shown in Table 2.

As the model slope in photo 1 was made by compacting soil layer by layer with a depth of 5cm. So the total density in Table 1 is obtained by controlling the compaction numbers. The slope angle is 45° with a height of 80cm. In the numerical analysis, two cases of the test, that are water injection from bottom at a range of 40cm and water injection from back at a range of 25cm with a fixed head of 25cm respectively, are simulated. Detailed information about model slope and drainage boundary condition in each case is shown in Table 3.

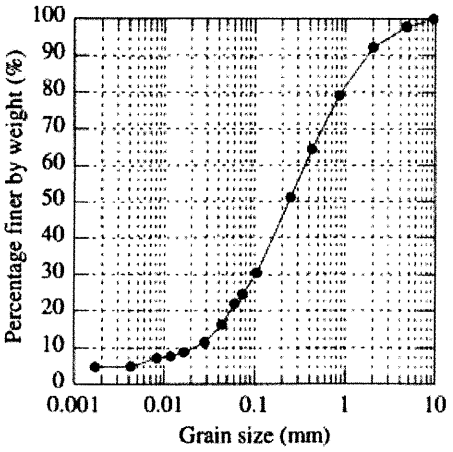

Figure 3 Grain size distribution of Shiarasu

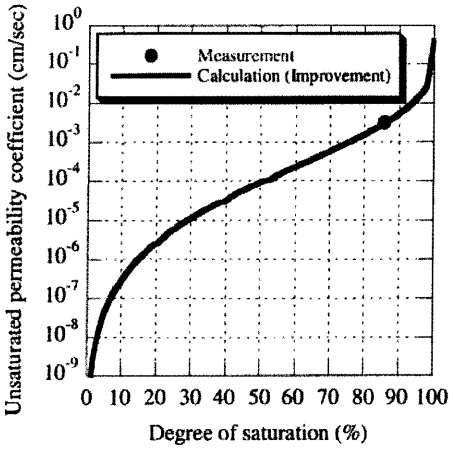

Figure 4 Relationship between permeability and degree of saturation (Sako et al., 2006)

Table 1 Physical and mechanical properties of Shirasu used in simulation

	case1	Case2
Density of soil particle (g/cm^3)	2.45	2.40
Water content in nature (%)	25.60	23.30
Void ratio	1.57	1.47
Total density of soil (g/cm^3)	1.20	1.20
Permeability of soil (cm/sec)	$5.75*10^{-3}$ (Sr=86.7%)	$1.87*10^{-3}$ (Sr=89.1%)

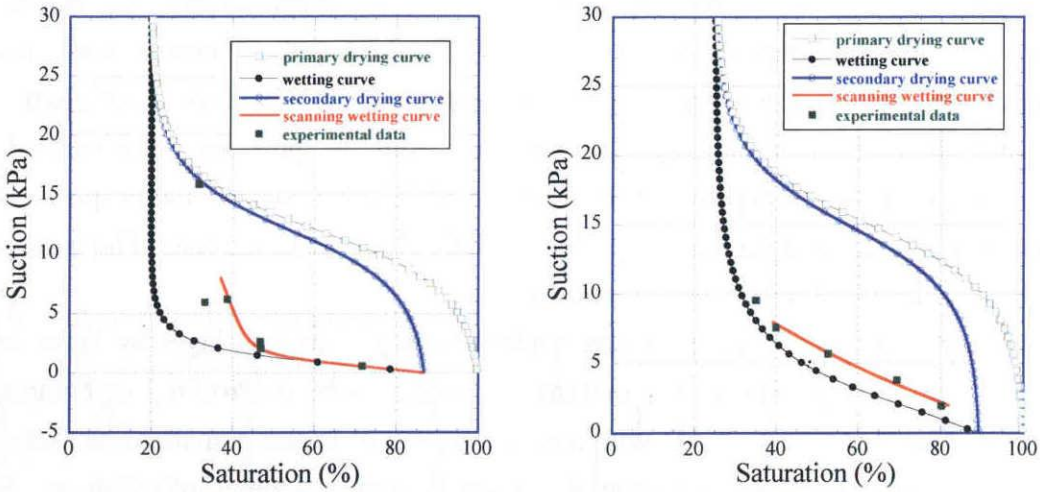

(a) Case 1 (b) Case 2

Figure 5 Moisture characteristic curves of Shirasu.

Table 2 Parameters of MCC for unsaturated Shirasu

		Case 1	Case 2
Saturated degrees of saturation S_r^s		0.867	0.891
Residual degrees of saturation S_r^r		0.20	0.25
Parameter corresponding to drying AEV (kPa)	S_d	12.00	15.00
Parameter corresponding to wetting AEV (kPa)	S_w	0.07	0.10
Initial stiffness of scanning curve (kPa) k_{sp}^e		90	20
Parameter of shape function c_1		0.30	0.30
Parameter of shape function c_2		0.60	0.20
Parameter of shape function c_3		30.0	10.0

Table 3 Two cases of test conditions used in simulation

Test condition		Case1	Case2
Shape of slope	L_1 (cm)	140	140
	L_2 (cm)	60	60
	H (cm)	80	80
	B (cm)	180	180
	α (^{o})	45	45
Total density	(g/cm^3)	1.2	1.2
Boundary condition	top	drainage	drainage
	bottom	water injection	undrainage
	back	undrainage	water injection
	slope	drainage	drainage
Water injection condition		bottom injection (fixed head:25cm)	back injection (fixed head:25cm)

4.3 Simulation of the model test

According to the size of the slope and initial water content, the initial stress state is calculated by a static analysis before simulation of the model test. The initial suction is assumed to be uniformly distributed with a value of 7.85kPa the same as the test condition. The input parameters in numerical simulation are also the same as those in the test as shown in Table 1 and Table 4. Figure 6 shows the element simulation of Shirasu under drained and exhausted conditions in saturated and unsaturated state (suction=10kPa). The parameters of unsaturated Shirasu used in element simulation are also shown in Table 4. Figure 7 shows the mesh and boundary condition in the analysis.

Table 4 Material parameters of unsaturated Shirasu

	Case 1	Case 2
Compression index λ	0.055	0.055
Swelling index κ	0.01	0.01
Critical state parameter **M**	1.0	1.0
Void ratio N (p'=98 kPa on *N.C.L.*)	**1.55**	**1.45**
Poisson's ratio ν	0.30	0.30
Parameter of overconsolidation a	2.0	2.0
Parameter of suction b	0.5	0.5
Parameter of overconsolidation β	1.0	1.0
Void ratio N_r (p'=98 kPa on *N.C.L.S.*)	**1.57**	**1.47**

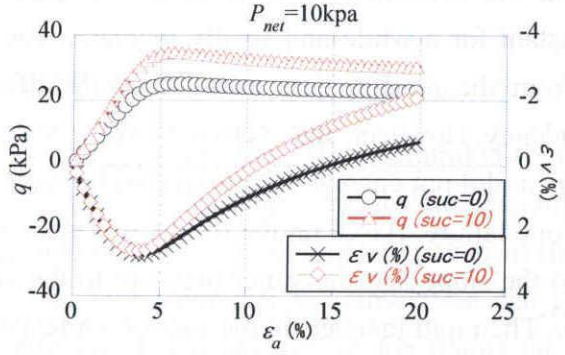

Figure 6 Element simulation of Shirasu in saturated (suction=0kPa) and unsaturated state (suction=10kPa)

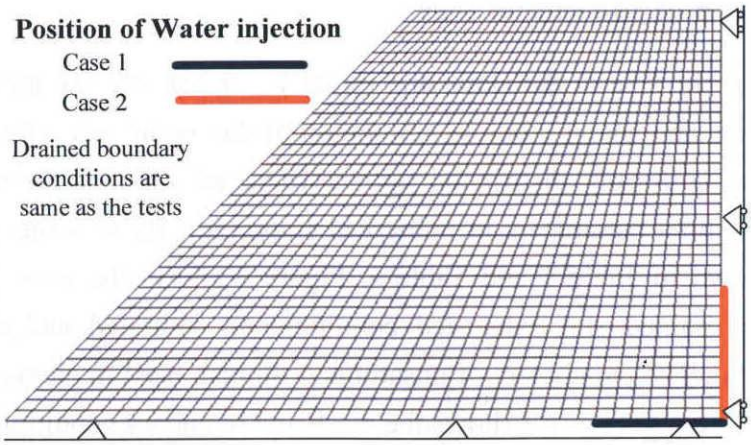

Figure 7 Analysis mesh and boundary condition (1600 elements)

4.4 Results and discussions

4.4.1 Model test results

Figure 8 shows the changes of negative pore water pressure (suction) at different depth of the slope with time respectively. From the figure, it can be seen that the suction started from about -8kpa increase from the lower part of the slope to the upper part. The suction obtained from the tensiometers installed at the depth of 50cm, increases to -3kPa, then kept constant for a while and finally increases again to reach failure. The suctions measured from the tensiometers installed at the depth of 40cm and 30cm showed the same tendency. However, the suction from the tensiometers installed at the depth of 10cm and 20cm did not change because the water had not reached the measure points before the slope failure. Based on the results it is clearly that a larger amount of water infiltrated in to the slope and the water pressure in the slope gradually becomes unstable as time goes. The rapid increase in the suction corresponds to the seepage flow passing through these measuring points. The physical meanings of the increase in suction during the initial stage and then kept a constant value of -3kPa after seepage flow passing through the measuring points should be investigated. -3kPa of pore water pressure may correspond to the air entry value of Shirasu.

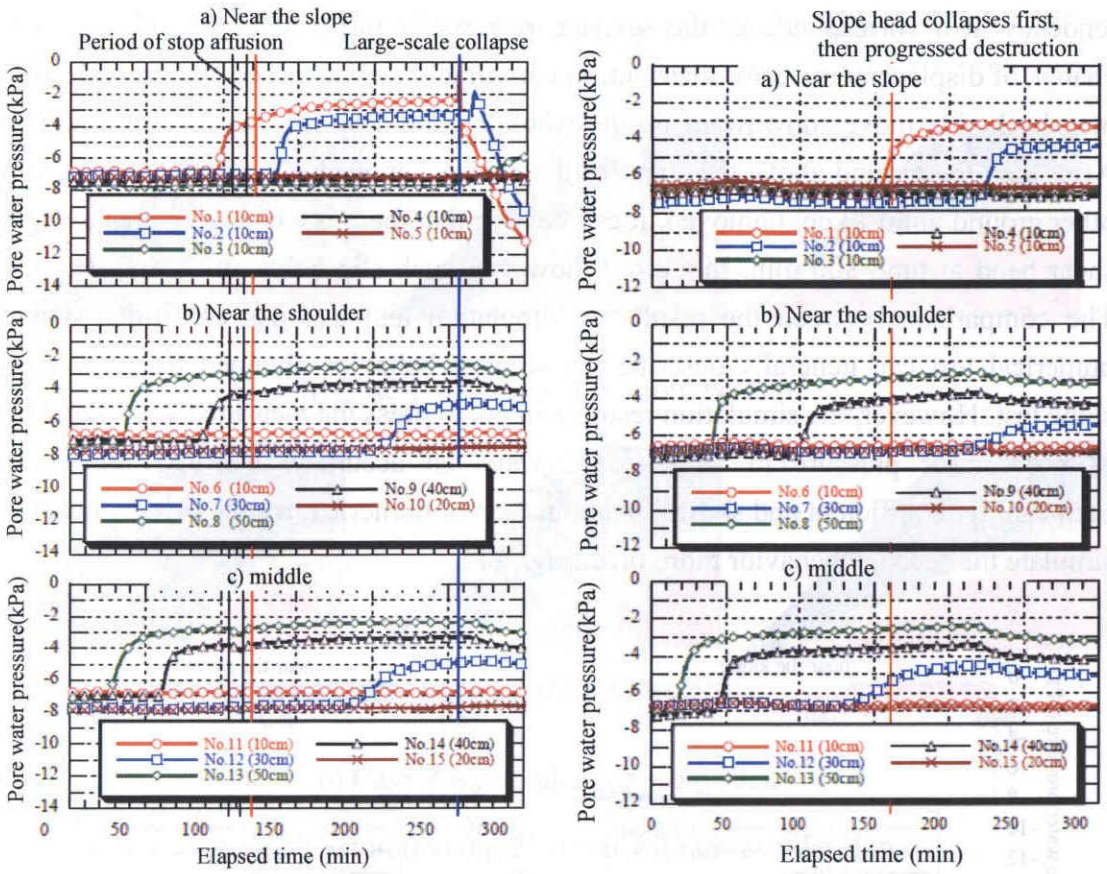

a) case-1: water injection from bottom

b) case-2: water injection from back

Figure 8 Change in negative pore water pressure with time

4.4.2 Numerical simulation results

The numerical test was carried out using 2D unsaturated-saturated FE-FD Method based on the proposed new constitutive model for unsaturated soil. Figure 9, shows the change of negative pore water pressure (suction) with time at the measured points of two cases respectively. It is found out that the simulation can generally describe the development of pore water pressure quite well in the points far away from the slope surface. In the points along the slope surface, however, a rather big difference between the calculation and the test existed. This might be caused by the assumption that the coefficients of permeability are the same in vertical and horizontal direction, and the initial suction is uniform in the whole model slope. Figure 10, Figure 11 shows the change in distribution of saturation and suction respectively. From these figures, it is known that the water is infiltrating toward slope surface from the initial position with time for both cases. 300 min after the start of water infiltration, the water had reached the toe of slope in Case 1. While in Case 2, the water had not reached the toe. This

tendency also corresponds to the seepage process in the test. Figure 12 shows the change of displacement vector distribution with time. For both cases, the ground surface near back side moves downward on the whole at first 100 min due to water seepage. After then the ground above the shear band in Case 1 moved towards the toe while the other ground almost kept unmoved. It can be seen that there is a clear slip area along the shear band at time 300 min. In Case 2, however, such slip behavior did not show up. The comparison between the results of simulation and test has confirmed that the numerical test can generally describe the seepage behavior obtained from the model slope test. However, the simulation results can not express the measured values and time of pore water pressure in an accuracy way. An accuracy of MCC, unsaturated permeability coefficient and skillful manipulation of numerical techniques are needed to simulate the seepage behavior more precisely.

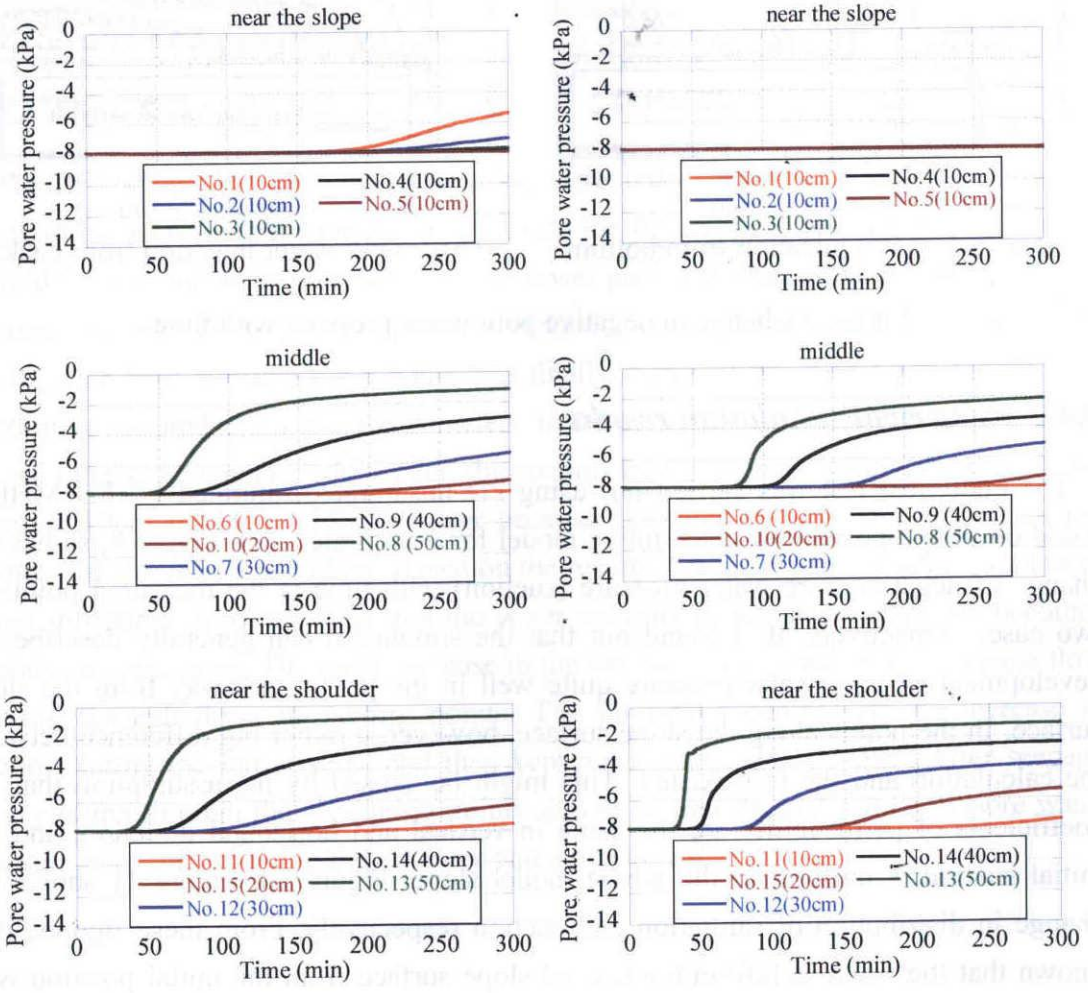

a) case-1: water injection from bottom b) case-2: water injection from back

Figure 9 Changes in pore water pressure with time

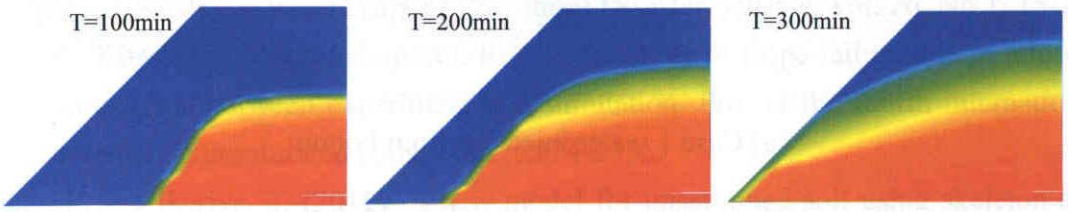

a) Case 1 water injection from bottom

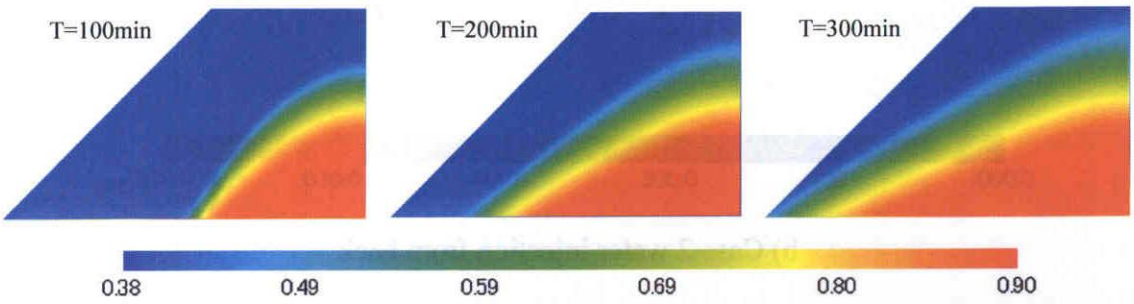

b) Case 2 water injection from back

Figure 10 Saturation distributions with time in the slope

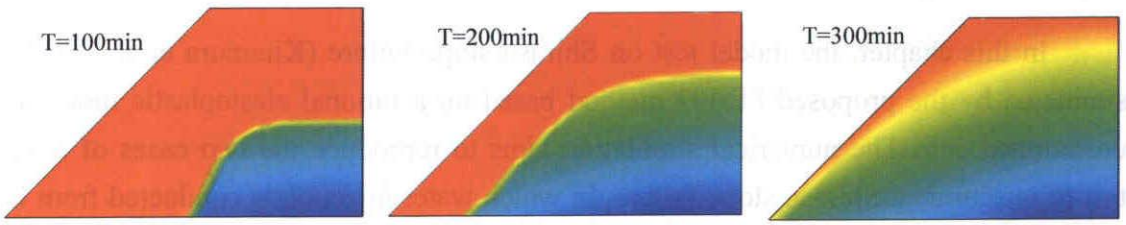

a) Case 1 water injection from bottom

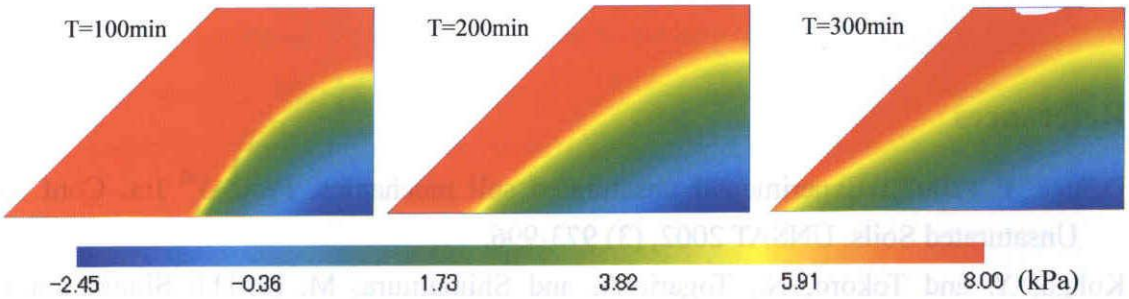

a) Case 2 water injection from back

Figure 11 Suction distributions with time

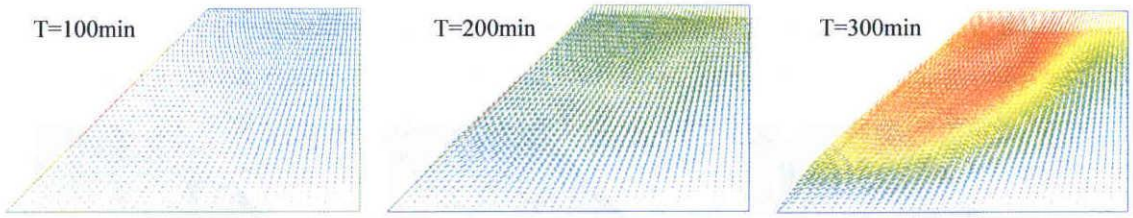

a) Case 1 water injection from bottom

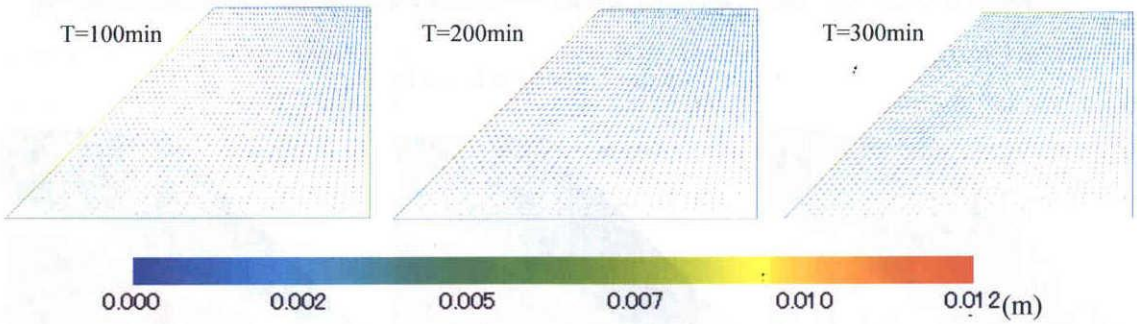

b) Case 2 water injection from back

Figure 12 Displacement vector distributions in the slope

4.5 Summery

In this chapter, the model test on Shirasu slope failure (Kitamura et al, 2007) is simulated by the proposed FE-FD method based on a rational elastoplastic model for unsaturated soil. The numerical simulation aims to reproduce the two cases of model test of unsaturated Shirasu slope failure, in which water injection is conducted from the bottom and back side of the slope respectively. Simulation results are compared with test results to verify the proposed constitutive model and numerical method.

References

Delage, P. (2002): Experimental unsaturated soil mechanics, Proc. 3rd Int. Conf. on Unsaturated Soils, UNSAT 2002, (3) 973-996.

Kohgo, Y. and Tokoro, N., Togari, A. and Shimamura, M. (2011): Simulation of behavior of a slope model with a shollow subsurface sand layer due to rainfall, Unsaturated Soils: Theory and Practice 2011, 741-746.

Kitamura, R., Sako, K., Kato, S., Mizushima, T. And Imanishi, H.(2007): Soil tank test on seepage and failure behaviors of Shirasu slope during rainfall, Japan Science and

Technology Information Aggregator, Electronic, Vol.2, No.3, 149-168 (in Japanese).
Orense, R.P., Shimoma, S., Maeda. K. And Towhata, I. (2004): Instrumented model slope failure due to water seepage, J. Natural Disaster Science, Vol. 26, No.1, 15-26.
Sako, K., Kitamara, R. and Fukagawa, R. (2006): Study of slope failure due to rainfall: A comparison between experiment and simulation, Pro. of the fourth international conference on unsaturated soils, Vol.2, 2324-2335.
Zhang. F. and Ikariya. T. (2011): A new model for unsaturated soil using skeleton and degree of saturation as state variables, Soil and Foundations, Vol. 51, No. 1, 67-81.

PART II:

NUMERICAL ANALYSIS IN SOLVING GEOTECHNICAL PROBLEMS INCLUDING LIQUEFACTION

CHAPTER 5 Numerical simulation of ground improvement for group-pile foundation and comparison with shaking table test results

5.1 Introduction

To clarify the mechanical behaviors of pile foundations at ultimate state during strong earthquakes, many researches about the tests on group-pile foundation subjected to lateral loading either in model scale or in real-scale have been conducted. Also many engineering problems related to pile foundation subjected to lateral loading have been investigated. Kimura et al (2007) reported their research work on the development and application of sheet piles with H-joint steel pile in the construction of foundations for structures. Khan et al (2008) investigated the static stability of sheet pile quay wall improved by cement treated sea-side ground with centrifuge model tests. Khan et al (2009) also conducted dynamic centrifuge tests to verify the behavior of sheet pile quay wall stabilized by sea-side ground improvement. Hara et al (2010) conducted an experimental study on the application of piled geo-wall, a composite of independent reinforced soil structure with pile foundation, as a seismic enhancement measure for embankment. More detailed remarks on the researches about pile foundation engineering can be referred to the work by Kusakabe and Kobayashi (2010).

It is known that during a strong earthquake, the dynamic behavior of a group-pile foundation is related not only to the inertial force coming from superstructures but also to the deformation of surrounding ground. Therefore, in seismic evaluation of group pile foundation, it is necessary to understand the behaviors of both group-pile foundations and superstructures simultaneously during a major earthquake. Needless to say, a full-scale loading test is the most accurate way to determine the mechanical behaviors of deep foundations though it might be extremely expensive and time consuming. On the other hand, numerical simulation also plays a very important role in determining the behaviors and a large number of numerical studies have been done in this field. Ye (2007) developed a three-dimensional static and dynamic finite element analysis code named as DBLEAVES based on finite deformation scheme. In order to confirm the applicability of the proposed numerical method, a real-scale field test of 9-pile

foundation subjected to horizontal cyclic loading (Kosa et al. 1998) is simulated with a three-dimensional (3D) soil-water coupling finite element method (FEM) using the DBLEAVES. The results are quite convincing and the applicability of the DBLEAVES is firmly verified by comparing the numerical results with the field test results (Jin et al, 2010).

In this chapter, numerical tests on seismic enhancement effect of existing group-pile foundation with ground improvement are first conducted to find out the optimum pattern of ground improvement around existing pile foundation. In the numerical tests, three influential factors are considered, that is, the depth, the thickness (or height) and the width (or length) of the ground-improvement zone around the pile group. The numerical tests are conducted in static push-over condition. The main purpose of the research is firstly to find out an optimum pattern for the partial-ground improvement around an existing pile foundation, and secondary to confirm the efficiency of seismic enhancement by the partial-ground improvement method both by shaking table tests (conducted by Morikawa and Nakamura, 2011) and numerical analyses. As a consequence, the applicability of the DBLEAVES for evaluating the seismic behavior of pile foundation is verified again. In the numerical analyses, nonlinear behaviors of ground and pile are described by cyclic mobility model (Zhang et al, 2007) and axial force dependent model (AFD model) proposed by Zhang and Kimura (2002), respectively.

5.2 Numerical tests on reinforcement effect of ground improvement around existing pile foundation

5.2.1 Introduction and analysis mesh

Cement-treated ground improvement around an existing group-pile foundation, as showed in Figure 1, is an applicable way to increase the seismic resistance of pile foundation because it has some distinct advantages such as less cost, time saving and less space necessary for construction. Some researchers and the applications of this method can be found in the works by Maeda et al (2008) and Adachi (2009). The problem, however, is how to find out an optimum pattern which depends on the size and

the position of the improved ground zone. In this section, numerical tests on a group-pile foundation are conducted using the DBLEAVES (Ye, 2007). Calculations are conducted in static loading condition. Based on the numerical tests results, the optimum size and position of the ground improvement zone are determined with the static analyses by judging the validity of the ground improvement in different conditions.

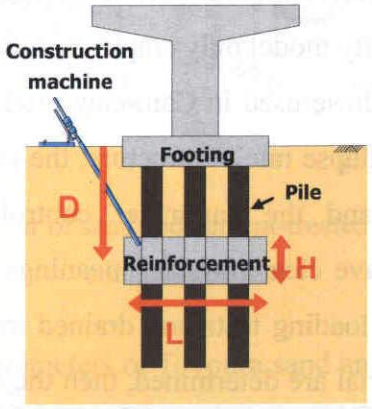

Figure 1 Cement-treated partial ground improvement methods for existing group-pile foundation

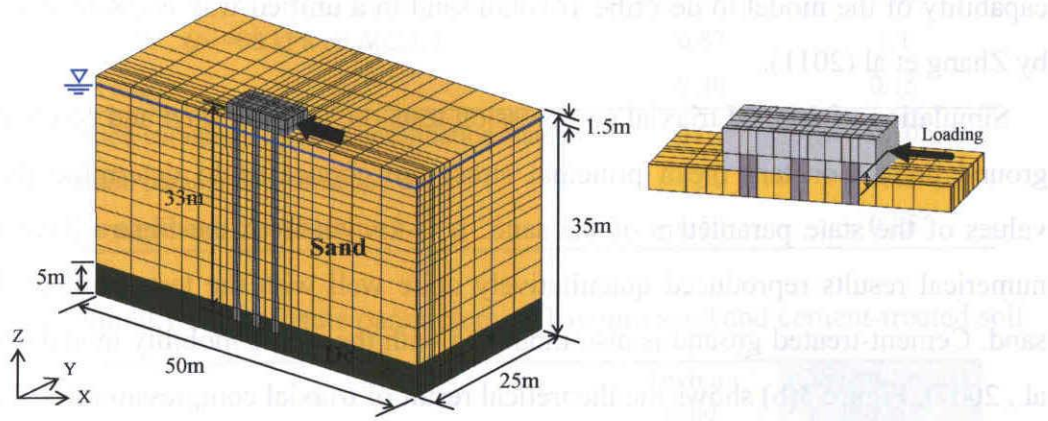

Figure 2 3D-FEM mesh for static analysis in numerical test

Figure 2 shows the geologic profile of ground and 3D-FEM mesh used in the numerical tests. The ground is composed of two layers, Toyoura sand layer at upper part and diluvial clay (DC) layer at bottom as supporting layer of the pile foundation. Because of the symmetric conditions of geometry and loading, only half of the domain is taken under consideration. The boundary conditions of the ground are fixed at the

bottom, sliding at the two side planes. The water table is located at the level of 1.5 m below the ground surface. The initial stress of the ground is gravitational field without considering the effect of pile driving.

5.2.2 Models and material parameters used for soils and piles

In the calculation, the soils are described by the cyclic mobility model (Zhang et al., 2007) and the material parameters and initial condition of the ground are listed in Tables 1 & 2. As to the cyclic mobility model only employs eight parameters among which five parameters are the same as those used in Cam-clay model. Other three parameters, the parameter controlling the collapse rate of structure, the parameter controlling the losing rate of overconsolidation and the parameter controlling the developing rate of stress-induced anisotropy, have clear physical meanings and can be easily determined by undrained triaxial cyclic loading tests and drained triaxial compression tests. Once the parameters of a geomaterial are determined, then they are fixed to uniquely describe the overall mechanical behaviors of the geomaterial, without changing the values of the eight parameters irrespective of what kind of the loading and the drainage conditions may be. That is, monotonic or cyclic loading and drained or undrained condition. The capability of the model to describe Toyoura sand in a unified way is discussed in detail by Zhang et al (2011).

Simulation of drained triaxial compression tests on Toyoura sand and cement-treated ground under constant mean principal stress are conducted to determine the initial values of the state parameters of the sand. It is known from the Figure 3 (a) that the numerical results reproduced quantitatively quite well with the test result of Toyoura sand. Cement-treated ground is also modelled with the cyclic mobility model (Zhang et al., 2007). Figure 3(b) shows the theoretical result of triaxial compression test. The peak strength of the cement-treated soil is adjusted to 1.0MPa, a typical value that can be obtained in practical engineering. The material parameters of the cement-treated ground are also listed in Tables 1 & 2.

The steel piles are set in a 3×3 pattern with 3m center-to-center pile spacing. The pile is modelled by a hybrid element proposed by Zhang et al. (2000), composed of a beam element and 4 solid elements. The nonlinear behaviour of steel pile is described by AFD model (Zhang and Kimura, 2002) and the parameters of the pile are listed in Table 3.

The concrete footing above the ground is modelled with an elastic material, so does the bearing layer (DC layer).

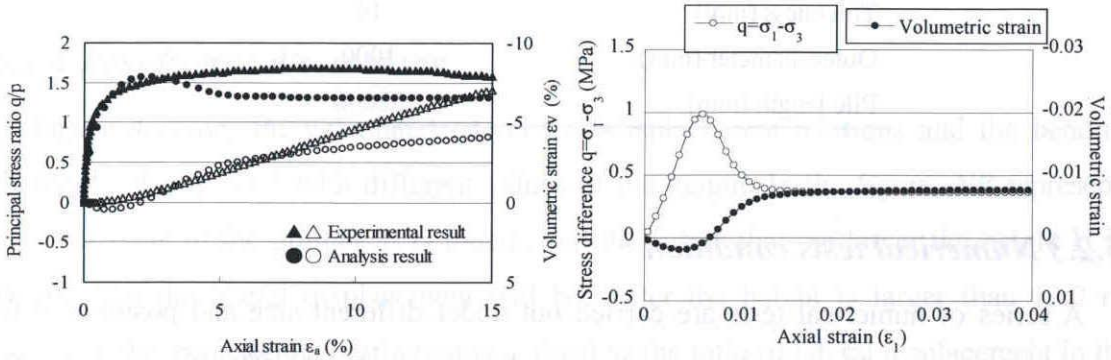

(a) Toyoura sand (b) Cement-treated soil

Figure 3 Elemental behaviour of sand and cement-treated soil under drained triaxial compression test

Table 1 Material parameters of Toyoura sand and cement-treated soil

	Toyoura sand	Cement-treated ground
Compression index λ	0.050	0.010
Swelling index κ	0.0064	0.0030
Critical state parameter M	1.30	1.66
Void ratio N (p'=98 kPa on *N.C.L.*)	0.87	1.1
Poisson's ratio ν	0.30	0.15
Degradation parameter of overconsolidation state m	0.01	0.10
Degradation parameter of structure a	0.50	0.05
Evolution parameter of anisotropy b_r	1.50	0.25

Table 2 Initial values of state parameters of Toyoura sand and cement-treated soil

	Toyoura sand	Cement-treated ground
Initial void ratio e_0	0.69	0.74
Initial mean effective stress p'(kPa)	196.0	98.0
Initial degree of structure R_0^*	0.99	0.50
Initial degree of overconsolidation OCR ($1/R_0$)	30.0	50.0
Initial anisotropy ζ_0	0.0	0.0

Table 3 Parameters of steel pile

Material (Steel pipe)	SKK 490
Thickness (mm)	14
Outer diameter (mm)	1000
Pile length (mm)	32000

5.2.3 Numerical tests condition

A series of numerical tests are carried out under different size and position of the improved ground. Three influential factors, that is, the height (H) of cement-treated ground, the length (L) and the depth (D) from the ground surface to the centre of the improved area are taken into consideration. In the effective stress analysis, a monotonic lateral loading with a maximum value of 50 MN is applied at the centre of one side surface of the footing, where all the nodes on the face move in the same way, i.e. a rigid surface. Table 4 lists the parameters of the height (H), the length (L) and the depth (D) used in the numerical tests.

Table 4 Parametric study in numerical tests

Analysis case	H (m)	D (m)	L (m)
NR	0.0	0.0	0.0
H=3.0m	3.0	7.5	9.0
H=6.0m	6.0		
H=9.0m	9.0		
H=12.0m	12.0		
H=15.0m	15.0		
D=3.0m	6.0	3.0	9.0
D=4.5m		4.5	
D=6.0m		6.0	
D=7.5m		7.5	
D=9.0m		9.0	
D=10.5m		10.5	
D=12.0m		12.0	
L=7.0m	6.0	7.5	7.0
L=9.0m			9.0

L=13.5m			13.5
L=18.0m			18.0

5.2.4 Results and discussions

Figure 4 shows the calculated lateral load-displacement relations and the bending moments of pile No.5 with different values of the height. In the figure, *NR* represents non treatment of the ground. It is found from the figure that the larger the height H is, the smaller the lateral displacement will be. After the height is larger than 12.0 m, however, the improvement ratio that is defined as the ratio of lateral displacement in the case of non-cement-treatment to those of cement-treated will not increase any more. The same tendency can be found in the bending moment. The reduction of lateral displacement due to the ground improvement with different height is listed in Table 5.

Figure 5 shows the calculated lateral load-displacement relations and the bending moments of pile No.5 with different values of the depth. It is known from the figure that the best depth, where the smallest lateral displacement can be achieved, is 4.5 m. The same tendency can be found in the bending moment. The reduction of lateral displacement due to the ground improvement with different depth is listed in Table 6.

Figure 6 shows the calculated lateral load-displacement relations and the bending moments of pile No.5 with different values of the length. It is very clear from the figure that the larger the length is, the smaller the lateral displacement will be. The same tendency can be found in the bending moment. The reduction of lateral displacement due to the ground improvement with different length is listed in Table 7.

It is, however, not an applicable way to increase the length of the improvement ground without limitation because of the cost, time and workability of the ground improvement. Therefore, a reasonable length, together with a reasonable height of the improvement ground, should be decided in real engineering project based on the concept of improvement efficiency, which is defined as the ratio of improvement ratio to the total volume of the improved ground. Figure 7 shows the calculated improvement ratio and corresponding improvement efficiency based on the lateral displacement. From the improvement efficiency calculated by the numerical tests, the optimum size and the position of the ground improvement zone are determined, that is, the height (H)

is 6m, the depth (D) is from 0 m to 4.5 m and the length (L) is 9m.

It should be pointed out that the optimum geometrical layout of the ground improvement is assessed basis on the push-over model that only considers inertial force from superstructures. In reality, however, the seismic behavior of the soil-group pile foundation-superstructure system is affected by combined inertial and kinematic loading. The reason why using the push-over model to select such an optimum pattern is only for the two following factors. The first factor is that in the design of a pile foundation in practical engineering, the seismic behavior of the piles is evaluated with push-over model in most cases. The second factor is that when considering kinematic loading due to soil-foundation interaction, both the nonlinearity of soil and pile should be properly evaluated at element level to make the sense, which may make the selection very complicated and unrealistic. One the other hand, in the following chapters, the enhancement effect of the partial ground improvement method will be investigated in detail with shaking table test and dynamic analysis. Therefore the way to select the optimum pattern is relatively reasonable.

Table 5 Calculated maximum lateral displacements and bending moments (different height)

Height H (m)	Maximum lateral displacement (cm)	Maximum bending moment (MN•m)
Non-cement-treatment	122.0	6.49
3	114.0	6.55
6	97.9	6.46
9	81.2	6.31
12	66.2	5.85
15	62.4	5.63

Table 6 Calculated maximum lateral displacements and bending moments (different depth)

Depth D (m)	Maximum lateral displacement (cm)	Maximum bending moment (MN•m)
Non-cement-treatment	122.0	6.49
3	77.5	5.77

4.5	74.7	5.34
6	83.6	6.10
7.5	97.9	6.46
9	109.0	6.59
10.5	117.0	6.58
12.5	121.0	6.56

Table 7 Calculated maximum lateral displacements and bending moments (different length)

Length H (m)	Maximum lateral displacement (cm)	Maximum bending moment (MN•m)
Non-cement-treatment	122.0	6.49
7	83.2	5.74
9	74.8	5.35
13.5	45.7	4.19
18	34.8	3.89

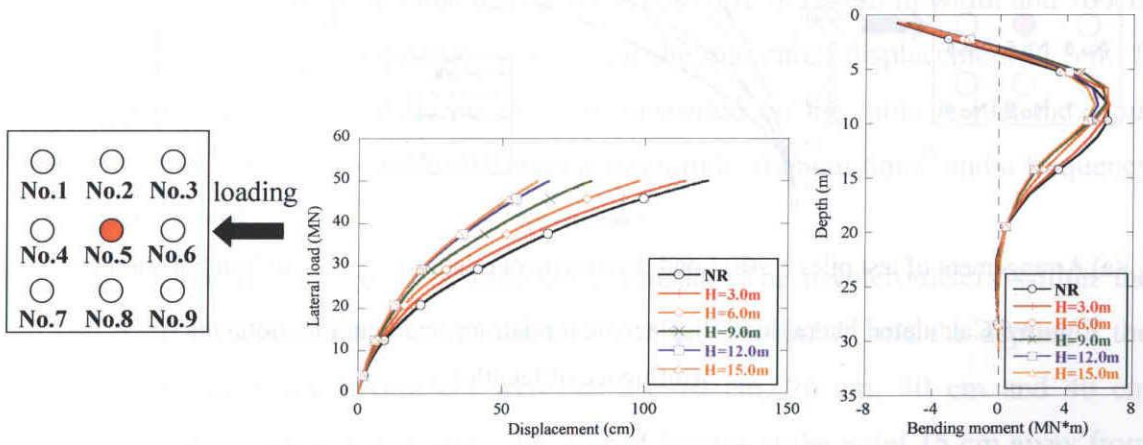

(a) Arrangement of test piles (b) Load-displacement relations (c) Bending moment

Figure 4 Calculated lateral load-displacement relations and bending moments of pile No.5 (influence of height H)

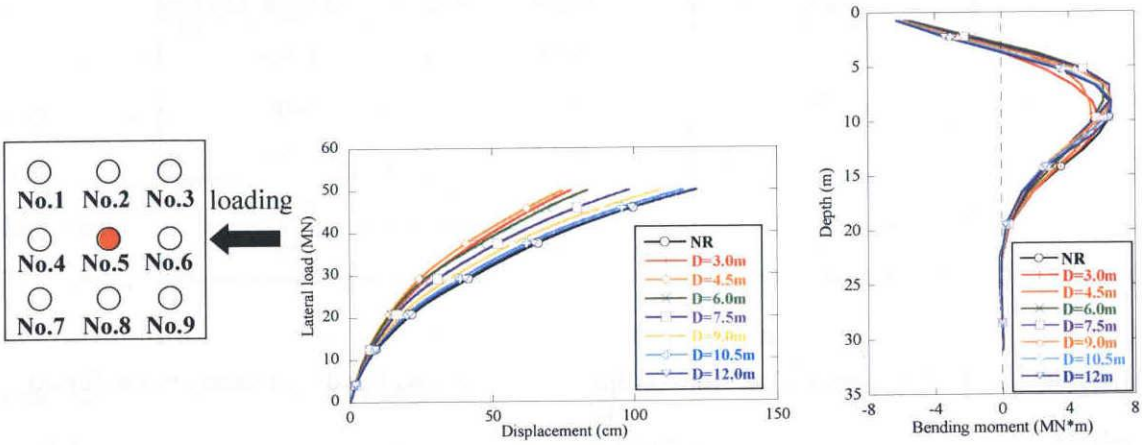

(a) Arrangement of test piles (b) Load-displacement relations (c) Bending moment

Figure 5 Calculated lateral load-displacement relations and bending moments of pile No.5 (influence of depth D)

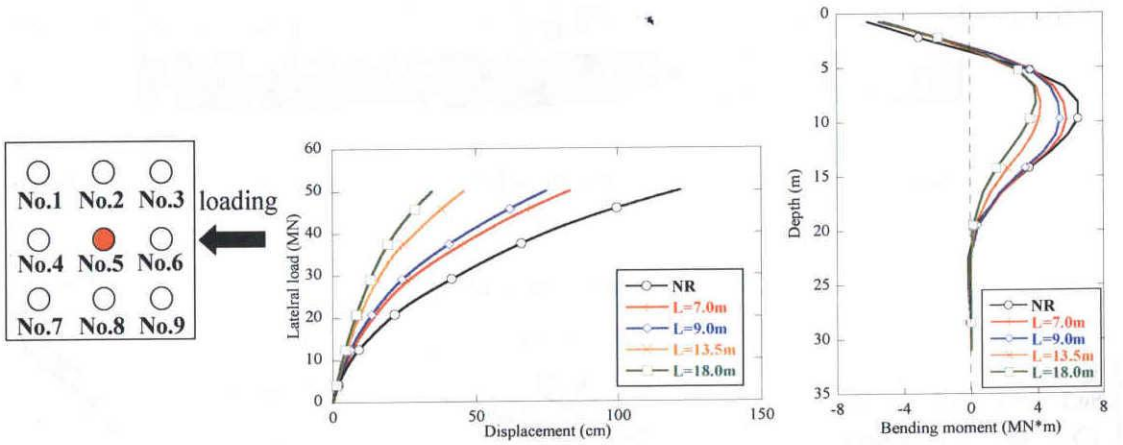

(a) Arrangement of test piles (b) Load-displacement relations (c) Bending moment

Figure 6 Calculated lateral load-displacement relations and bending moments of pile No.5 (influence of length L)

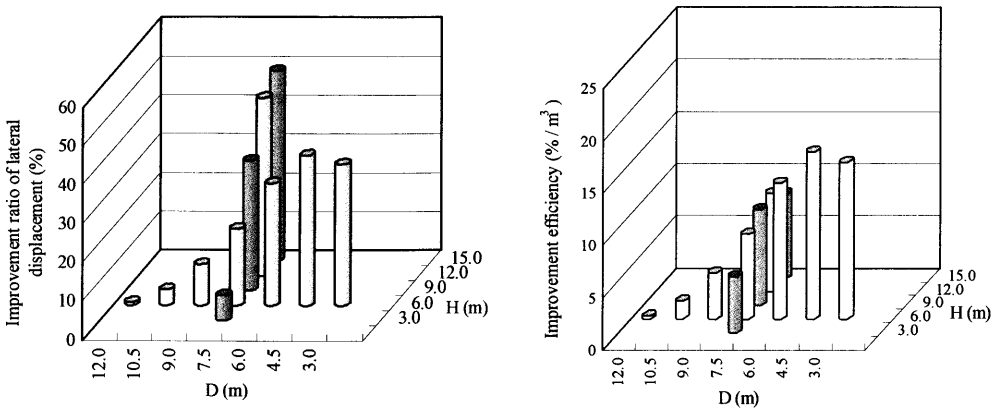

Improvement ratio of lateral displacement　　Improvement efficiency

(b) Depth and height as variables

Figure 7 Calculated improvement ratio and corresponding improvement efficiency

5.3 Numerical simulation of the shaking table tests a superstructure group pile foundation ground system with partial ground improvement

5.3.1 Brief introduction of shaking table tests

Photo 1 shows the shaking table test device whose size is 120cm in width and 160cm in length. The maximum acceleration is 1g and the maximum displacement is 5cm. It should be noticed here that the acceleration measured on the table is just the input vibration wave, a typical cosine wave with a magnitude of about 6m/s^2 and a frequency of 4Hz.

Figure 8 shows the layout of measuring sensors. The accelerometers within the ground were set along two columns marked with label *A* and *B*, and the depths of the places where these accelerometers were set are 10 cm, 20 cm, 30 cm and 40 cm respectively, as shown in the figure. Position *A* locates at the point 15 cm away from the center line while Position *B* locates at the point 15 cm away from the boundary. Accelerometers were also installed on the table, footing and the top of the pier.

In considering the reinforcement effect of the partial ground improvement method, two cases, that is, Case1 without improvement and Case2 with improvement, were tested. The pattern of the partial ground improvement is the optimized one that has been selected with the numerical tests described in previous chapter in which the soil-water

coupling static elastoplastic finite element analyses were conducted on the group-pile foundation with different patterns of partial ground improvement area.

The relative density of the model ground is Dr=79.8% with a standard deviation of σ=3.95%. The average height of the model ground is 0.496m with a standard deviation of σ=0.0038m. The Parameters of pile, pier and footing are shown in Table 8. The Parameters of improved ground material are shown in Table 9. The input waves in 1G shaking table test are shown in Figure 9.

Table 8 Parameters of pile, pier and footing

Item	Size (prototype)	Size (model)	Similarity ratio
Pile diameter (m)	1.00	0.02	50
Thickness of pile (m)	0.014	0.001	14
Pile length (m)	25.00	0.50	50
Pile spacing (m)	3.00	0.06	50
Bending stiffness of pile ($N \cdot m^2$)	1.11E+09	1.89E+02	5.87E+06
Weight of upper structure (kN)	7.38E+03	0.059	1.25E+05
Height of pier (m)	7.50	0.15	50
Width of footing (m)	9.00	0.18	50
Thickness of footing (m)	2.50	0.05	50
Elastic modulus of pile E_p (kPa)	-	7.0E+07	-
Density of pile ρ (t/m^3)	-	2.7	-

Table 9 Physical properties of improved ground material

Wet unit weight	γ_t (kN/m^3)	19.9
Water content	w (%)	21.6
Uniaxial strength	q_u (kPa)	600.
Poisson's ratio	ν	0.20
Deformation stiffness	E_{50} (MPa)	10.8

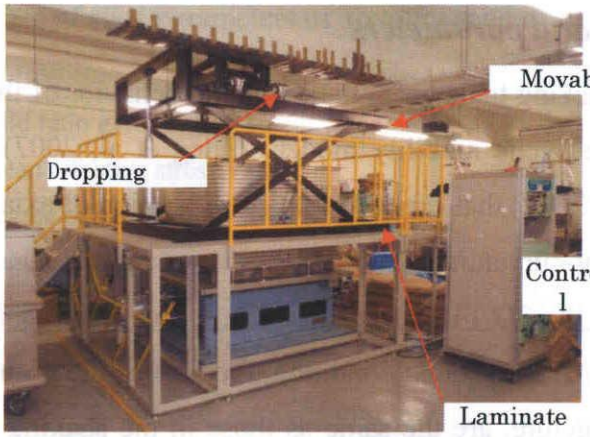

Photo 1 Shaking table test device in NIT

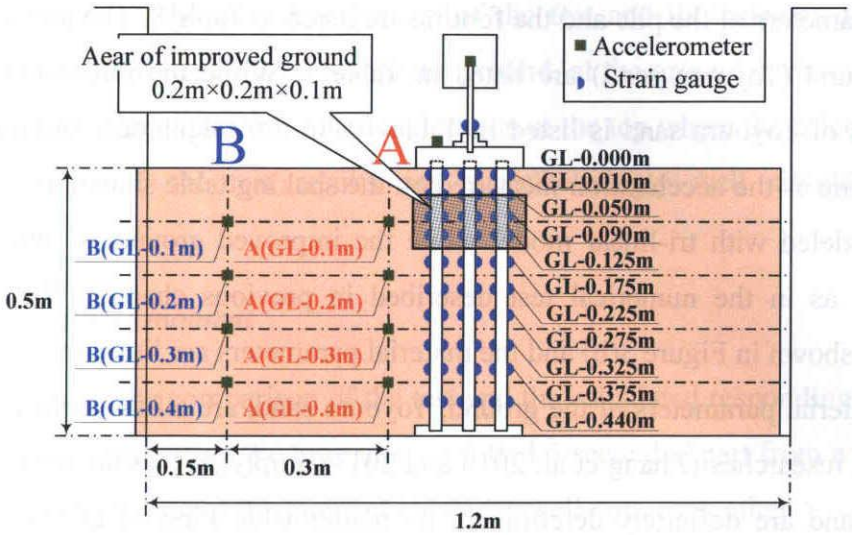

Figure 8 Layout of measuring sensors

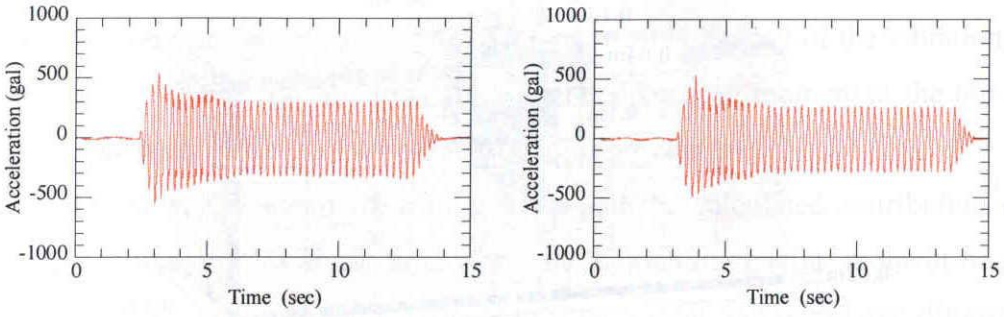

(a) Case 1 (Non-improvement) (b) Case 2 (ground improvement)

Figure 9 Input waves in 1G shaking table test

5.3.2 FEM mesh and parameters

In simulate the shaking table tests, the nonlinear behavior of the ground and the pile are described by the cyclic mobility model (Zhang et al, 2007) and the AFD model (Zhang and Kimura, 2002) that can take into consideration of axial-force dependency in the nonlinear moment-curvature relations.

Figure 10 shows the 3D FEM mesh used in the dynamic analysis for the shaking table test of Case2. All the ground condition, the size of the group-pile foundation, the footing and superstructure, are the same as those in the shaking table test. The model ground is made from Toyoura sand. Because of the symmetric geometric and loading condition, only half of the domain was considered in the calculation.

The parameters of the pile and the footing are listed in Table 8. The parameters of the model ground (Toyoura sand) are listed in Table 1. While the initial values of state parameters of Toyoura sand is listed in Table 10. In the calculation, the input wave is just the same as the acceleration measured on the shaking table shown in Figure 9. The pier is modeled with tri-linear model while the improved ground is simulated in the same way as in the numerical test described in previous chapter. The stress-strain relation is shown in Figure 3(b) and the material parameters are listed in Table 1.

The material parameters of the ground, Toyoura sand, are all the same as those used in the past researches (Zhang et al, 2010 and 2011), implying that the parameters of the Toyoura sand are definitely determined, no matter what kind of the boundary value problem may be.

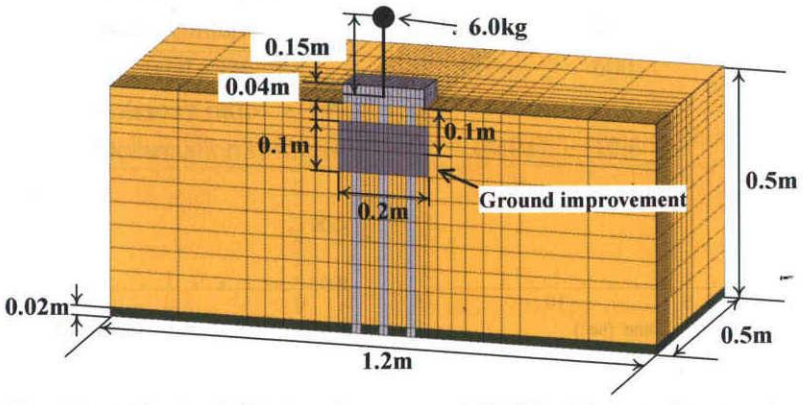

Figure 10 3D-FEM mesh used in dynamic analysis (Case2)

Table 10 Initial values of state parameters of Toyoura sand in simulating shaking table tests

Initial void ratio e_0	0.68
Initial mean effective stress p'(kPa)	100.0
Initial degree of structure R_0^*	0.99
Initial degree of overconsolidation OCR $(1/R_0)$	30.0
Initial anisotropy ζ_0	0.0

Note: Density ρ = 1.579 (t/m^3); Relative density Dr=0.80

5.3.3 Simulation results

Responding acceleration

Figures 11 and 12 show the comparison of the test and the calculated responding accelerations at different position, within the ground, at the ground surface, the footing and the top of the pier. Apart from the acceleration at the top where the calculated one is larger than the test, the test results are overwhelmingly well simulated by the calculation.

Responding bending moment

Figure 13 shows the comparison of the test and the calculated responding histories of the bending moments within the time interval 4.0~4.5 second. Apart from a small phase difference, the magnitude of the moment coincides well with each other.

Figure 14 shows the tested and calculated time histories of the bending moments at the positions of GL-0.01m, GL-0.125m and GL-0.325m. By comparing the results, it is known that the test results are well simulated on the whole, with the only difference that in the calculation, the decreasing degree of the moment at the end of the vibration is not so prominent as observed in the test. The calculated bending moment at the top of the piles is greatly reduced due to the partial ground improvement.

Figure 15 shows the comparison of the test and the calculated distribution of the moments in different piles at the time when the maximum bending moment occurred. The test results are simulated on the whole to some extent, but with large difference at the end of the pile where the test results are overestimated by the calculation, in Piles *L* and *C*. Meanwhile, the difference between different piles is much smaller than those

observed in the test. The reason of the discrepancy between the test and calculation might be caused by the fixed condition of the pile end. Because the pile end is inserted into a hole with a depth of 1cm in the test, which may gives raise to some restriction on the rotation of the end. In the simulation, however, the pile end is assumed to be rotation free. Further discussion on this issue should be down in the future study.

Figure 16 shows an enlarged part of the histories of the tested and calculated bending moments at different positions. The calculated results are similar to the test results The magnitude of the bending moments is dependent on the axial force of the pile, that is, the maximum moment always occurred in push-into pile that has relative large axial force while the minimum moment occurred in pull-out pile that has relative small axial force. Though this phenomenon in the calculation is not as prominent as observed in the test, the tendency is clearly simulated, showing the calculation is quite convincing.

It should be pointed out from the above discussion on the responding moments that the partial ground improvement really determines the expected effect at the pile head, according to the test and numerical calculation data, large bending moments at natural soil/reinforced soil interface, however arise in the same order of the magnitude of those at pile head. It means that the bending moments at natural soil/reinforced soil interface become critical for pile design under seismic loading. In practical engineering, however, it is possible to reduce the stiffness of the reinforced soil by controlling the cement injection so that a more even change of the stiffness around the interface can be expected, which may be expected to reduce the increase of the moment around the interface. Further study on this issue by shaking table tests and numerical tests should be down to clarify the factor.

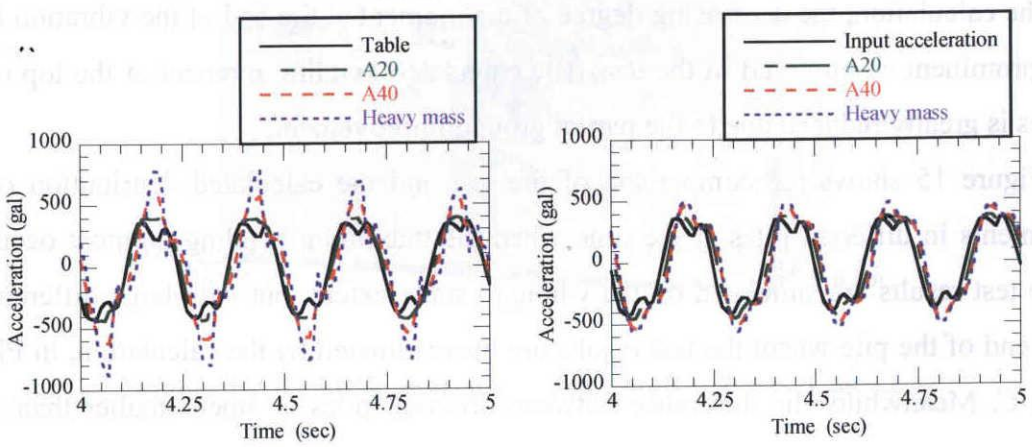

(a) Test (b) Calculation

Figure 11 Comparison of test and calculated responding accelerations (Case 1)

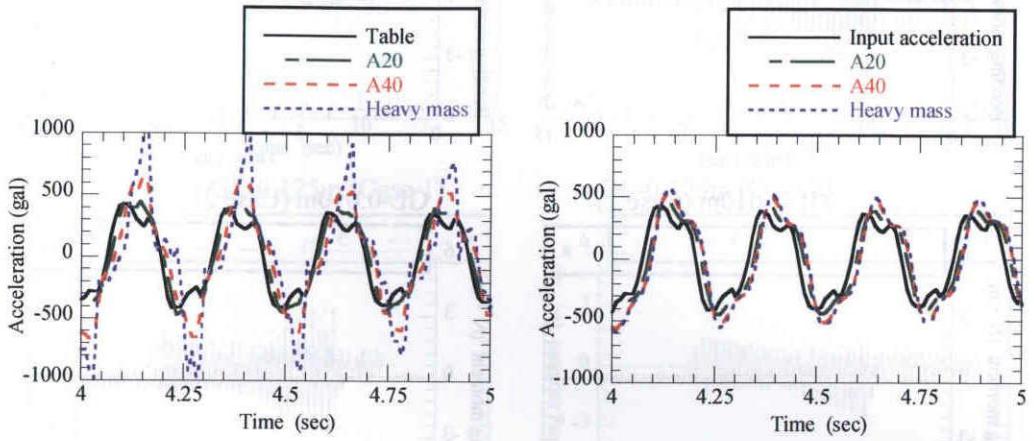

(a) Test (b) Calculation

Figure 12 Comparison of test and calculated responding accelerations (Case 2)

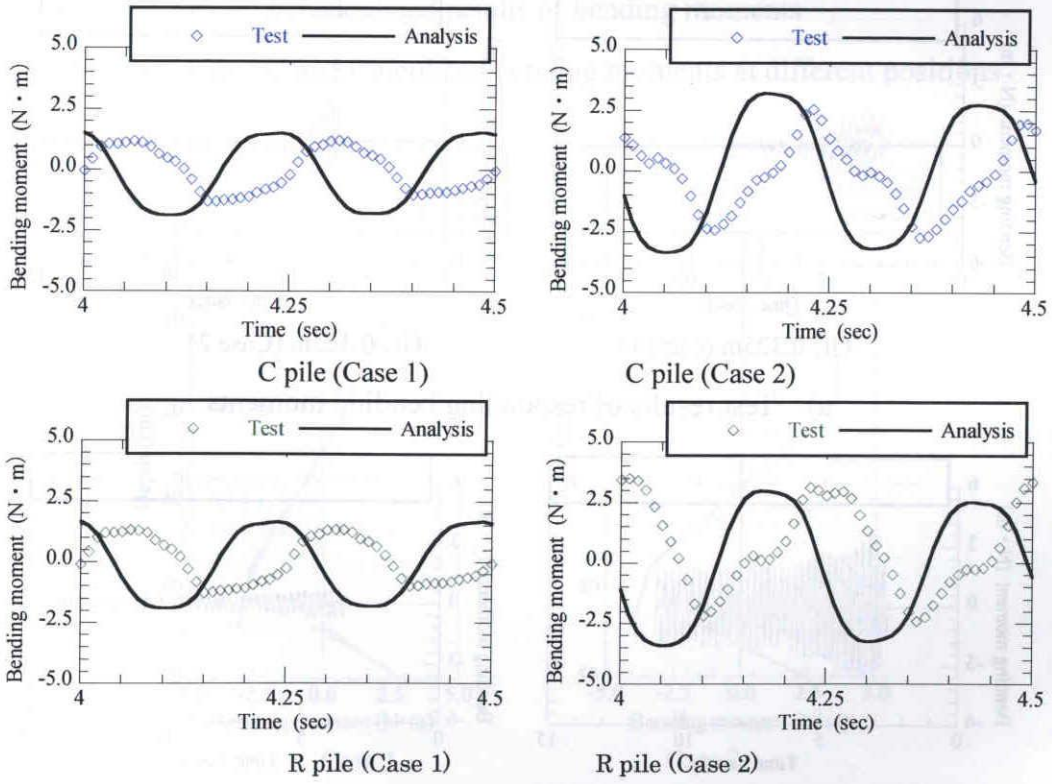

Figure 13 Comparison of test and calculated responding moments at GL-0.125m

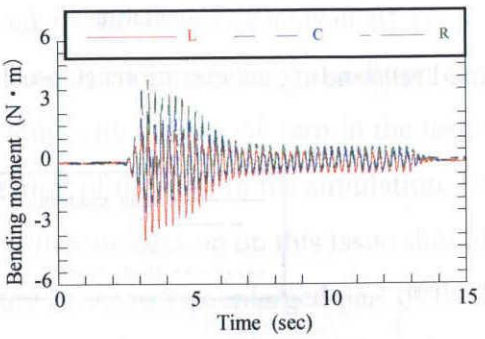

GL-0.010m (Case 1)

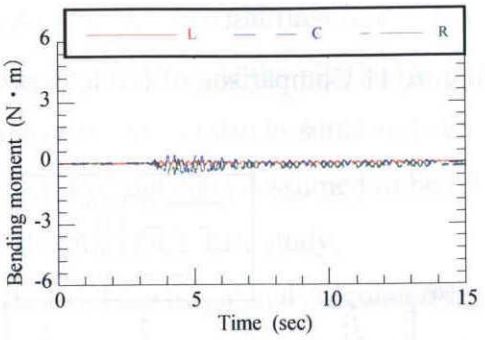

GL-0.010m (Case 2)

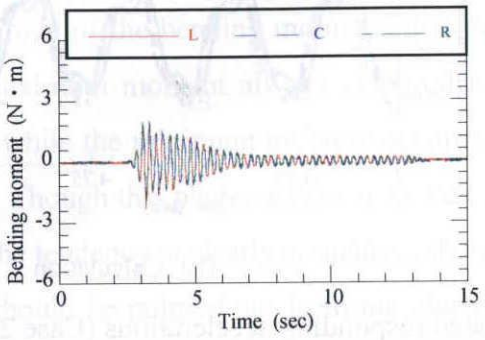

GL-0.125m (Case 1)

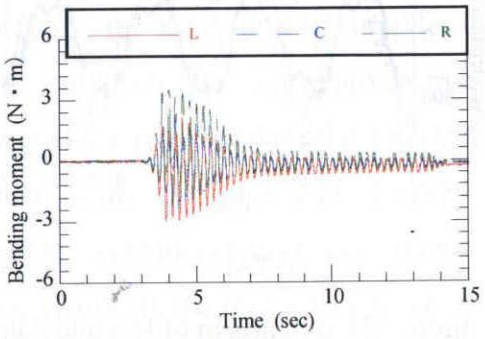

GL-0.125m (Case 2)

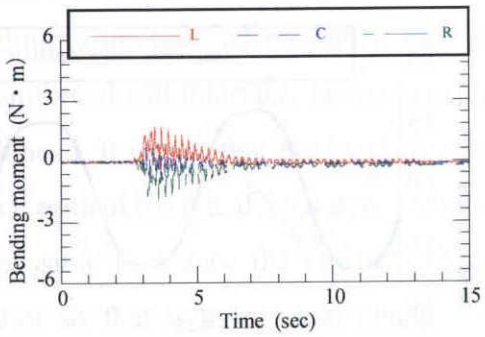

GL-0.325m (Case 1)

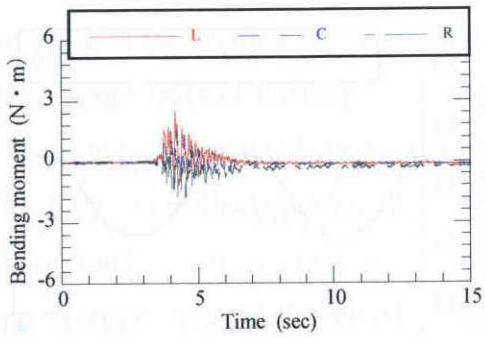

GL-0.325m (Case 2)

a) Test results of responding bending moments

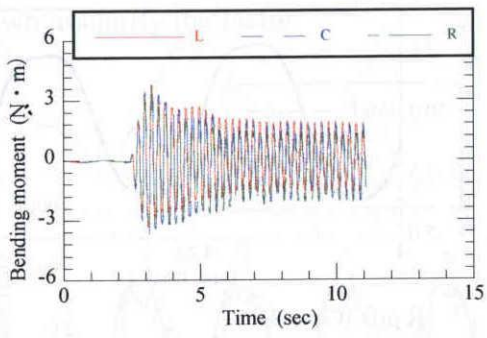

GL-0.010m (Case 1)

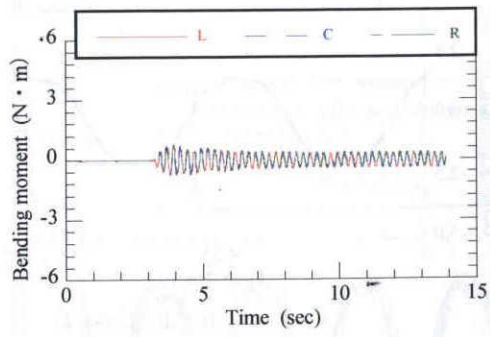

GL-0.010m (Case 2)

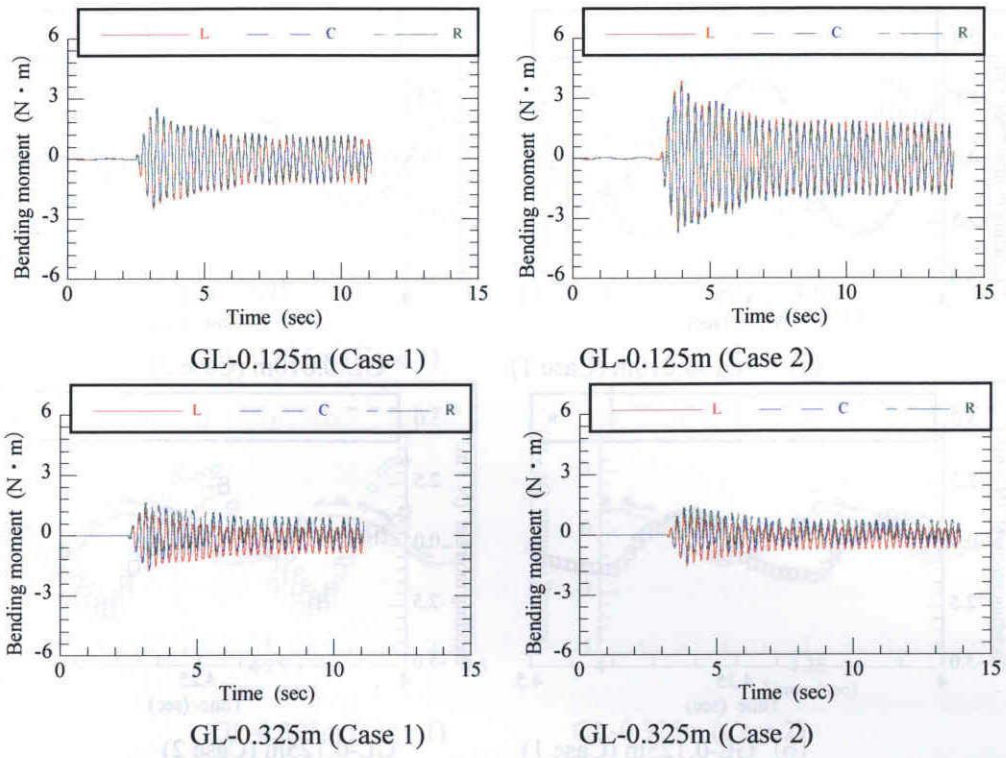

b) Calculated results of bending moments

Figure 14 Tested and Calculated bending moments at different positions

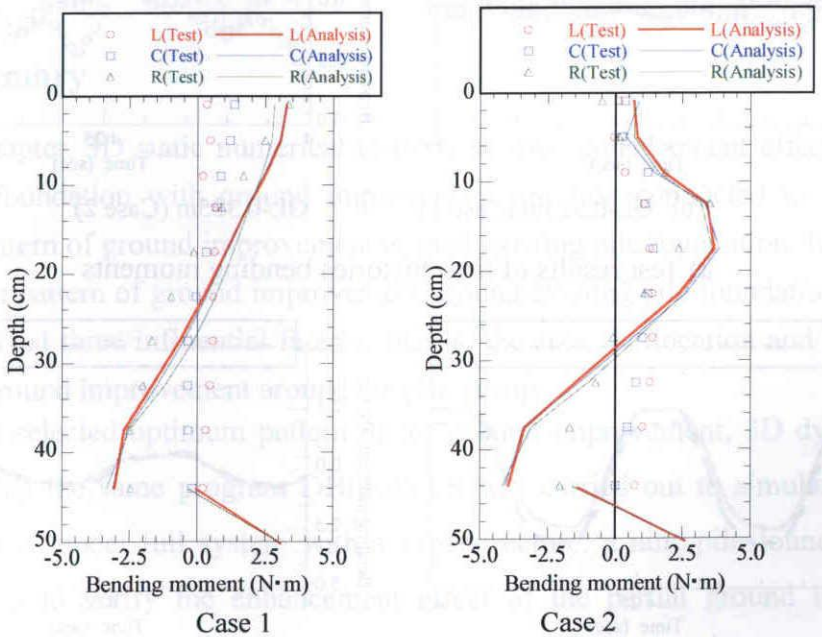

Figure 15 Comparison of test and calculated distribution of bending moments

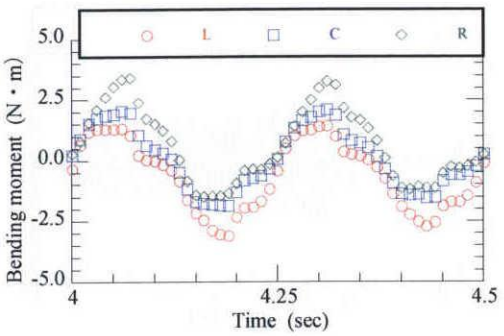

(a) GL-0.010m (Case 1)

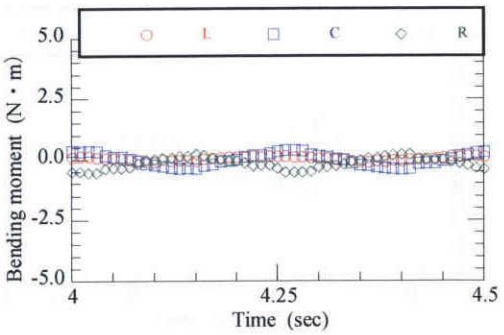

GL-0.010m (Case 2)

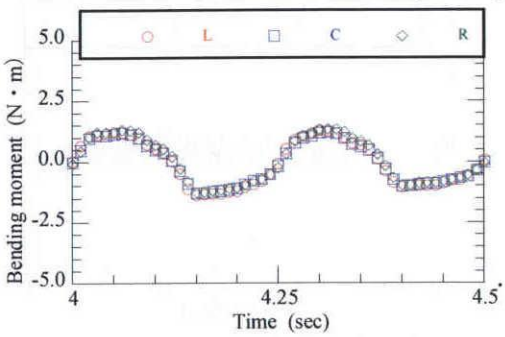

(b) GL-0.125m (Case 1)

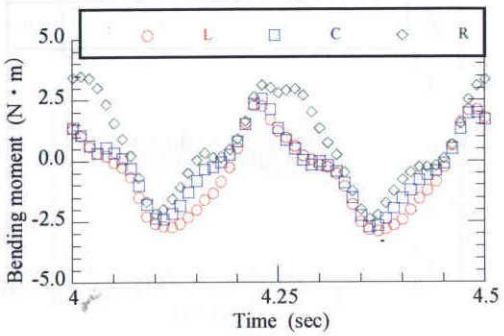

GL-0.125m (Case 2)

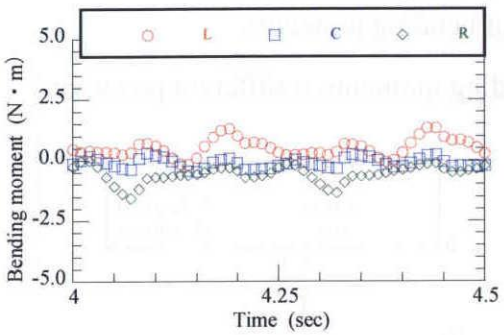

(c) GL-0.325m (Case 1)

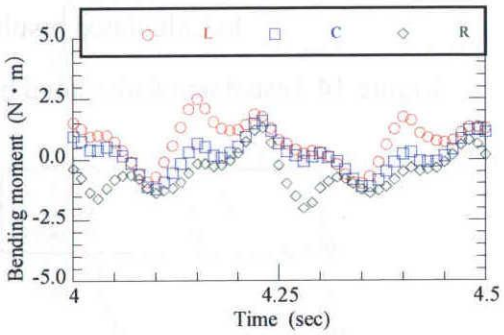

GL-0.325m (Case 2)

a) Test results of time histories bending moments

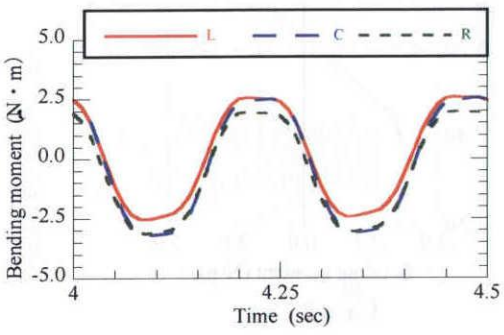

GL-0.010m (Case 1)

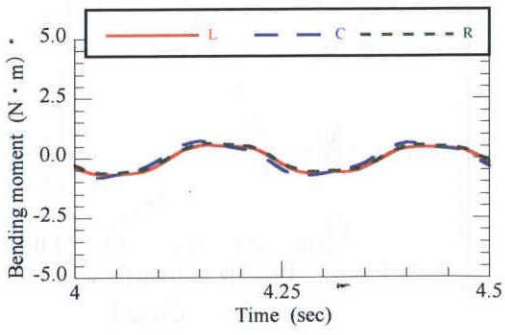

GL-0.010m (Case 2)

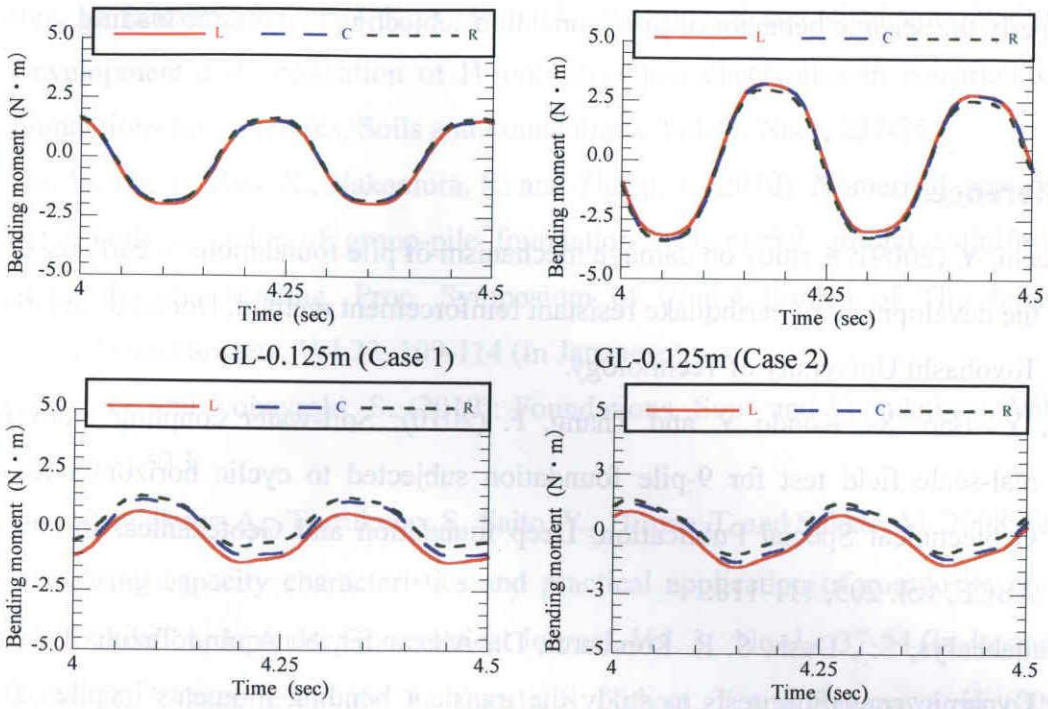

b) Calculated results of time histories bending moments

Figure 16 Calculated time histories bending moments at different positions

5.4 Summary

In this chapter, 3D static numerical tests on seismic enhancement effect of existing group-pile foundation with ground improvement are first conducted to find out the optimum pattern of ground improvement around existing pile foundation. In finding out the optimum pattern of ground improvement around existing pile foundation, numerical tests considered three influential factors, that is, the size, the location and the shape of the partial ground improvement around the pile group.

Using the selected optimum pattern of the ground improvement, 3D dynamic FEM analyses using the same program DBLEAVES was carried out to simulate a shaking table test on a model full system with a superstructure, a nine-pile foundation and a sandy ground to verify the enhancement effect of the partial ground improvement method. It was confirmed by both shaking table test and numerical simulation that the enhancement effect to reduce the bending moment within the piles can be achieved with the partial ground improvement method, especially within the improved area. The study shows that the proposed numerical method using DBLEAVES is capable to evaluate

properly the seismic behavior of pile foundation subjecting to dynamic loading.

References

Adachi, Y. (2009): A study on damage mechanism of pile foundations at earthquake and the development of earthquake resistant reinforcement method, Doctoral dissertation, Toyohashi University of Technology.

Jin, Y., Bao, X., Kondo Y. and Zhang, F. (2010): Soil-water coupling analysis of real-scale field test for 9-pile foundation subjected to cyclic horizontal loading, Geotechnical Special Publication, Deep foundation and Geotechnical in situ test, ASCE, vol. 205, 111-118.

Bhattacharys, S. , Dash, S. R. Lombardi, D., Alexander, N. A. and Tazoh, T. (2011): Dynamic centrifuge tests to study the transient bending moments in piles during liquefaction, Proceedings of 4th Japan–Greece Workshop Seismic Design of Foundations, Innovations in Seismic Design, and Protection of Cultural Heritage, Tazoh and Gazetas (eds), Vol.1, 107-121.

Hara, T., Tsuji, S., Yashima, A., Sawada, K., Tatta, N. and Otake Y. (2010): Independent reinforced soil structure with pile foundation -Piled geo-wall: An experimental study on the application to seismic measure for embankment-, Soils and Foundations, Vol.50, No.5, 565-571.

Ishizaki, S., Nagao, T. and Tokimatsu, K. (2011): Dynamic centrifuge model test of pile-supported building with semi-rigid head connection in liquefiable soil, Proceedings of 4th Japan–Greece Workshop Seismic Design of Foundations, Innovations in Seismic Design, and Protection of Cultural Heritage, Tazoh and Gazetas (eds), Vol.2, 237-246.

Khan, M. R. A., Hayano, K. and Kitazume, M. (2008): Investigation on static stability of sheet pile quay wall improved by cement treated sea-side ground from centrifuge model tests, Soils and Foundations, Vol.48, No.4, 563-575.

Khan, M. R. A., Hayano, K. and Kitazume, M. (2009): Behavior of sheet pile quay wall stabilized by sea-side ground improvement in dynamic centrifuge tests, Soils and Foundations, Vol.49, No.2, 193-206.

Kimura, M. Inazumi, S., Too, J. K. A., Isobe, K., Mitsuda, Y. and Nishiyama, Y. (2007): Development and application of H-joint steel pile sheet piles in construction of foundations for structures, Soils and Foundations, Vol.47, No.2, 237-251.

Kondo, Y., Jin, Y., Bao, X., Nakamura, K. and Zhang, F. (2010): Numerical experiment on seismic behavior of group-pile foundation with partial ground solidification under dynamic loading, Proc. Symposium of Chubu Branch of The Japanese Geotechnical Society, Vol.22, 109-114 (In Japanese).

Kusakabe, O. and Kobayashi, S. (2010): Foundations, Soils and Foundations, Vol.50, No.6, 903-913.

Maeda, Y., Ichikawa A., Tsurukubo, S, Saito, Y., Hirose, T. and Sakate, M. 2008: Study on bearing capacity characteristics and practical application of composite ground pile foundation, Japanese Geotechnical Journal, Vol. 3, No. 1, 37-54 (In Japanese).

Motamed, R., Tohata, I., Honda, T., Yasuda, S., Tabata, T. and Nakazawa, H. (2009): Behaviour of pile group behind a sheet pile quay wall subjected to liquefaction-induced large ground deformation observed in shaking test in E-Defense project, Soils and Foundations, Vol.49, No.3, 459-475.

Motamed, R., Sesov, V., Tohata, I. and Anh, N. T. (2010): Experimental modeling of large pile groups in sloping ground subjected to liquefaction-induced lateral flow: 1-G shaking table tests, Soils and Foundations, Vol.50, No.2, 261-279.

Shirato, M., Koseki, J., Fukui, J. and Kimura, Y. (2006): Effects of stress-dilatancy behavior of soil on load transfer hysteresis in soil-pile interaction, Soils and Foundations, Vol.46, No.3, 281-298.

Shirato, M., Nonomura, Y., Fukui, J. and Nakatani, S. (2008): large-scale shake table experiment and numerical simulation on the nonlinear behavior of pile-groups subjected to large-scale earthquakes, Soils and Foundations, Vol.48, No.3, 375-396.

Tomisawa, K. and Miura, S. (2007): Mechanical behavior of pile foundation constructed in composite ground and its evaluation, Soils and Foundations, Vol.47, No.5, 961-972.

Tazoh, T., Sato, M., Jang, J., Kimata, H., Kobayashi, N. and Gazetas, G. (2011): Seismic behavior of batter pile foundation -Centrifuge tests and analytical study, Proceedings of 4th Japan–Greece Workshop Seismic Design of Foundations, Innovations in

Seismic Design, and Protection of Cultural Heritage, Tazoh and Gazetas (eds), Vol.2, 199-216.

Tokimatsu, K., Suzuki, H., Tabata, K. and Sato, M. (2007): Three dimensional shaking table tests on soil-pile-structure models using E-defense facility, Proceedings of 4th International Conference on Earthquake Engineering, June 25-28, Thissaloniki, Greece

Uno, K., Mitou, M. and Otsuka, H. (2011): Shaking table test of bridge pile foundation in liquefied ground focused on section force to the intermediate part of pile, Proceedings of 4th Japan–Greece Workshop Seismic Design of Foundations, Innovations in Seismic Design, and Protection of Cultural Heritage, Tazoh and Gazetas (eds), Vol.2, 227-236.

Uzuoka, R., Sento, N. and Kazama, M. (2008): Seepage and inertia effect on rate-dependent reaction of a pile in liquefied soil, Soils and Foundations, Vol.48, No.1, 15-25.

Ye, B. (2007): Experiment and Numerical Simulation of Repeated Liquefaction -Consolidation of Sand, Doctoral Dissertation, Gifu University

Zhang, F., Kimura, M., Nakai, T. and Hoshikawa., T. (2000): Mechanical behavior of pile foundations subjected to cyclic lateral loading up to the ultimate state, Soils and Foundations, Vol.40, No.5, 1-17.

Zhang, F. and Kimura, M. (2002): Numerical prediction of the dynamic behaviors of an RC group-pile foundation, Soils and Foundations, Vol.42, No.3, 77-92.

Zhang, F., Ye, B., Noda, T., Nakano M. and Nakai, K. (2007) : Explanation of cyclic mobility of soils: Approach by stress-induced anisotropy, Soils and Foundations, Vol.47, No.4, 635-648.

Zhang, F., Jin, Y., Ye, B. (2010): A try to give a unified description of Toyoura sand, Soils and Foundations, Vol.50, No.3, 679-693.

Zhang, F., Ye, B. and Ye, G. L. (2011) : Unified description of sand behavior, Frontiers of Architecture and Civil Engineering in China, Vol.5, No.2, 121–150.

CHAPTER 6 Dynamic analyses on undersea soft rock to clarify the mechanism of the formation from proto-decollement to decollement

6.1 Introduction

The Japanese Islands are located on the boundary of four plates, and experience massive earthquakes from the geography condition. Then, the oceanic plate underthrust beneath the continental plate, the decollement zone in the Nankai trough accretion prism is attracting attention. It is said that before the oceanic plate becoming a boundary, the decollement equivalent layer referred to as proto-decollement exists in the oceanic plate as shown in Figure 1. The clarification of the mechanism process of formation from proto-decollement to the decollement is one step to the clarification of the mechanism of the earthquake. According to existed study, heterogeneous brittle shear and consolidation characterize the early evolution of the decollement zone. High density values in the decollement zone and the rapid drops of density values at its bottom have been found by X-ray computed tomography scan image. This suggests that the decollement zone can prevent the consolidation of underlying sediments. Despite intense brittle fracturing in the decollement zone, the over-consolidation due to the decollement sealing may induce high fluid pressure at the top of underthrust sediments, resulting in strain decoupling at the base of the decollement zone (Tobin, et al. 2000).

There are a lot of spaces in the structure of proto-decollement. However, when forming the decollememt, the cementation between these particles collapses and the space becomes small. As a result, it is not the regular consolidation trend but the extremely consolidation, and becomes dense. This extremely consolidation is thought to be the reason of earthquake caused by plats shifting. The study in this chapter is to study the mechanism of the form of decollment by numerical simulation.

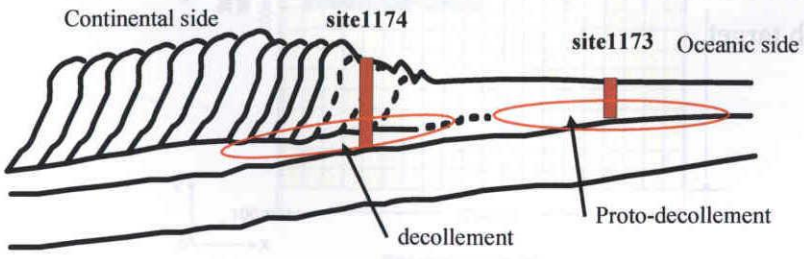

Figure 1 Trough section of South Sea

6.2 FEM model and input wave

Material parameters

The numerical simulation is carried in two cases, which are elastic analysis and elastoplastic analysis. The parameters used in the simulation are shown in Table 1. Figure 2 shows the stress-strain relationships of the soft rock in triaxial drained tests.

Table1 Parameters of the undersea soft rock (cyclic mobility model)

ν	e_o	R_f	λ	κ	m	m^*	R^*_0	ζ_0	b_r	OCR
0.2	0.7	3.9	0.011	0.00076	0.1	0.1	0.5	0	0.1	6(3)

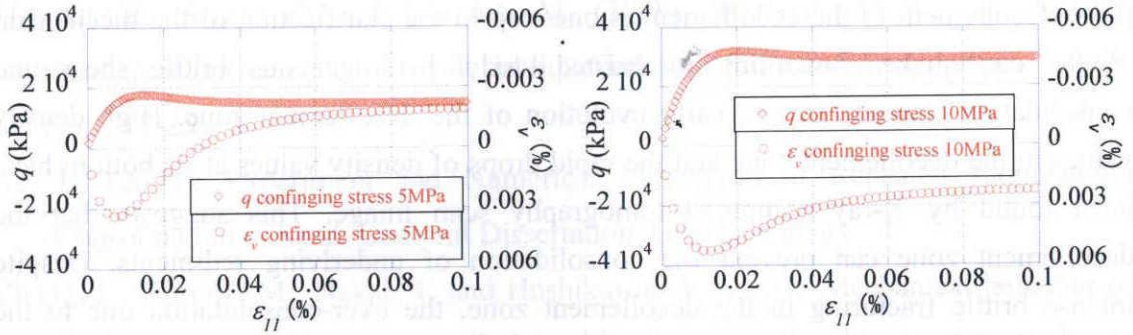

a) Confining stress 5MPa (OCR6) b) Confining stress 10MPa (OCR3)

Figure 2 Stress-strain relationships in triaxial drained tests

Analysis range and FEM mesh

The analysis takes a large range of length 10000m, width 10000m and depth 3000m area show as Figure 3. For the boundary condition, all the boundary surfaces are free except that the bottom is fixed in x, y, z direction. The results of elements noted in blue and nodes noted in red at the depth of 1650m with a confining stress of 9.75MPa are put out as research target.

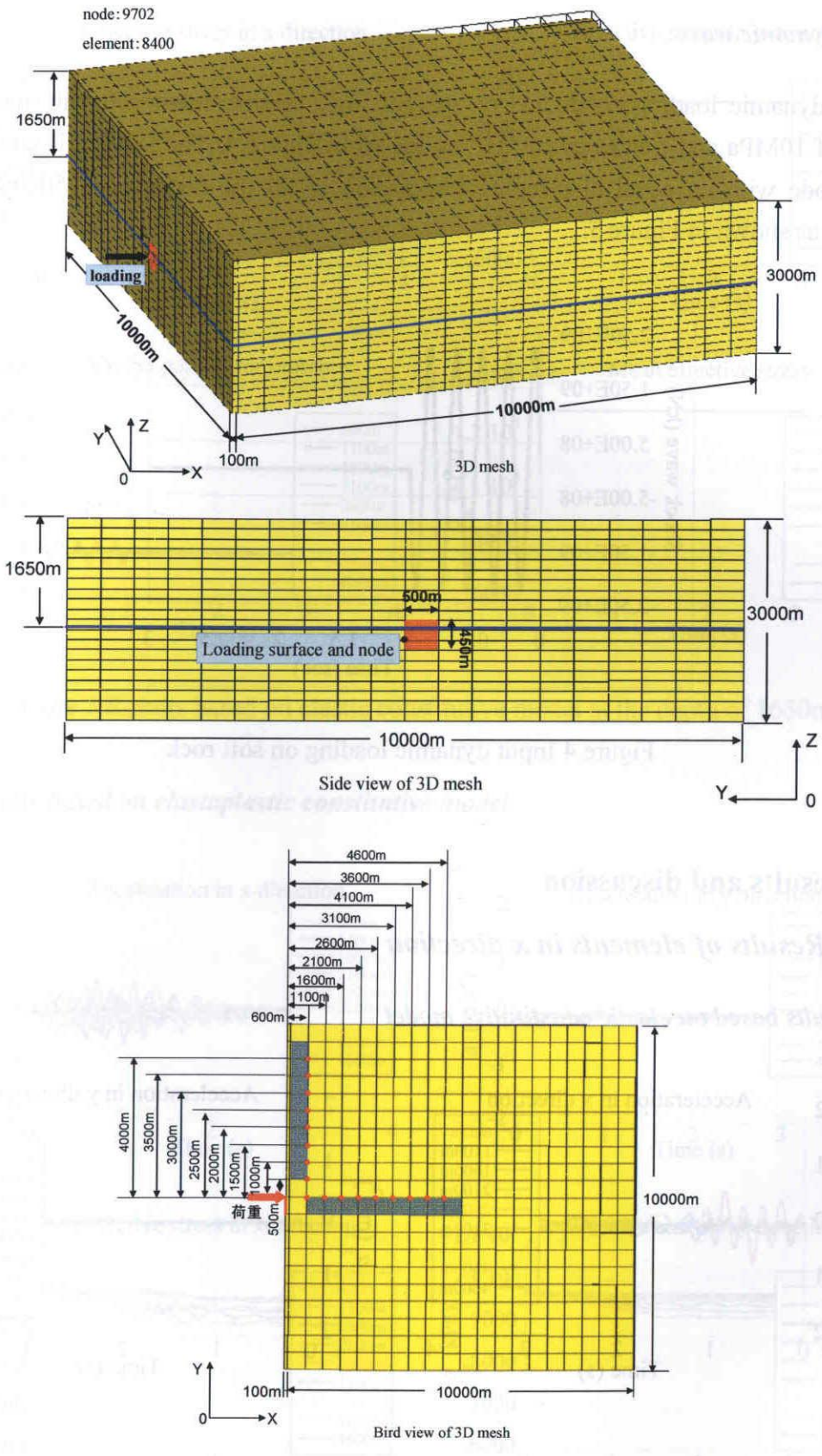

Figure 3 Analysis mesh of 3D and object of study

Input dynamic wave

The dynamic loading conducted on the soft rock is sine wave with the maximum value of 10MPa and frequency of 5HZ as shown in Figure 4. The loading is conducted on a node with an equal displacement condition of all the nodes on a 500mX450m surface as shown in Figure 3.

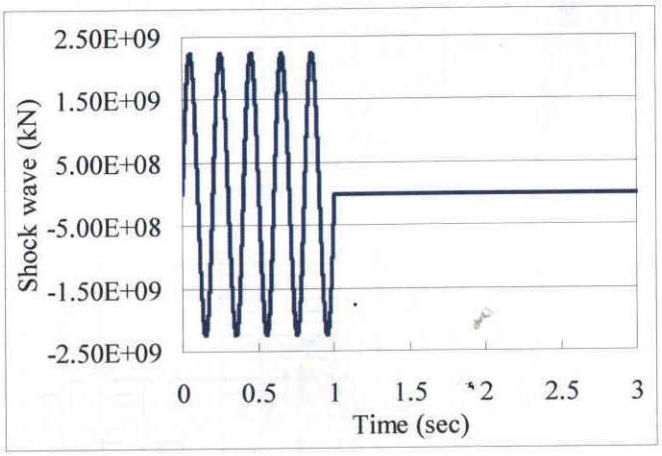

Figure 4 Input dynamic loading on soft rock

6.3 Results and discussion

6.3.1 Results of elements in x direction

a) Results based on elastic constitutive model

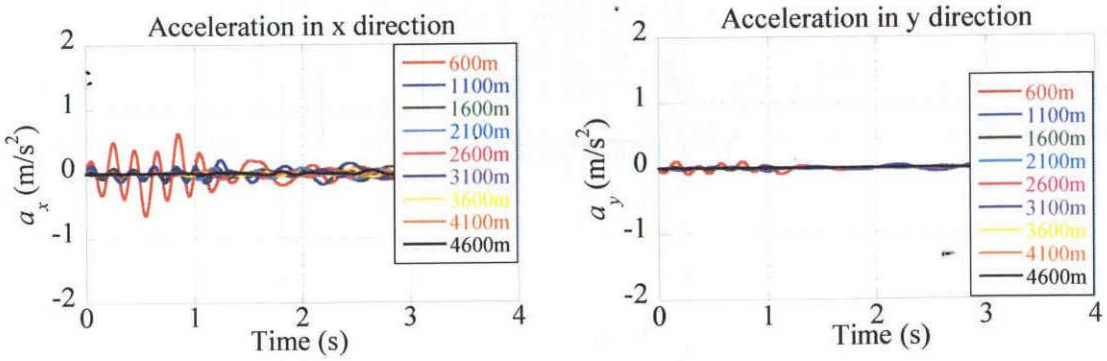

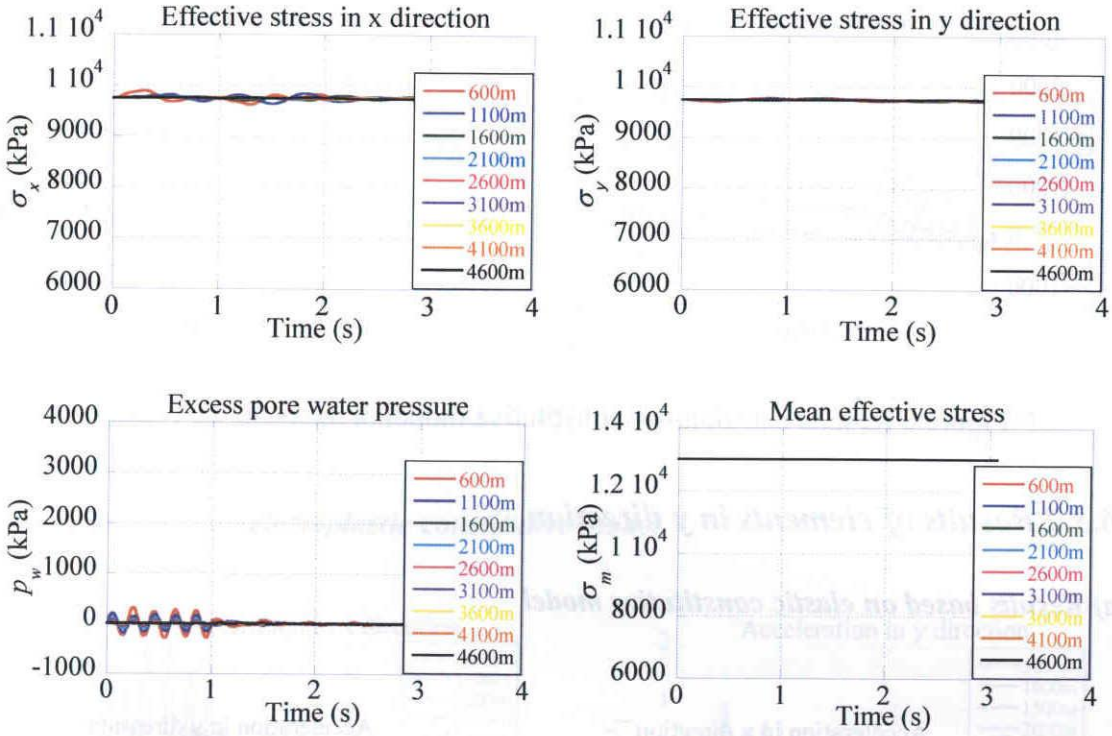

Figure 5 Results based on elastic constitutive model at the depth of 1650m

b) Results based on elastoplastic constitutive model

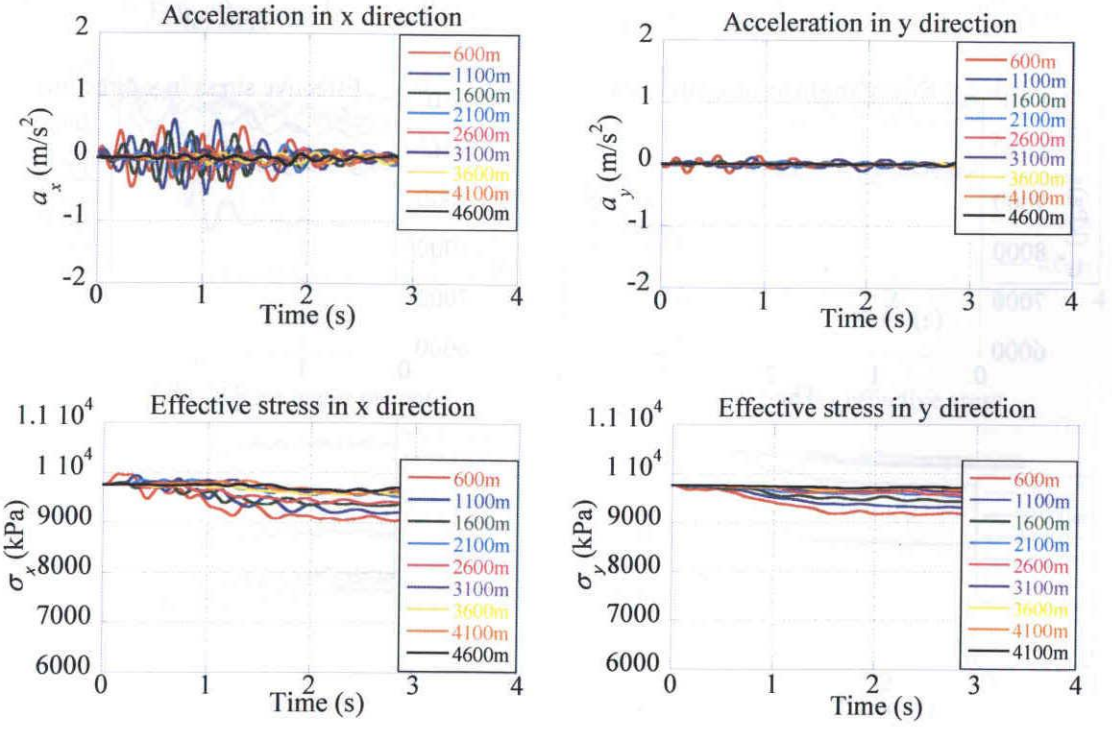

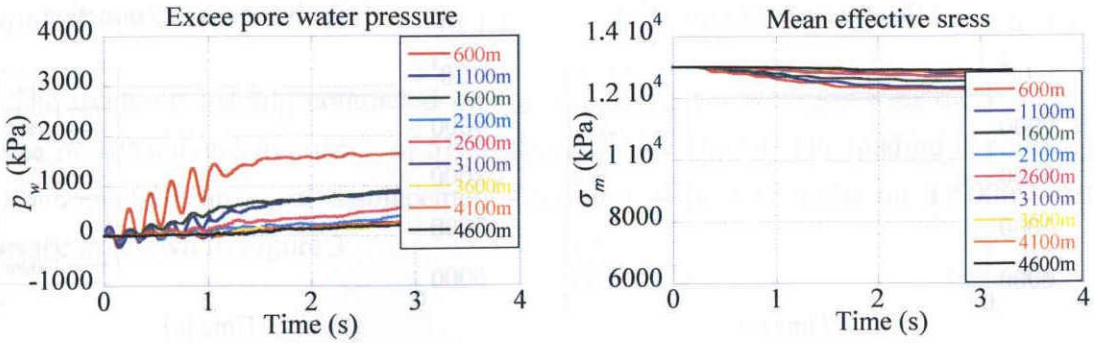

Figure 6 Results elastoplastic constitutive model at the depth of 1650m

6.3.2 Results of elements in y direction

a) Results based on elastic constitutive model

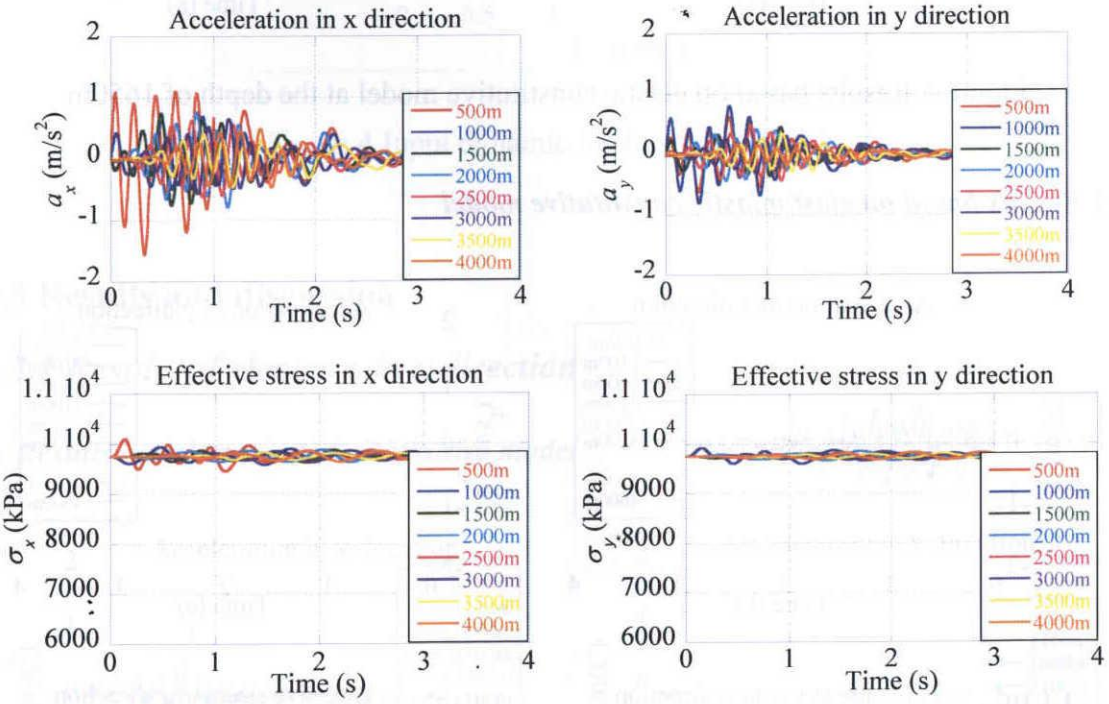

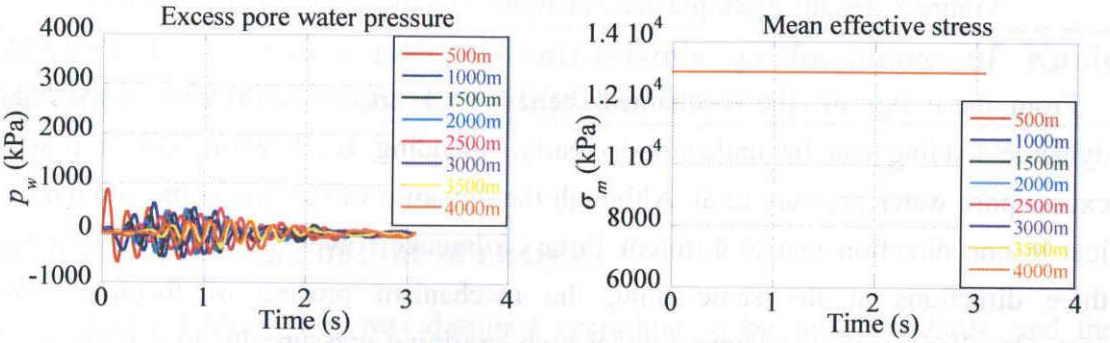

Figure 7 Results based on elastic constitutive model at the depth of 1650m

b) Results based on elastoplastic constitutive model

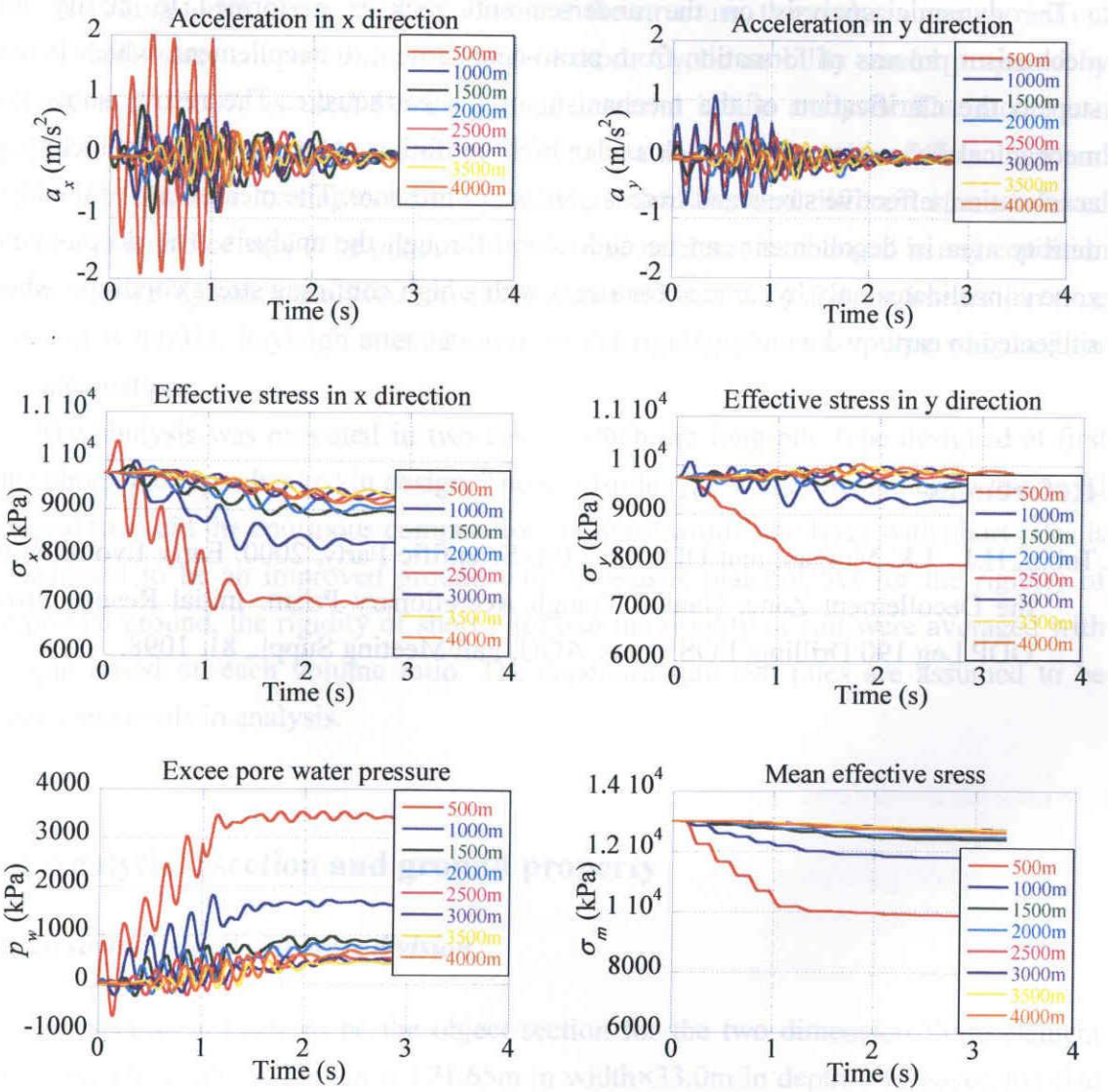

Figure 8 Results elastoplastic constitutive model at the depth of 1650m

From these figures, the mechanical behavior of undersea soft rock subjected to dynamic loading can be understood clearly, including acceleration, effective stress, excess pore water pressure et al. Although the dynamic wave used in the simulation is just in one direction that is different from earthquake waves which are usually from three directions at the same time, the mechanism process of formation from proto-decollement to decollement under high confining pressure due to earthquake can be clarified by this numerical simulation.

6.4 Summary

The dynamic analysis on the undersea soft rock is performed to clarify the mechanism process of formation from proto-decollement to decollement, which is one step to the clarification of the mechanism of the earthquake. The results show the mechanical behaviors of soft rock under high confining stress of 9.75MPa including acceleration, effective stress and excess pore water pressure. The mechanism of the high density area in decollement can be understood through the analysis. The decollement zone consolidates only by large shear stress with a high confining stress condition when subjected to earthquake motions.

References

Tobin, H.J., J K Morgan, and ODP Leg 190 Scientific Party, 2000, Early Evolution of the Decollement Zone, Nankai Trough Accretionary Prism: Initial Results From ODP Leg 190 Drilling, EOS Trans. AGU, Fall Meeting Suppl., 81, 1098.

CHAPTER 7 Evaluation of anti-seismic performance of Kanie Parking Lot foundation based on liquefaction analysis

7.1 Introduction and outline of analysis

The Kanie Parking Lot was designed according to building standards, and the anti-seismic capacity for the upper structure will not be evaluated because it belongs to the field of structure mechanics. However, the structure calculation of the upper part is necessary because the inertial force acts from the upper part to the base. Therefore the structure model used in this analysis was extracted by the first class authorized architect according to the conventional specifications of structure.

According to the geometrical condition of the structure, the analysis was carried out by 2D soil-water coupled finite element method. Cyclic mobility model proposed by Zhang et al (2007) is used for the ground material in the analysis. The model can explain the mechanical behaviors of soil in drain condition with different ground materials, different loading conditions, different densities and different stress-induced history in a unified way (The parameter of the soil need not be changed in any condition at all). In the dynamic analysis, Newmark-β method was used and the integration time interval is 0.002s. Rayleign attenuation of initial rigidity proportion type was used for the attenuation.

The analysis was executed in two cases, which are long-pile type designed at first and short-pile type changed in design. The short-pile type was evaluated as an improved ground to avoid the enormous computation. In other words, the layer with short piles is considered to be an improved ground with an elastic material. As for the rigidity of improved ground, the rigidity of short piles and the rigidity of soil were averaged with weight based on each volume ratio. The superstructure and piles are assumed to be elastic materials in analysis.

7.1 Analytical section and ground property

Analysis range and soil layer division

E-F section is made to be the object section for the two dimension finite element analysis. The analysis domain is 171.65m in width×33.0m in depth. Moreover, the size

of building is 67.65m in width and 19.8m in height. For the thickness of each layer, A_{s1}=2m、 A_{s2}=2m、 A_{s3}=2m、 A_{s4}=2m、 $A_{silt.1}$=5m、 $A_{silt.2}$=2m、 A_{s5}=1m、 $A_{silt..3}$=3m、 A_{s6}=6m、 A_{s7}=2m、 $A_{silt..4}$=2m、 A_{s8}=2m、 $A_{silt..5}$=2m. The groundwater level is GL-2.0m.

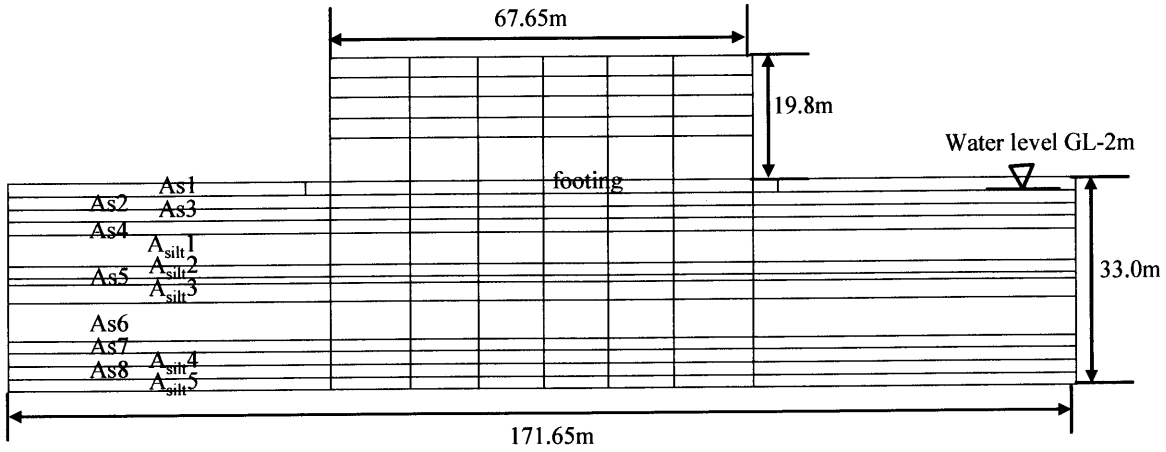

(a) Case-1 long-pile type

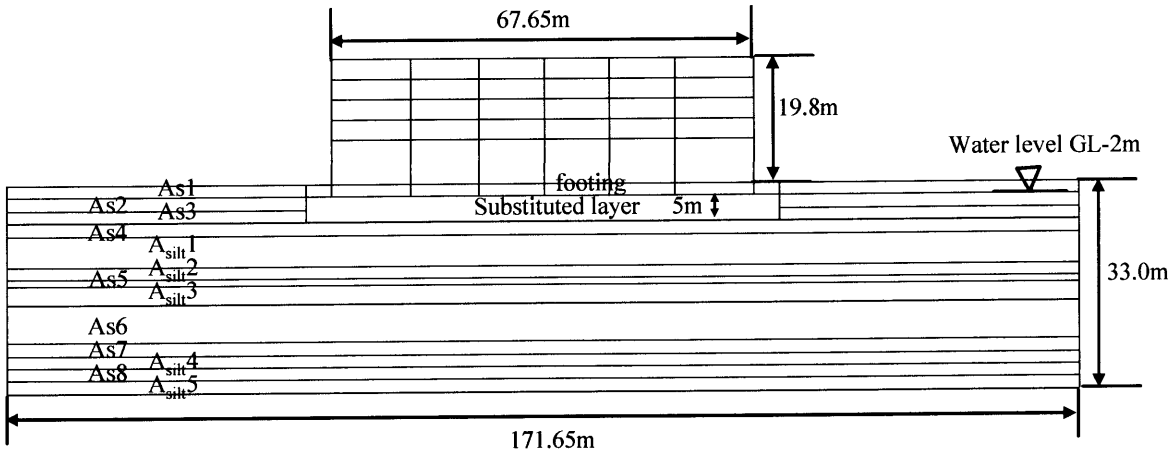

(b) Case-2 improved ground (short-pile type)

Figure 1 Analysis section and soil layers

Ground parameter and soil element behavior

The ground parameter of each soil lay used in calculation is shown in Table 1 and Table 2. Figure 2 shows elements simulation results in each layer. The liquefaction strength curve of loose sand layer A_{s2} is shown in Figure 3.

Table 1 Material parameters of each soil layer

Layer	λ	κ	ν	R_f	e_0	a	b_r	m
Very loose sand A_{s1} A_{s4}	0.050	0.010	0.30	4.60	0.80	2.2	1.5	0.10
Loose sand A_{s2} A_{s3} A_{s5} A_{s6}	0.030	0.0060	0.30	4.60	0.78	2.2	1.5	0.10
Middle dense sand A_{s7} A_{s8}	0.024	0.0048	0.30	4.60	0.75	2.2	1.5	0.10
Loose silt $A_{silt.1\sim3}$	0.207	0.041	0.35	3.50	1.1	0.10	0.10	3.8
Bottom silt $A_{silt.4\sim5}$	0.207	0.035	0.35	3.50	1.1	0.10	0.10	3.8
Improved material	$E=10^5$kPa ; $\nu=0.25$							

Table 2 Physical and state variable of each soil layer

Layer	OCR	D_r(%)	R^*_0	k (m/sec)	γ(kN/m^3)
Very loose sand A_{s1} A_{s4}	4.0	53	0.80	1.0E-4	17.6
Loose sand A_{s2} A_{s3} A_{s5} A_{s6}	5.0	58	0.80	1.0E-4	17.6
Middle dense sand A_{s7} A_{s8}	6.0	78	0.80	1.0E-4	17.6
Loose silt $A_{silt.1\sim3}$	2.5		0.60	1.0E-6	16.7
Bottom silt $A_{silt.4\sim5}$	2.5		0.60	1.0E-6	17.6
Improved material					

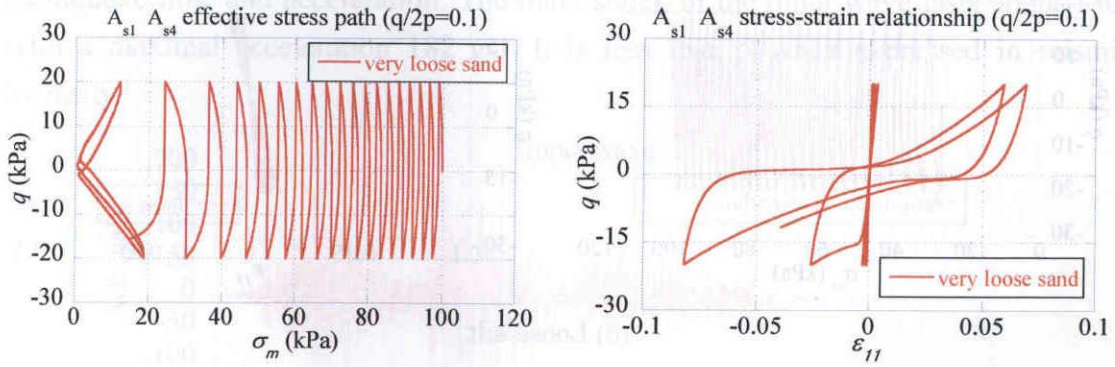

(a) Very loose sand

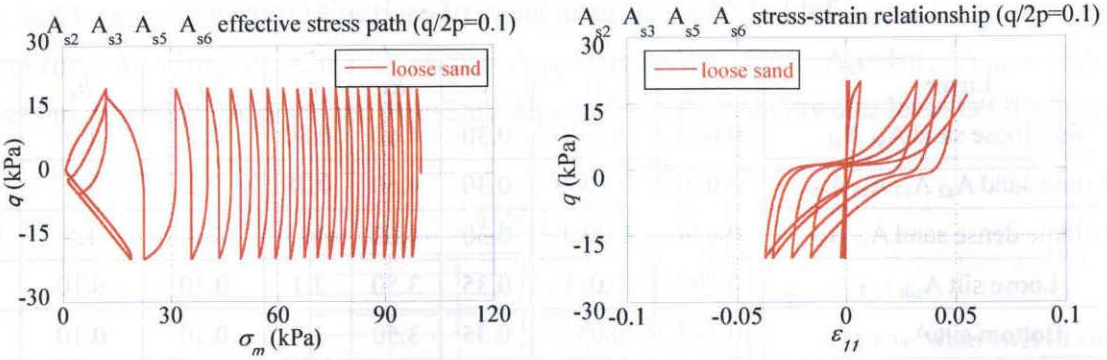

(b) Loose sand

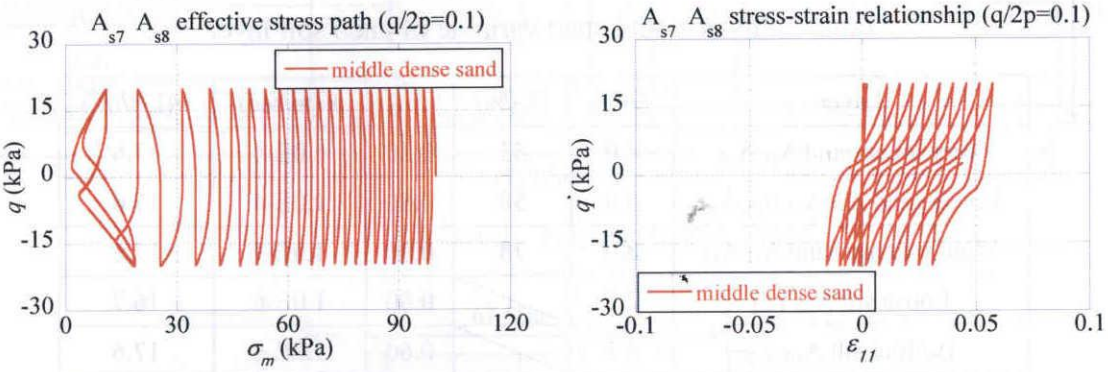

(c) Middle dense sand

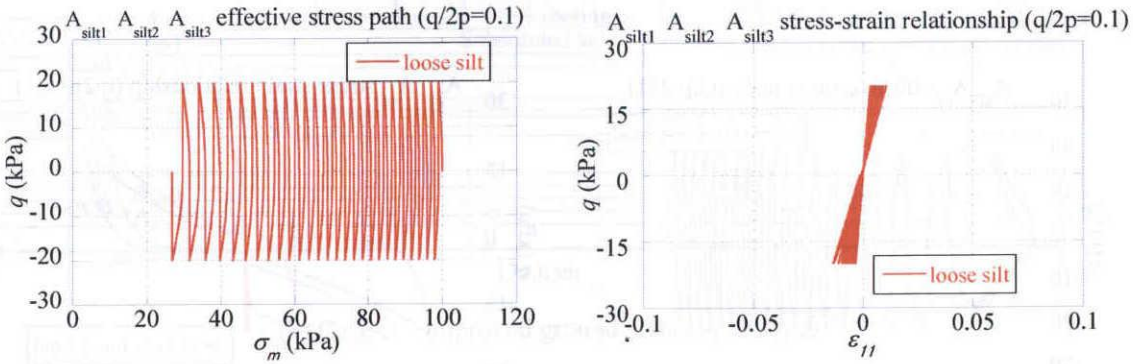

(d) Loose silt

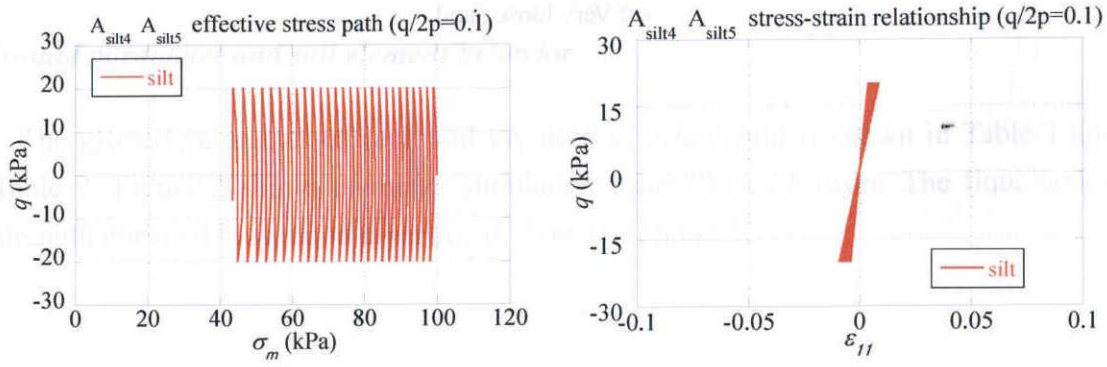

(e) Bottom silt

Figure 2 Elements simulation of each layer

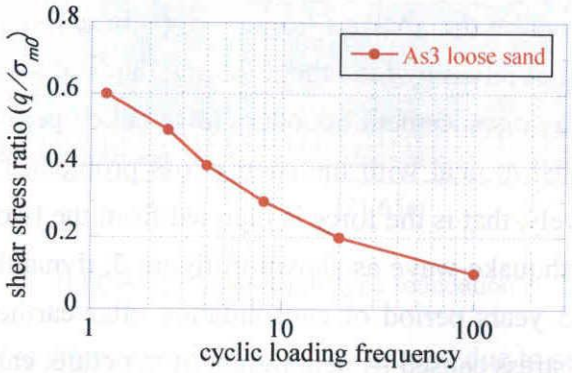

Figure 3 Liquefaction strength curve of the alluvion sand layerA_{s2}

7.3 Input earthquake wave

The input earthquake wave was the forecast 3 synchronization earthquake wave of eastern sea, southeast sea and south sea that was made by Pro. Sugito Masata in Gifu university (the giant earthquake countermeasure proposed to society by the national universities of three prefectures in eastern sea aria, 2011.11.20). Figure 4 shows earthquake time and acceleration. The main shock of the input wave lasts about 150s with a maximal acceleration 182 gal. It is less than 5 when expressed in seismic intensity.

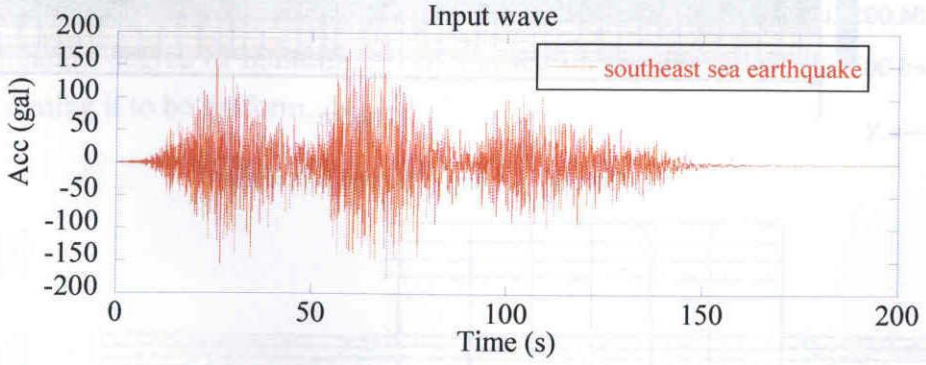

Figure 4 Time and acceleration of 3 synchronization earthquake wave (Amax: 18.23cm/sec^2, Vmax: 22.34cm/sec)

7.4 Analysis condition

The soil condition used in structure design was based on the result of the boring No.1 survey, and the same soil condition was used in the analysis. The layered foundation was supposed in the analysis because big stratum ups and downs in the site of this structure were not found by the other 2 boring dates in the vicinity. In the case of dynamic analysis, equal displacement boundary (also called periodical boundary) in the lateral boundary is used to deal with the energy loss problem. On the other hand, the bottom is fixed relatively, that is the force is inputted from the two sides.

Using the input earthquake wave as shown in figure 3, dynamic analysis was carried out followed by a 3.5 years period of consolidation after earthquake. FEM mesh and initial mean effective stress caused by self-weight of structure, car loading and ground is shown in Figure 5. The lived load becomes uniform caused by parking from the second floor to the fifth floor. As shown in figure 5, the worst condition that parking concentrates on the left half sides of all the floors is assumed in the analysis. Before dynamic analysis, static analysis that considers the structure-ground as a whole system was carried out to get the initial effective stress of the ground.

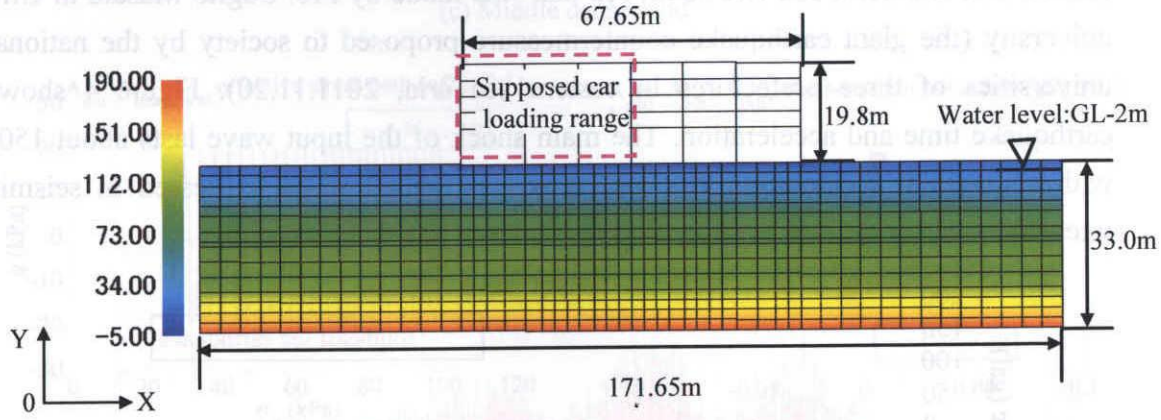

(a) Case-1 Long-pile type foundation

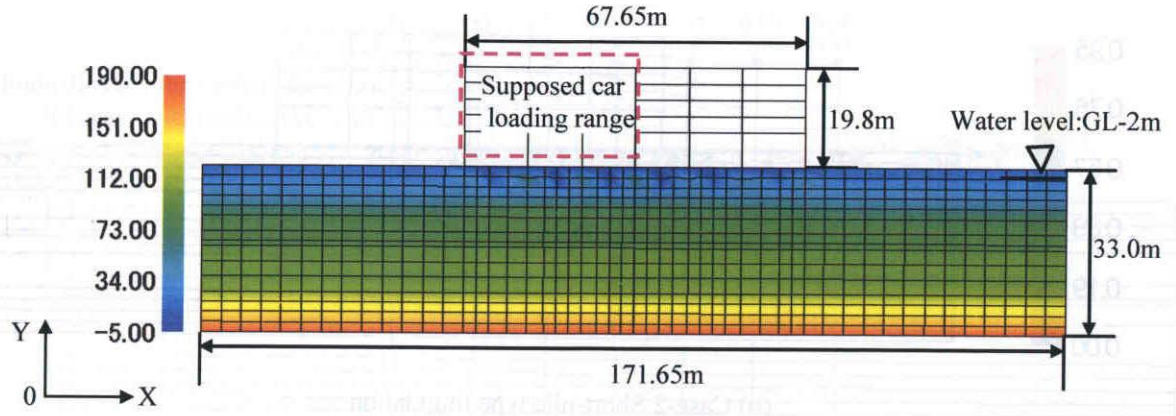

(b) Case-2 Short-pile type foundation

Figure 5 Mean effective stress distribution of the ground due to self-weight (unit: kPa)

7.5 Liquefaction analysis results and discussion

Figure 6 shows the distribution of displacement vector immediately after earthquake, and Figure 7 shows the distribution of displacement vector 3.5 years after earthquake. Figure 8 shows the comparison of vertical displacement of building between the two cases. Figure 9 shows excess pore water pressure ratio immediately after earthquake. From the results it is understood that liquefaction occurred in the vicinity of GL-4~-6.0m (Excess pore water pressure ratio≒1.0).

In the case of long-pile type foundation, the settlement difference of the left and right side ends is 0.24cm immediately after earthquake. However, in the case of short-pile type is 6.70cm immediately after earthquake and 12.10cm 3.5 years after earthquake. The inclination degree of building is 1.8‰ based on the amount of uneven settlement when assuming it to be uniform.

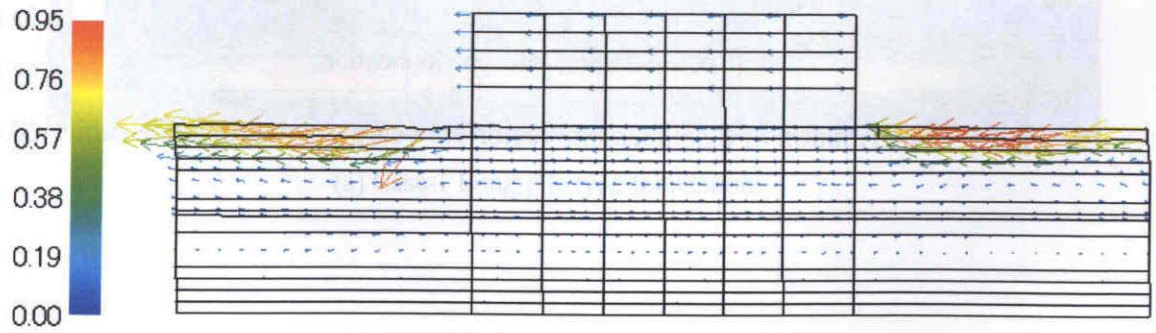

(a) Case-1 Long-pile type foundation

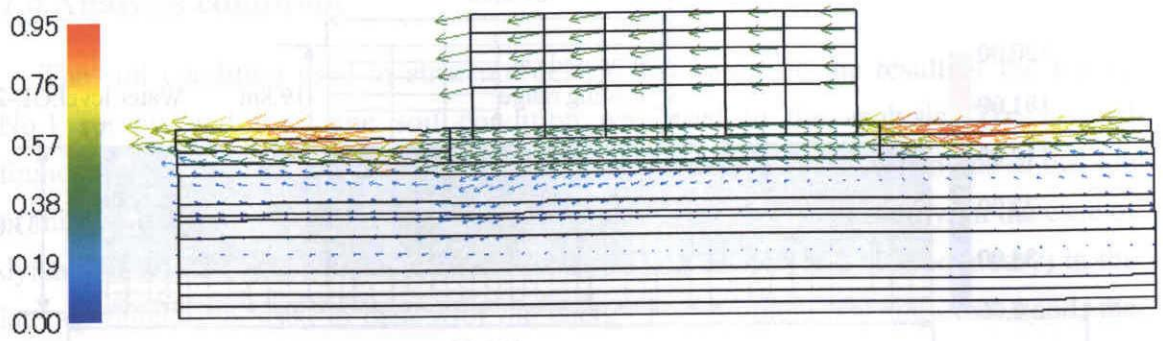

(b) Case-2 Short-pile type foundation

Figure 6 Distribution of displacement vector immediately after earthquake (unit: m)

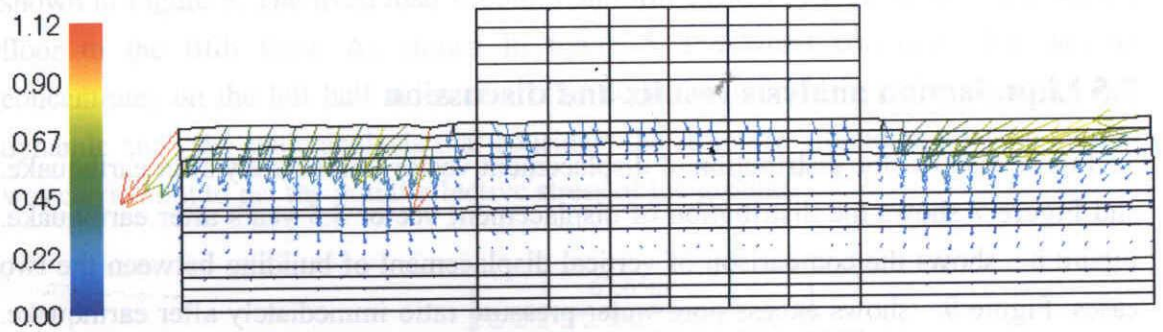

(a) Case-1 Long-pile type foundation

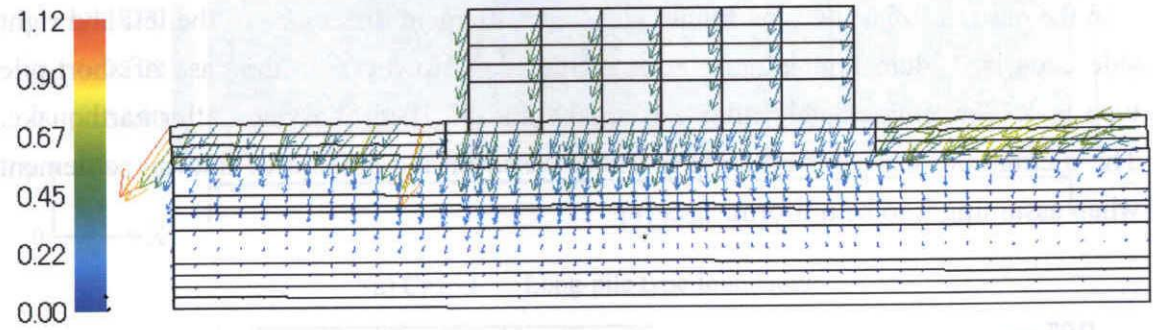

(b) Case-2 Short-pile type foundation

Figure 7 Distribution of displacement vector 3.5 years after earthquake (unit: m)

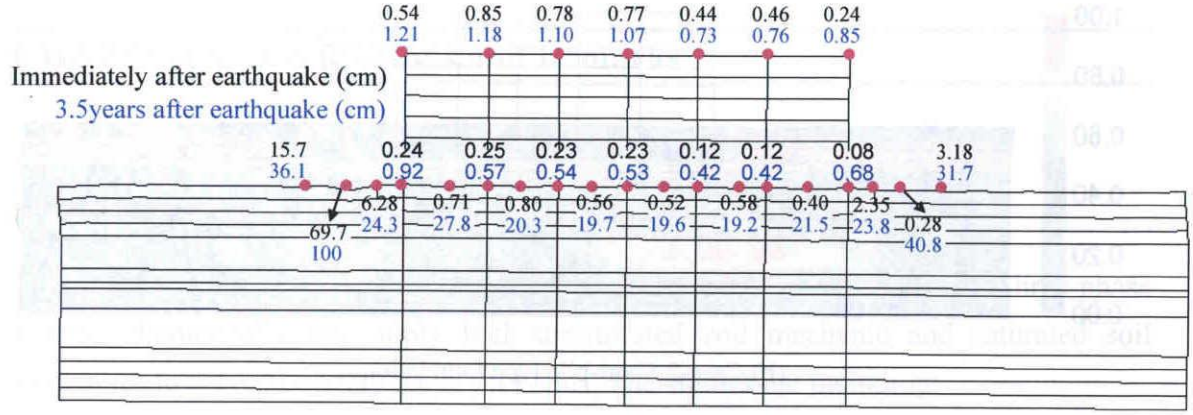

(a) Case-1 Long-pile type foundation

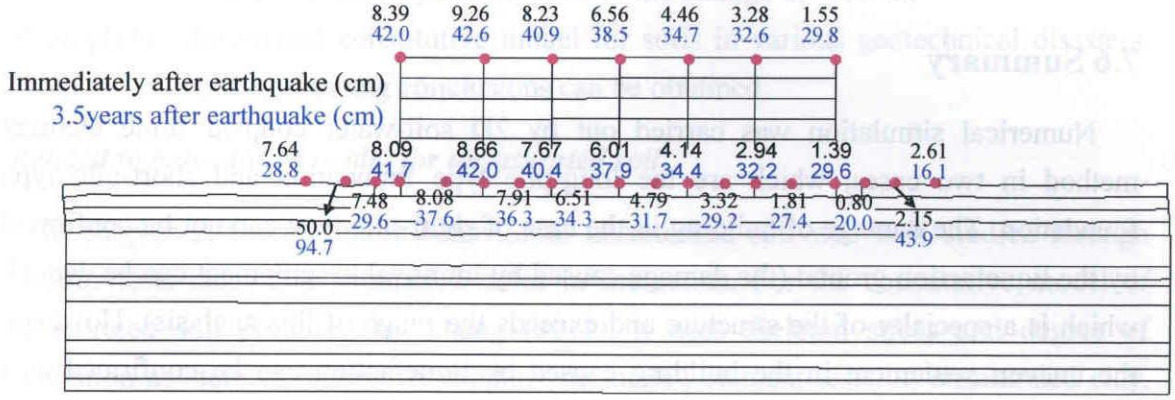

(b) Case-2 Short-pile type foundation

Figure 8 Vertical displacement of building

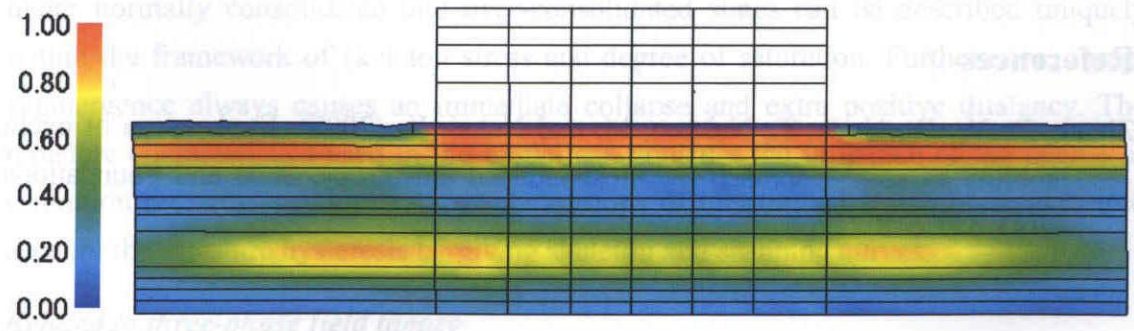

(a) Case-1 Long-pile type foundation

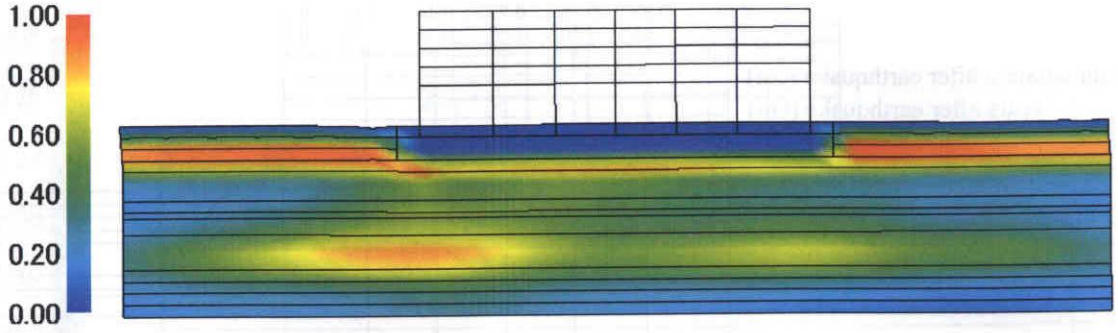

(b) Case-2 Short-pile type foundation

Figure 9 Excess pore water pressure ratio immediately after earthquake

7.6 Summary

Numerical simulation was carried out by 2D soil-water coupled finite element method in two cases, which are the long-pile type foundation and short-pile type foundation. The damage of building in the case of short-pile type can not be confirmed by the liquefaction ground (the damage caused by immovable settlement can be denied, which is a specialty of the structure and exceeds the range of this analysis). However, the uneven settlement in the building caused by liquefaction can be confirmed at a maxim value of12.10cm, which did not occur in the case of long-pile type foundation. The seismic stability of the structure foundation was well evaluated by this numerical analysis.

References

Zhang, F., Ye, B., Noda, T., Nakano, M. and Nakai, K. (2007): Explanation of cyclic mobility of soils: approach by stress-induced anisotropy, Soils and Foundations, 47(4), 635-648.

CHAPTER 8 Conclusions and Remarks

8.1 Conclusions

The main purpose of this research is to investigate the soil-water-air three-phase mixture theoretically and apply both unsaturated soil mechanic and saturated soil mechanics to solve boundary value problems. The studies are including:

1) Investigating the mechanical behaviors of unsaturated soil;
2) Proposing a water-air-soil three-phase model in the FE-FD program and performing a 2D numerical analysis on slope failure due to the change of suction;
3) Applying the existed constitutive model for soils in various geotechnical disasters.

From the study, the following conclusions can be obtained:

Related to constitutive model for unsaturated soil

In chapter 2, the mechanic behavior of unsaturated soil was well studied through various tests dates and simulation dates in literatures. For the constitutive model of unsaturated soil proposed by Zhang (2011), it uses skeleton stress and degree of saturation as state variables. To validate the model, element tests on unsaturated clay, silt, sand and rock fill soil are performed. Trough the comparison of results between tests and simulation, it is confirmed that the model can give well description of yield stress, shear strength and volume change behaviors of soil, especially collapse by submergence. Moreover, the overall behaviors of both unsaturated and saturated soil under normally consolidated and over-consolidated states can be described uniquely within the framework of skeleton stress and degree of saturation. Furthermore, abrupt submergence always causes an immediate collapse and extra positive dilatancy. The moisture characteristics used in the model can consider the influence of the degree of saturation on stress-strain-dilatancy relationships of unsaturated soils, for it takes into account the moisture hysteresis by giving skeleton and scanning curves.

Related to three-phase field theory

In chapter 3, the field governing equations in soil-water-air three-phase problems are descretized in detail in FEM scheme with a proper incorporation of the constitutive model in which the degree of the saturation is taken as the state variable. The three-phase field theory can properly take into account the interaction between the solid

phase and fluid phase (water and air), which is of great significance in unsaturated infiltration analysis.

In this three-phase field theory, the displacement of solid u, the pore water pressure p^w are taken as the basic variables in the governing equations. The finite element is used to discretize the field equations in space, and finite difference method is used for the discretization of the continuity equation for the pore fluid. Newmark-β method is employed to descretize the field equation in time.

The simulation of an element subjected to different loading and water infiltration has been conducted as a boundary value problem and it is known that the collapse behavior due to the increase of degree of saturation commonly observed in water infiltration test can be well described by the proposed numerical analysis.

Related to numerical simulation of unsaturated model slope

In chapter 4, combining the new constitutive model and three-phase field theory, 2D numerical analysis was conducted to simulate the process of infiltration in unsaturated Shirasu slope.

In both the test and simulation, the pore water pressure increased rapidly after keeping at a constant value before the slope failure occurred. This phenomenon is very important in predicting the slope failure. However, this result was just proved in the model scale, and field measurement date in full scale should be checked.

From the simulation results, the water seepage process with the slope can be observed clearly. The comparison between simulation and test showed that the numerical simulation could generally describe the mechanical behavior of unsaturated soil and seepage behavior obtained from test.

The numerical results can not correspond to the test results at the values of pore water pressure and the time. The above unsolved problem should be investigated more based on various unsaturated soil tests and improved numerical method.

Related to numerical simulation of shaking table test on group pile foundation

In this chapter 5, numerical tests with 3D static FEM analyses on seismic enhancement effect of existing group-pile foundation with ground improvement, are conducted firstly to find out an optimum pattern of the ground improvement, using the program DBLEAVES. Based on the results, a shaking table test was then conducted on a model full system with a superstructure, a nine-pile foundation and a sandy ground using the selected optimum pattern of the ground improvement to verify the

enhancement effect of the partial ground improvement method. Moreover, the test result was also simulated with 3D dynamic FEM analyses using the same program DBLEAVES. The following conclusions can be given:

In the analysis, the material parameters of the ground, Toyoura sand, are all the same as those used in the past researches (Zhang et al, 2010 and 2011), implying that the parameters of the Toyoura sand are definitely determined, no matter what kind of the boundary value problem may be.

In finding out the optimum pattern of ground improvement around existing pile foundation, numerical tests considering three influential factors, that is, the size, the location and the shape of the partial ground improvement around the pile group, are calculated in static loading with many patterns. It is found based on the concept of improvement efficiency that for the present pile foundation, the optimum pattern is that the partial ground improvement zone is 6m in height, 0 m to 4.5 m in depth and 9m in length.

Based on the optimum pattern, the efficiency of seismic enhancement by the partial ground improvement method is confirmed by shaking table test. It is found that on the whole, the enhancement effect to reduce the bending moment within the piles can be achieved with the partial ground improvement method, especially within the improved area. In present case, the bending moment at the top of the pile is reduced greatly.

Numerical simulation of the shaking table test with 3D dynamic FEM analysis using DBLEAVES was also conducted. The same tendency of the reinforcement effect of the partial ground improvement method was observed in the shaking table test. The efficiency of the partial ground improvement method for the seismic reinforcement of the existing pile foundation is also confirmed by the numerical analysis.

The most important result newly obtained in the present study is that, the factor that the enhancement effect to reduce the deformation of an existing group-pile foundation and the bending moment of the piles can be achieved with the partial ground improvement method, has been confirmed by both shaking table test and elastoplastic finite element analysis. The partial ground improvement method has been used in practical engineering for some years but its enhancement effect has not been clarified systematically in previous studies. Another important result newly obtained in the present study is that, the factor that the proposed numerical method using DBLEAVES

is capable to evaluate properly the seismic behavior of pile foundation, is verified again. In the numerical analyses, nonlinear behaviors of ground and pile are described by cyclic mobility model and the AFD model, respectively.

Related to numerical simulation of undersea soft rock

In chapter 6, simulation is performed on the undersea soft rock under high confining stress state subjecting to dynamic loading to clarify the mechanism process of the formation from proto-decollement to decollement, which is one step to the clarification of the earthquake mechanism. The mechanical behaviors of the soft rock subjecting to huge dynamic loadings such as earthquake motions were well examined. The study object is selected at a depth of 1650m under seabed, where has a confining stress of 9.75MPa. Through the results including acceleration, effective stress and excess pore water pressure, it is understood that the decollement zone which has a high confining stress may consolidate and become dense when subjected to huge shear stress caused by earthquake.

Related to numerical simulation of Kanie Parking Lot foundation

In chapter 7, numerical simulation was carried out by 2D soil-water coupled finite element method evaluate the anti-seismic performance of Kanie Parking Lot foundation in two cases to, which are the long-pile type foundation and short-pile type foundation. In the numerical calculation based on liquefaction analysis, the process during earthquake was simulated by a dynamic soil-water coupled analysis, while the process of dissipation of excess pore water pressure was simulated by a static consolidation analysis. The mechanical behavior of the ground during liquefaction and the settlement in post-liquefaction was well examined. Through the results, it is clear that although the ground in both two cases liquefied, the structure with the long-pile type foundation has less uneven settlement than the short-pile type foundation after earthquake. The seismic stability of the structure foundation was well evaluated by this numerical analysis.

Through the research, the numerical method to solve boundary value problems is confirmed by various calculations and experiments. It has provided an important procedure to the practice of unsaturated and saturated soil mechanics. Many geotechnical disasters can be predicted by the numerical method together with in situ tests. However, there are still some problems remained for future study in the usage of unsaturated mechanics.

8.2 Remarks on future study

The validity of the proposed constitutive model for unsaturated-saturated soil should be confirmed with more laboratory tests in the future study. 2D soil-water-air coupled finite element analyses were conducted to simulate the unsaturated Shirasu slope infiltration in three cases. Although the analysis reproduced the water seepage to a reasonable accuracy, there still some unsolved problem. Firstly, the accuracy of the relationship between the pore water pressure and time of the collapse of the slope. Secondly, the simulation was just on model test, the field investigation and the simulation in real scale slope is needed. Lastly, the simulation of the increase of pore water pressure with water injection in three different places respectively, was conducted by increasing the water head from the initial underground water level to the designated water level. This process is different to the natural raining. In a word, validation and modification of the proposed constitutive model and numerical method for unsaturated-saturated soil are needed in future work especially when performing the analysis in full scale of unsaturated slopes by comparing the simulation results with the field measurement dates. Moreover, an unsaturated slope failure prevention system based on the numerical simulation and field investigation should be planed in future study.

APPENDIX I BRIEF DESCRIPTION OF CYCLIC MOBILITY MODEL

The original model (Zhang et al., 2007) is proposed based on the concepts of subloading (Hashiguchi and Ueno, 1977) and superloading (Asaoka et al., 1998). Here a brief description of the model is given.

The similarity ratio of the superloading surface to normal yield surface R^* and the similarity ratio of the superloading surface to subloading surface R are given as,

$$R^* = \frac{\tilde{p}'}{\bar{p}'} = \frac{\tilde{q}}{\bar{q}},\ 0 < R^* \le 1 \ \ and \ \frac{\tilde{q}}{\tilde{p}'} = \frac{\bar{q}}{\bar{p}'} \tag{1}$$

$$R = \frac{p'}{\bar{p}'} = \frac{q}{\bar{q}},\ 0 < R \le 1, \ \ and \ \ \frac{\bar{q}}{\bar{p}'} = \frac{\tilde{q}}{\tilde{p}'} = \frac{q}{p'} \tag{2}$$

where, $(p', q), (\tilde{p}', \tilde{q})$ and $(\bar{p}', \bar{q})$ represent the present stress state, the corresponding normally consolidated stress state and the structured stress state at p-q plane, respectively. The normally yield surface is given in the following form as:

$$f(\tilde{p}', \tilde{\eta}^*, \zeta) + \int_0^t J\mathrm{tr}\boldsymbol{D}^p d\tau = \mathrm{MD}\ln\frac{\tilde{p}'}{\tilde{p}_0'} + \mathrm{MD}\ln\frac{\mathrm{M}^2 - \zeta^2 + \tilde{\eta}^{*2}}{\mathrm{M}^2 - \zeta^2} + \int_0^t J\mathrm{tr}\boldsymbol{D}^p d\tau = 0 \tag{3}$$

where, $\tilde{\eta}^* = \eta^*$, and the other variables involved in Equations, A II - (1), (2) and (3) are defined as:

$$\eta^* = \sqrt{3\hat{\boldsymbol{\eta}}\cdot\hat{\boldsymbol{\eta}}}/\sqrt{2},\ \ \hat{\boldsymbol{\eta}} = \boldsymbol{\eta} - \boldsymbol{\beta},\ \ \boldsymbol{\eta} = \boldsymbol{S}/p',\ \ \boldsymbol{S} = \boldsymbol{T}' + p'\boldsymbol{I},\ \ p' = -\mathrm{tr}\boldsymbol{T}'/3 \tag{4}$$

$$\zeta = \sqrt{2/3}\sqrt{\boldsymbol{\beta}\cdot\boldsymbol{\beta}},\ \ \eta = \sqrt{2/3}\sqrt{\boldsymbol{\eta}\cdot\boldsymbol{\eta}} \tag{5}$$

where, $\boldsymbol{S}$ is the deviatory stress tensor; $\boldsymbol{\beta}$ is the anisotropic stress tensor, and $\boldsymbol{T}'$ is the Cauchy effective stress tensor and is assumed to be positive in tension. In Equation A II -(3), J is the Jacobean determination of deformation gradient tensor $\boldsymbol{F}$ and can be expressed as:

$$J = \det\boldsymbol{F} = \frac{v}{v_0} = \frac{1+e}{1+e_0} \tag{6}$$

where v and v_0 are the specific volume at the current time (t) and the specific value at the reference time (t=0). D is the dilatancy parameter which can be expressed by $\tilde{\lambda}, \tilde{\kappa}$ the compression and the swelling index, respectively, as follows:

$$D=\frac{\tilde{\lambda}-\tilde{\kappa}}{M(1+e_0)}=\frac{\tilde{\lambda}-\tilde{\kappa}}{Mv_0} \tag{7}$$

$\boldsymbol{D}^p$ denotes the plastic component of stretching $\boldsymbol{D}$ which is assumed to be positive in tension, and is related to the plastic volumetric strain rate in the following form under the condition that the compressive of the volumetric strain is supposed to be positive:

$$\varepsilon_v^p=-\int_0^t J\mathrm{tr}\boldsymbol{D}^p d\tau \tag{8}$$

By substituting Equations A II -(1) and A II -(2) into Equations A II -(3), subloading yield surface can also be written as:

$$\begin{aligned} &f(p',\eta^*,\zeta)+MD\ln R^*-MD\ln R+\int_0^t J\mathrm{tr}\boldsymbol{D}^p d\tau \\ &=MD\ln\frac{p'}{p_0'}+MD\ln\frac{M^2-\zeta^2+\eta^{*2}}{M^2-\zeta^2}+MD\ln R^*-MD\ln R+\int_0^t J\mathrm{tr}\boldsymbol{D}^p d\tau=0 \end{aligned} \tag{9}$$

An associated flow rule is employed in the present model, namely,

$$\boldsymbol{D}^p=\lambda\partial f/\partial\boldsymbol{T}' \tag{10}$$

The consistency equation for the subloading yield surface can then be given as:

$$\frac{\partial f}{\partial\boldsymbol{T}'}\cdot\overset{\circ}{\boldsymbol{T}}'+\frac{\partial f}{\partial\boldsymbol{\beta}}\cdot\overset{\circ}{\boldsymbol{\beta}}+MD\frac{\dot{R}^*}{R^*}-MD\frac{\dot{R}}{R}+J\mathrm{tr}\boldsymbol{D}^p=0 \tag{11}$$

where, $\overset{\circ}{\boldsymbol{T}}'$ and $\overset{\circ}{\boldsymbol{\beta}}$ are the Green-Naghdi rates of stress tensor $\boldsymbol{T}'$ and anisotropic stress tensor $\boldsymbol{\beta}$, respectively. $\boldsymbol{\Omega}$ is material spin tensor. It is easy to obtain the following relation:

$$\frac{\partial f}{\partial p'}=MD\left(\frac{1}{p'}+\frac{\partial(\eta^{*2})}{\partial p'}/(M^2-\zeta^2+\eta^{*2})\right)=MD\frac{M^2-\eta^2}{(M^2-\zeta^2+\eta^{*2})p'} \tag{12}$$

From Equation A II -(12), it is clear that the *C.S.L.*, defined by the condition in which $\partial f/\partial p'=0$, always satisfies the relation η=M, implying that the *C.S.L.*, as the threshold between plastic compression and plastic expansion, does not move with the changes in the anisotropy.

Evolution rule for the anisotropic stress tensor is defined as:

$$\overset{\circ}{\boldsymbol{\beta}}=\frac{J}{D}b_r(M-\zeta)\sqrt{2/3}\left\|\boldsymbol{D}_s^p\right\|\frac{\hat{\boldsymbol{\eta}}}{\|\hat{\boldsymbol{\eta}}\|} \tag{13}$$

where, $\zeta<M$ provides a natural physical limitation on the development of anisotropy automatically., it is known from the evolution Equation A II -(13) that development of

anisotropy will stop at the state when $\boldsymbol{\eta} = \boldsymbol{\beta}$.

Evolution rule for degree of structure R*, which is the same as in the work by Asaoka et al. (2002), is adopted:

$$\dot{R}^* = JU^*\sqrt{2/3}\left\|\boldsymbol{D}_s^p\right\|,\quad U^* = aR^*(1-R^*)/\mathrm{D},\quad (0 < R^* \le 1) \tag{14}$$

The changing rate of overconsolidation is assumed to be controlled by two factors, namely, the plastic component of stretching and the incremental anisotropy as,

$$\dot{R} = JU\left\|\boldsymbol{D}^p\right\| + \frac{R}{\mathrm{MD}}\frac{\eta}{\mathrm{M}}\frac{\partial f}{\partial \boldsymbol{\beta}}\cdot\mathring{\boldsymbol{\beta}} \tag{15}$$

In which, $\mathring{\boldsymbol{\beta}}$ is proportional to the norm of the plastic component of stretching $\left\|\boldsymbol{D}_s^p\right\|$ and U is given by the following relation as:

$$U = -\frac{m}{\mathrm{D}}\left(\frac{(p'/p_0')^2}{(p'/p_0')^2+1}\right)\ln R \tag{16}$$

where p_0' =98.0 kPa is reference stress.

If the stretching is divided into elastic and plastic components, and the elastic components follow

$$\mathring{\boldsymbol{T}}' = \boldsymbol{E}\boldsymbol{D}^e,\quad \boldsymbol{D} = \boldsymbol{D}^e + \boldsymbol{D}^p,\quad \mathring{\boldsymbol{T}}' = \boldsymbol{E}\boldsymbol{D} - \Lambda\boldsymbol{E}\frac{\partial f}{\partial \boldsymbol{T}'} \tag{17}$$

The positive valuable Λ ($(\Lambda=\lambda)$) can be rewritten as :

$$\Lambda = \frac{\dfrac{\partial f}{\partial \boldsymbol{T}'}\boldsymbol{E}\boldsymbol{D}}{\dfrac{\partial f}{\partial \boldsymbol{T}'}\boldsymbol{E}\dfrac{\partial f}{\partial \boldsymbol{T}'} + J\dfrac{\mathrm{MD}}{(\mathrm{M}^2-\zeta^2+\eta^{*2})p'}(\mathrm{M}_s^2-\eta^2)} \tag{18}$$

where

$$\begin{aligned}\mathrm{M}_s^2 &= \mathrm{M}^2 - \frac{m\mathrm{M}\ln R}{R}\left\{\frac{(p'/p_0')^2}{(p'/p_0')^2+1}\right\}\sqrt{6\eta^{*2}+\frac{1}{3}(\mathrm{M}^2-\eta^2)^2}\\ &-2a\mathrm{M}(1-R^*)\eta^* + (1-\frac{\eta}{\mathrm{M}})\frac{\sqrt{6}\mathrm{M}b_r(\mathrm{M}-\zeta)\eta^{*2}(2\mathrm{M}^2-3\boldsymbol{\eta}\cdot\boldsymbol{\beta})}{(\mathrm{M}^2-\zeta^2+\eta^{*2})(\mathrm{M}^2-\zeta^2)}\end{aligned} \tag{19}$$

The loading criteria are given below:

$$\begin{cases} \Lambda > 0 & \textit{loading} \\ \Lambda = 0 & \textit{neutral} \\ \Lambda < 0 & \textit{unloading} \end{cases} \tag{20}$$

In most cases, the denominator is positive, therefore, $\Lambda > 0$ is equivalent to the following relation:

$$\frac{\partial f}{\partial \boldsymbol{T}'} \cdot \boldsymbol{ED} > 0 \tag{21}$$

APPENDIX II AXIAL-FORCE DEPENDENCY MODEL (AFD MODEL)

The derivation of a beam model considering the axial-force dependency and taking a weak form of the equilibrium equation for a beam, which satisfies the compatibility of the deformation, is given in detail. For abbreviation, the model is called as axial-force dependent model (AFD model, Zhang and Kimura, 2002a). In the model, the plane-section assumption is still kept valid and the stress-strain relations of reinforcement and concrete are shown in Figure IV-1. As shown in Figure, ε_a, the strain at a arbitrary point P(x,y) at the sectional plane of a beam, can be divided into three parts, that is, the bending strain ε_{m1} due to M_x, the bending strain ε_{m2} due to M_y and axial strain ε_0 due to axial force, as shown in following equation,

$$\varepsilon_a = \varepsilon_{m1} + \varepsilon_{m2} + \varepsilon_0 = \left(x\{H_u''(z)\}^T + y\{H_v''(z)\}^T - \{H_w'(z)\}^T \right) \cdot [A]\{\delta\} = \{F(z)\}^T \cdot [A]\{\delta\} \qquad (1)$$

where, $\{\delta\} = \{u_i \quad v_i \quad w_i \quad \theta_{xi} \quad \theta_{yi} \quad u_j \quad v_j \quad w_j \quad \theta_{xj} \quad \theta_{yj}\}^T$ is the nodal displacement vector.

$$\{F(z)\}^T = \left(x\{H_u''(z)\}^T + y\{H_v''(z)\}^T - \{H_w'(z)\}^T \right) \qquad (2)$$

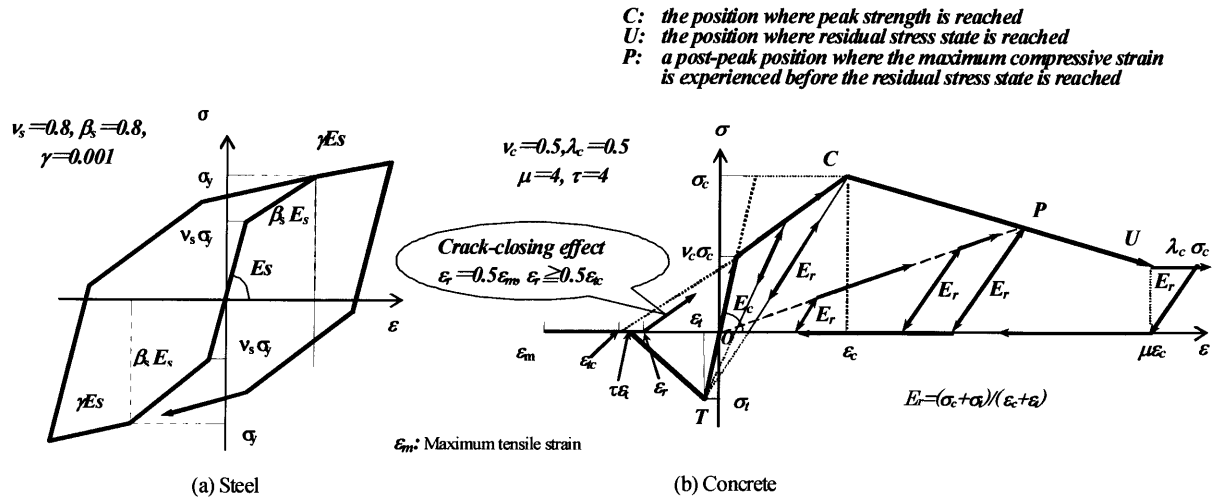

Figure IV-1 Nonlinear properties of reinforcement and concrete

$$\begin{aligned}
\{H_u''(z)\}^T &= \{0\ \ 0\ \ 0\ \ 0\ \ 0\ \ 2\ \ 0\ \ 0\ \ 0\ \ 6z\} \\
\{H_v''(z)\}^T &= \{0\ \ 0\ \ 0\ \ 0\ \ 0\ \ 0\ \ 2\ \ 0\ \ 6z\ \ 0\} \\
\{H_w'(z)\}^T &= \{0\ \ 0\ \ 0\ \ 0\ \ 0\ \ 0\ \ 0\ \ 1\ \ 0\ \ 0\}
\end{aligned} \tag{3}$$

$$[A] = \begin{pmatrix}
1 & 0 & 0 & 0 & 0 & 0 & 0 & 0 & 0 & 0 \\
0 & 1 & 0 & 0 & 0 & 0 & 0 & 0 & 0 & 0 \\
0 & 0 & 1 & 0 & 0 & 0 & 0 & 0 & 0 & 0 \\
0 & 0 & 0 & 1 & 0 & 0 & 0 & 0 & 0 & 0 \\
0 & 0 & 0 & 0 & 1 & 0 & 0 & 0 & 0 & 0 \\
-3/l^2 & 0 & 0 & 0 & -2/l & 3/l^2 & 0 & 0 & 0 & -1/l \\
0 & -3/l^2 & 0 & -2/l & 0 & 0 & 3/l^2 & 0 & -1/l & 0 \\
0 & 0 & -1/l & 0 & 0 & 0 & 0 & 1/l & 0 & 0 \\
0 & 2/l^3 & 0 & 1/l^2 & 0 & 0 & -2/l^3 & 0 & 1/l^2 & 0 \\
2/l^3 & 0 & 0 & 0 & 1/l^2 & -2/l^3 & 0 & 0 & 0 & 1/l^2
\end{pmatrix} \tag{4}$$

The virtual energy stored in the beam element due to a virtual strain can be expressed as,

$$U = \iiint_v \sigma_a \cdot d\varepsilon_a dv = \{d\delta\}^T \iiint E \cdot [A]^T \{F(z)\} \cdot \{F(z)\}^T [A] dv \cdot \{\delta\} \tag{5}$$

On the other hand, virtual energy W brought about by the external force due to a virtual displacement, is $W=\{d\delta\}^T\{F\}$. Therefore, the virtual energy theory $(W=U)$ can be obtained as

$$\{F\} = \iiint E \cdot [A]^T \{F(z)\} \cdot \{F(z)\}^T [A] dv \cdot \{\delta\} = [K] \cdot \{\delta\} \tag{6}$$

where, $[K]$is the stiffness matrix of the beam element and can be rewritten as

$$[K] = \iiint E [A]^T [I] [A] dv \tag{7}$$

$$\begin{aligned}
[I] = \{F(z)\} \cdot \{F(z)\}^T &= \left(x\{H_u''(z)\} + y\{H_v''(z)\} - \{H_w'(z)\}\right) \\
&\cdot \left(x\{H_u''(z)\}^T + y\{H_v''(z)\}^T - \{H_w'(z)\}^T\right)
\end{aligned} \tag{8}$$

In the classical beam theory, $[I]$ is defined by Equation AIV- (9) in which the influence on the M-Φ relation due to the axial force is not considered, namely,

$$[I] = [I_1] = x^2 \{H_u''(z)\} \cdot \{H_u''(z)\}^T + y^2 \{H_v''(z)\} \cdot \{H_v''(z)\}^T + \{H_w'(z)\} \cdot \{H_w'(z)\}^T \tag{9}$$

Based on Equations AIV- (8) and (9), $[I]$ can be rewritten as

$$[I]=[I_1]+[I_2] \tag{10}$$

where, $[I_2]$is evaluated by the following equation:

$$\begin{aligned}[I_2]= xy\cdot\left(\{H_u''(z)\}\cdot\{H_v''(z)\}^T+\{H_v''(z)\}\cdot\{H_u''(z)\}^T\right)\\ -x\left(\{H_u''(z)\}\cdot\{H_w''(z)\}^T+\{H_w''(z)\}\cdot\{H_u''(z)\}^T\right)\\ -y\left(\{H_v''(z)\}\cdot\{H_w''(z)\}^T+\{H_w''(z)\}\cdot\{H_v''(z)\}^T\right)\end{aligned} \tag{11}$$

$[I_2]$ is the newly added item which takes into consideration the influence on the M-Φ relation due to the axial force. Based on the above equations, $[K]$ can be expressed as

$$[K]=[A]^T\cdot[D]\cdot[A],\ [D]=\begin{bmatrix}0_{5\times5} & 0_{5\times5}\\ 0_{5\times5} & D_1\end{bmatrix} \tag{12}$$

where,

$$[D_1]=\begin{bmatrix}4lEI_y & 4lEI_{xy} & -2lEx & 6l^2EI_{xy} & 6l^2EI_y\\ 4lEI_{xy} & 4lEI_x & -2lEy & 6l^2EI_x & 6l^2EI_{xy}\\ -2lEx & -2lEy & lEA & -3l^2Ey & -3l^2Ex\\ 6l^2EI_{xy} & 6l^2EI_x & -3l^2Ey & 12l^3EI_x & 12l^3EI_{xy}\\ 6l^2EI_y & 6l^2EI_{xy} & -3l^2Ex & 12l^3EI_{xy} & 12l^3EI_y\end{bmatrix} \tag{13}$$

$$\begin{aligned}&EA=\iint E\cdot dA,\quad EI_y=\iint E\cdot x^2\cdot dA\\ &EI_x=\iint E\cdot y^2\cdot dA,\quad EI_{xy}=\iint E\cdot x\cdot y\cdot dA\\ &Ex=\iint E\cdot x\cdot dA,\quad Ey=\iint E\cdot y\cdot dA\end{aligned} \tag{14}$$

The integration in Equation 14 can be evaluated by discretizing area A into N small areas A_i and taking the sum as

$$EI_y=\iint E\cdot x^2\cdot dA=\sum_{i=1}^{N}E_ix_i^2A_i. \tag{15}$$